

# **From the Sun to Earth**

## **Exploring the Multifacets of Solar**

## **Eruptive Events**

Mohamed Nedal

A thesis submitted for the degree of  
Doctor of Philosophy

Institute of Astronomy and National Astronomical Observatory,  
Bulgarian Academy of Sciences  
Solar and Space Weather Research  
January 10, 2024

Supervisor: Assoc. Prof. Kamen Asenov Kozarev

# Acknowledgments

To my family, professors, and friends ...

# Contents

|          |   |           |
|----------|---|-----------|
| <b>1</b> | <b>Introduction</b>   | <b>2</b>  |
| 1.1      | Background and Motivation . . . . .   | 2         |
| 1.1.1    | Coronal Waves . . . . .   | 3         |
| 1.1.2    | Solar Radio Bursts . . . . .  | 4         |
| 1.1.3    | Solar Energetic Particle (SEP) Forecasting . . . . .  | 5         |
| 1.2      | Objectives and Scope . . . . .  | 6         |
| 1.3      | Methodology Overview . . . . .  | 6         |
| 1.4      | Main Contributions . . . . .  | 7         |
| 1.5      | Outline . . . . .   | 7         |
| <b>2</b> | <b>Characterization of Coronal Bright Fronts</b>  | <b>8</b>  |
| 2.1      | Introduction . . . . .  | 8         |
| 2.2      | Observations . . . . .  | 8         |
| 2.3      | Data Analysis and Methods . . . . .   | 8         |
| 2.4      | Results and Discussion . . . . .  | 8         |
| 2.5      | Conclusions . . . . .   | 8         |
| 2.6      | Wavetrack: A Flexible Framework for Automated Recognition and Tracking of Wave-Like Events in Solar Imagery . . . . . | 8         |
| 2.6.1    | Overview . . . . .  | 8         |
| 2.7      | Geomagnetic Storms: CME Speed De-Projection vs. In Situ Analysis . . . . .  | 11        |
| <b>3</b> | <b>Solar Radio Observations: Integrating Space-based and Ground-based Data for Coronal Diagnostics</b>                | <b>13</b> |
| 3.1      | Introduction . . . . .  | 13        |
| 3.2      | Observations . . . . .  | 15        |
| 3.2.1    | PSP Observations . . . . .  | 15        |
| 3.2.2    | LOFAR Observations . . . . .  | 18        |
| 3.3      | Methods . . . . .   | 18        |
| 3.3.1    | Imaging of radio sources . . . . .  | 18        |
| 3.3.2    | Modeling . . . . .  | 20        |
| 3.4      | Results and discussion . . . . .  | 20        |
| 3.4.1    | Detection and characterization of type III radio bursts . . . . .   | 20        |
| 3.4.2    | Imaging of radio emission sources . . . . .   | 20        |
| 3.4.3    | Plasma diagnostics and magnetic field analysis . . . . .  | 21        |
| 3.5      | Summary and conclusions . . . . .   | 22        |
| <b>4</b> | <b>Modeling and Forecasting of Solar Energetic Protons (SEP)</b>  | <b>30</b> |
| 4.1      | Introduction . . . . .  | 30        |
| 4.2      | Early-Stage SEP Acceleration by CME-Driven Shocks . . . . .   | 32        |
| 4.2.1    | Overview . . . . .  | 32        |
| 4.2.2    | Data Analysis and Methodology . . . . .   | 32        |
| 4.2.3    | Results and Discussions . . . . .   | 34        |
| 4.3      | Solar Proton Flux Forecasting with Deep Learning Models . . . . .   | 34        |
| 4.3.1    | Data preparation . . . . .  | 34        |
| 4.3.2    | Method . . . . .  | 35        |
| 4.3.3    | Results and discussion . . . . .  | 39        |
| 4.4      | Conclusions . . . . .   | 47        |

|          |  |           |
|----------|--|-----------|
| <b>5</b> | <b>Summary and Future Work</b>                         | <b>50</b> |
| 5.1      | .....  | 50        |
| 5.2      | .....  | 50        |
| 5.3      | .....  | 50        |
| 5.4      | .....  | 50        |
| 5.5      | Future Work .....                                      | 50        |
| 5.6      | Definitions and Acronyms .....                         | 50        |
| <b>A</b> | <b>Appendix</b>  | <b>52</b> |
| A.1      | Appendix for Radio Observation-related Work .....      | 52        |
| A.1.1    | Persistent imaging technique .....                     | 52        |
| A.1.2    | Resolving the radio emission location ambiguity .....  | 52        |
| A.2      | Appendix for SEP-related Work .....                    | 54        |
| A.2.1    | Terminologies .....                                    | 54        |
| A.2.2    | Mathematical Representation of the LSTM NN Model ..... | 56        |
| A.2.3    | Evaluation Metrics .....                               | 57        |
| A.2.4    | Model Configuration .....                              | 57        |
| A.2.5    | Skill Scores .....                                     | 58        |

# List of Tables

|     |  |    |
|-----|--|----|
| 3.1 | Characteristics of the type III bursts detected via the automatic algorithm from the combined spectrum. . . . .  | 19 |
| 4.1 | Summary of the performance results of the models for the validation and test sets. . . . .   | 47 |
| 4.2 | Confusion matrix for the energy channel $\geq 10$ MeV predictions in the test set. . . . .   | 47 |
| 4.3 | Comparing the skill scores with previous models. The dashed entries mean the data is unavailable (Whitman et al. (2023) for more details). . . . .   | 48 |
| A.1 | Radial distances and densities at the first ( $R_1$ ) and last ( $R_2$ ) radio sources were obtained from the $2.5 \times$ Newkirk model, as well as their impact parameters $r_1$ and $r_2$ , respectively. .   | 54 |
| A.2 | Configuration of the ML model. (1) refers to the error value for 1-day forecasting. Same for (2) refers to 2-day forecasting, and (3) for 3-day forecasting. *In the 1D-CNN layer, 32 filters, a kernel size of 5, and strides of 1 were used. . . . . | 58 |

# List of Figures

|     |  |    |
|-----|--|----|
| 3.1 | Radio dynamic spectra for a single burst obtained from multiple instruments. The top-left panel is from the LOFAR/LBA instrument, the top-right is from the PSP/FIELDS instrument, the bottom-left is from the STEREO/SWAVES instrument, and the bottom-right is from the Wind/WAVES. The vertical red dashed line denotes the start time of the burst.  | 16 |
| 3.2 | Top view of the spacecraft positions in the ecliptic plane at 12:15 UT on April 3, 2019, with the Sun-Earth line as the reference point for longitude. The Earth's location is representative of the positions of LOFAR, Wind/WAVES, and GOES-15/XRS instruments. The spacecraft were connected back to the Sun by a 400 km/s reference Parker Spiral. The black arrow represents the longitude of AR12737 and the blue arrow represents the longitude of the AR12738. The gray dotted lines are the background Parker spiral field lines. The black dashed spiral shows the field line connected to the AR12737, and the blue dashed spiral is connected to the AR12738. The figure is generated using the Solar MAGnetic Connection Haus (Solar-MACH) tool (Gieseler et al. 2023). | 17 |
| 3.3 | Exploring the X-ray and extreme ultraviolet (EUV) emissions from the Sun. The top panel showcases a cutout region of the SDO/AIA 193 Å image of the solar disk along with the STEREO-A EUVI 195 Å point of view. The white curve is the limb of the solar disk as seen by AIA from the right side. The red and blue colors are the contours of the line-of-sight magnetogram from the SDO/HMI instrument. The levels are (50, 100, 150, 300, 500, 1000) Gauss. The middle panel shows the X-ray flux from the GOES-14 spacecraft shows minimum activity. The bottom panel shows the time series of the ESP Quad band from the SDO/EVE instrument, which shows the solar irradiance in the extreme ultraviolet (EUV) band.  | 24 |
| 3.4 | Automatic detection of type III radio bursts from the combined radio dynamic spectrum of LOFAR and PSP instruments. The dashed horizontal lines separates the LOFAR frequency range (top) and the PSP frequency range (bottom).  | 25 |
| 3.5 | Automatic detection of type III bursts observed by LOFAR. The red symbols along the fit lines are the $(f, t)$ coordinates of the image snapshots shown in Figure 3.6.   | 25 |
| 3.6 | Persistence imaging for the 16 type III bursts detected in the LOFAR dynamic spectrum. The label shows the observation frequencies in MHz and times in (minutes:seconds from 12:00:00 UT). Here, the color coding is not absolute, but rather each panel has its own color code.   | 26 |
| 3.7 | Different viewing angles for the deprojection of the radio sources of the sixth burst using the $2.5 \times$ Newkirk electron-density model on the PFSS solution. The black arrow points toward the Earth's LOS. The $yz$ plane is the POS as seen from the Earth. The red dashed line is a spline curve fit for the sources' centroids. The red, black, and blue curves are the open northern, closed, and open southern field lines, respectively. The opacity of the closed field lines is decreased for better visualization.  | 27 |
| 3.8 | Synthesized maps of plasma parameters obtained using the FORWARD toolset, with the 70%-contour of radio emission of the sixth burst at the first timestamp (12:34:06.8 UT) at the frequency of 72.26 MHz depicted on top of the 2D POS cuts. The left column represents, from top to bottom, plasma density, magnetic field, and the total plasma dynamic pressure. The right column represents, from top to bottom, the temperature, plasma beta, and the Alfvén speed.   | 28 |

|      |  |    |
|------|--|----|
| 3.9  | Coronal plasma parameters sampled from the 2D maps by the source centroids. The top panel shows (from left to right) the plasma density profiles from the MAS model, 2.5×Newkirk model, and the theoretical densities under the fundamental and harmonic assumptions, plasma temperature, and magnetic field. The bottom panel shows, from left to right, the total plasma dynamic pressure, Alfvén speed, and plasma beta. The x-axis is inverted to demonstrate a progression of increasing radial distance from the Sun as the observer moves towards the right. . . . .  | 29 |
| 4.1  | Data splitting for all input features, showing the training, validation, and testing sets. Daily data from 1976-12-25 00:00 to 2019-07-30 00:00. The gray shading labels the solar cycles from SC21 to SC24. . . . .   | 36 |
| 4.2  | Correlation matrices show the correlation between the features in the training, validation, and test sets. . . . .   | 37 |
| 4.3  | Architecture of a single BiLSTM layer. The blue circles at the bottom labeled by $(x_0, x_1, x_2, \dots, x_i)$ are the input data values at multiple time steps. The purple circles, on the other hand, are the output data values at multiple time steps labeled by $(y_0, y_1, y_2, \dots, y_i)$ . The dark green and light green boxes are the activation units of the forward layer and the backward layer, respectively. The orange and yellow circles are the hidden states at the forward layer and the backward layer, respectively. Both the forward and backward layers compose a single hidden BiLSTM layer. The figure is adopted from Olah (2015) .   | 37 |
| 4.4  | Illustration of the sliding window technique for a sample of 10 timesteps, where each number denotes a distinct time step. As an example here, the input horizon (blue color) length is 4 timesteps and the output horizon length is 3 timesteps. The input window slides 1 time step at a time across the entire data sequence to generate 4 distinct input and forecast horizon pairs. The purple, orange, and green colors of the output horizon represent 1-day, 2-day, and 3-day ahead forecasting, respectively. The timesteps of 1-day ahead forecasting across the data sequences are then concatenated into a single timeseries list that is called 1-day ahead prediction. The same for 2-day and 3-day ahead. . . . . | 38 |
| 4.5  | Benchmarking of 10 models, shows the Huber loss for the validation and test sets. . . . .  | 39 |
| 4.6  | <i>Left Panel</i> - The Huber loss vs. the number of training epochs for the BiLSTM model for the validation and test sets, for the 3 energy channels. <i>Middle Panel</i> - The mean absolute error (MAE); the model's metric vs. the number of training epochs. <i>Right Panel</i> - Shows how the learning rate of the Adam optimizer changes over the number of epochs. . . . .  | 40 |
| 4.7  | Correlation between the model predictions and observations for 1-day, 2-day, and 3-day ahead for $>10$ MeV (top panel), $>30$ MeV (middle panel), and $>60$ MeV (bottom panel). The panels in the left column represent all the points of the validation set, those in the right column represent all the observations points with daily mean flux $\geq 10$ pfu. . . . .  | 41 |
| 4.8  | Same as Figure 4.7 but for the test set. . . . .   | 42 |
| 4.9  | Comparison between the model outputs and observations of the test set for the 3 energy channels. In addition to the rolling-mean window correlation for 1-day ahead predictions. . . . .   | 43 |
| 4.10 | The model's forecasts for the out-of-sample testing set for the $>10$ MeV channel are shown at forecast horizons of 1 day, 2 days, and 3 days ahead, using samples of data from December in selected years mentioned in the top-left side of the plots. . . . .  | 44 |
| 4.11 | The model's forecasts for the out-of-sample testing set for the $>30$ MeV channel are shown at forecast horizons of 1 day, 2 days, and 3 days ahead, using samples of data from December in selected years mentioned in the top-left side of the plots. . . . .  | 45 |
| 4.12 | The model's forecasts for the out-of-sample testing set for the $>60$ MeV channel are shown at forecast horizons of 1 day, 2 days, and 3 days ahead, using samples of data from December in selected years mentioned in the top-left side of the plots. . . . .  | 46 |

|  |    |
|--|----|
| A.1 Schematic shows the locations of the radio sources for the +Z and -Z solutions of Equation 3.4. The Sun is located in the middle as an orange circle, with a horizontal dashed black line representing the POS. The vertical dashed green line represents the Sun-Earth LOS. The dashed blue and red circles represent the plasma spheres of density equivalent to the observation frequencies of the innermost and outermost radio sources at $R_1$ and $R_2$ , respectively, under the Newkirk model assumption of spherically-symmetric density distribution. The impact parameters $r_1$ and $r_2$ are the projection of $R_1$ and $R_2$ on the POS. The dot-dashed blue and red circles are the circles passing through the impact parameters $r_1$ and $r_2$ , respectively. . . . . | 53 |
| A.2 Cut of the flux density at 700 kHz observed by Wind (left panel) and STEREO-A (right panel). Note: for STEREO-A, there is no exact frequency channel at 700 kHz; therefore we selected the nearest one (675 kHz). . . . .  | 54 |

# Chapter 1

## Introduction

### 1.1 Background and Motivation

The Sun, an ordinary main-sequence star situated at the center of our Solar System, exhibits various forms of activity and variability on multiple spatial and temporal scales. One of the main manifestations of solar activity relevant to space weather research are transient energetic eruptive phenomena such as flares, Coronal Mass Ejections (CME), and wide-ranging emissions of electromagnetic radiation and energetic particles (Schwenn 2006; Pulkkinen 2007). These eruptive events originate due to the sudden release of free magnetic energy stored in complex, twisted or sheared magnetic field structures in the solar atmosphere (Moore et al. 2001; Priest & Forbes 2007; Zhang et al. 2012; Amari et al. 2014). The energetic phenomena are driven by the rapid dissipation of magnetic energy via magnetic reconnection which can accelerate large numbers of electrons to relativistic energies and heat plasma to tens of million Kelvin (Shibata & Magara 2011; Benz 2017).

The eruptive solar events drive major disturbances in the near-Earth space environment and planetary environments across the heliosphere, collectively termed space weather (Schrijver & Siscoe 2010a; Eastwood et al. 2017). Enhanced fluxes of solar energetic particles (SEPs), plasma ejecta, and electromagnetic radiation emitted during solar eruptions can impact the geomagnetic field, radiation belts, ionosphere, thermosphere, and upper atmosphere surrounding the Earth (Schwenn 2006; Pulkkinen 2007). Adverse effects range from disruption of radio communications to damage of satellites, power grid failures, aviation hazards due to radiation risks for airline crew and passengers, and increased radiation exposure for astronauts (Lanzerotti 2001). The societal dependence on space-based infrastructure has increased exponentially, escalating the vulnerability to space weather disturbances. Recent studies estimate a severe space weather event could lead to trillion-dollar economic damages in the US alone (Oughton et al. 2017). Besides the near-Earth space environment, solar eruptive transients also drive adverse space weather effects across the Solar System impacting activities such as deep space exploration and astronomy (Lilensten et al. 2014).

Therefore, advancing our understanding of the origins and propagation characteristics of solar eruptive phenomena, as well as quantifying their impacts on geospace and planetary environments, has become an extremely important pursuit for nations worldwide. Fundamental research seeks to uncover the physical processes involved using observations coupled with theory and modeling. Concurrently, significant efforts are underway to develop next-generation space environment modeling and forecasting capabilities for predicting the impacts of solar variability. The field combining these research and predictive aspects related to Sun-Earth connections is broadly termed heliophysics (Schrijver & Siscoe 2010b). It encompasses understanding the fundamental solar, heliospheric and geospace plasma processes; coupling across multiple spatial and temporal scales; quantifying the impacts on humanity's technological systems and space-borne assets; and utilizing this knowledge to prevent/mitigate adverse effects (Schrijver et al. 2015; Schrijver 2015). NASA's Living With a Star program and the National Science Foundation's Space Weather activities exemplify strategic efforts to advance scientific understanding and predictive capabilities across the interconnected domains of heliophysics (Brewer et al. 2002).

The present thesis focuses on studying several important phenomena related to solar eruptive activity and its impacts from the perspective of heliophysics research and space weather. The specific topics investigated include: (1) The propagation and evolution characteristics of large-scale coronal disturbances termed EUV waves that are triggered by solar flares and CMEs; (2) The generation, propagation and plasma characteristics of solar radio bursts emitted by accelerated electron beams traveling along open

magnetic field lines in the corona; (3) The forecasting of gradual solar energetic particle (SEP) events which constitute one of the major components of space radiation hazards at Earth.

These diverse topics are united by the common theme of seeking to uncover the origins and propagation mechanisms of key transient phenomena resulting from solar eruptions, utilizing observational data, analytical theory and modeling, and data science techniques. The phenomena have been studied for several decades using observations from multiple space missions, but gaps persist in our understanding of their underlying physics and space weather impacts. The thesis aims to provide new insights that help address some of the outstanding questions, guided by the overarching goals and framework of heliophysics research. The following sub-sections elaborate on the background, significance, observational challenges and knowledge gaps pertaining to each of the research topics investigated. The following subsection provide a concise overview of key literature related to the research topics investigated in the thesis. A detailed review is presented in each chapter specific to the respective phenomenon.

### 1.1.1 Coronal Waves

Coronal waves, or Coronal Bright Fronts (CBFs), also known as Extreme Ultra-Violet (EUV) waves, are large-scale arc-shaped bright fronts or disturbances observed propagating across significant portions of the solar corona following the eruption of CMEs and flares (Thompson et al. 1998; Nindos et al. 2008; Vršnak & Cliver 2008; Magdalenić et al. 2010; Veronig et al. 2010; Warmuth 2015). They are best observed in EUV and white-light coronal emission, as well as in radio wavelengths, spanning distances of up to several 100 Mm with speeds ranging from  $100\text{-}1000 \text{ km s}^{-1}$ , faster than the local characteristic speed in the solar corona, transforming into shock waves (Liu & Ofman 2014; ?; Thompson & Myers 2009; Nitta et al. 2013). These structures consist of piled-up plasma with higher density, making them appear brighter in white-light images.

The discovery of coronal waves dates back to observations obtained with the EIT instrument on SOHO launched in 1995, appearing as bright propagating fronts in 19.5 nm wavelength imaging of Fe XII emission lines formed at  $\sim 1.5 \text{ MK}$  plasma (Thompson et al. 1998). Subsequent studies based on SOHO/EIT and TRACE imaging found correlations between waves and CMEs, favoring an interpretation as fast-mode MHD waves driven by CME lateral expansions (Biesecker et al. 2002).

Since 2010, the initiation and evolution of coronal waves are being exquisitely observed with unprecedented resolution by the Atmospheric Imaging Assembly (AIA) on the Solar Dynamics Observatory (SDO) instrument (Lemen et al. 2012) across multiple EUV passbands sensitive to a wide temperature range (Nitta et al. 2013). Alternatively, shock waves can be indirectly observed through the detection of type II radio bursts, which are commonly associated with shock waves in the solar corona Vršnak & Cliver (2008). The AIA instrument has provided valuable insights into the dynamics of the low solar corona over the past decade, thanks to its exceptional spatial and temporal resolution. Equipped with telescopes observing the solar disk in bands 193 and 211 Å, the AIA instrument has demonstrated its ability to distinguish compressive waves in the lower corona Patsourakos et al. (2010); Ma et al. (2011); Kozarev et al. (2011). These observations offer valuable information about the kinematics and geometric structure of CBFs. To accurately study the evolution of the wave's leading front, observations off the solar limb are preferred to mitigate projection effects, which may introduce ambiguities in estimating time-dependent positions and the global structure of the wave Kozarev et al. (2015).

In situ observations of shock waves have revealed their classification into quasi-parallel, quasi-perpendicular, sub-critical, and super-critical shocks based on the angle between the wavefront normal vector and the upstream magnetic field lines Tsurutani (1985). Quasi-parallel shocks have an angle ( $\theta_{BN}$ ) smaller than  $45^\circ$ , while quasi-perpendicular shocks have  $\theta_{BN}$  greater than  $45^\circ$ . Supercritical shocks, often associated with accelerated particles, are promising candidates for generating type II radio bursts Benz & Thejappa (1988). However, obtaining accurate estimates of shock strength and obliquity solely from remote observations is challenging.

Coronal waves exhibit diverse morphology and kinematics ranging from circular fronts to narrow jets or expanding dome-like structures (Veronig et al. 2010). A taxonomy of wave properties based on extensive observational surveys can be found in papers by Muhr et al. (2014) and Nitta et al. (2013). However, despite being observed for over two decades since their serendipitous discovery, fundamental questions remain regarding the physical nature and drivers of coronal waves (Chen 2016; Vršnak & Cliver 2008; Warmuth 2015). The debate centers around two competing interpretations - the wave versus pseudo-wave (or non-wave) models. The wave models envisage coronal waves as fast-mode MHD waves or shocks that propagate freely after being launched by a CME lateral over-expansion or an initial flare pressure pulse (Wills-Davey et al. 2007; Vršnak & Cliver 2008). The pseudo-wave models interpret

them as bright fronts produced by magnetic field restructuring related to the CME lift-off process rather than a true wave disturbance (Delannée & Aulanier 1999; Chen et al. 2002). Extensive observational and modeling studies have been undertaken to evaluate the two paradigms (Patsourakos & Vourlidas 2012; Long et al. 2017), but a consensus remains elusive. Addressing these outstanding questions related to the nature and origin of coronal waves is imperative, since they are being incorporated into models as a primary agent producing SEP events and geomagnetic storms during CMEs (Rouillard et al. 2012; Park et al. 2013). Their use as a diagnostic tool for CME and shock kinematics predictions in these models requires discriminating between the different physical mechanisms proposed for their origin.

The present thesis undertakes an extensive statistical analysis of coronal EUV wave events observed by SDO to provide new insights into their kinematical properties and relationship to CMEs. We focus on analyzing their large-scale evolution as a function of distance and direction from the source region, leveraging the extensive EUV full-disk imaging capabilities of SDO spanning nearly a decade. Statistical surveys to date have mostly focused on initial speeds and morphological classifications rather than large-scale propagation characteristics. Our study aims to uncover systematic trends in their propagation kinematics using a significantly larger sample compared to previous works. We also comprehensively evaluate associations with CME and flare parameters in order to discriminate between wave and pseudo-wave origins. The results have important implications for incorporating coronal waves into predictive models of CMEs and SEP events for future space weather forecasting.

### 1.1.2 Solar Radio Bursts

Solar radio emissions have been the subject of extensive study and research due to their connection with solar activity and their potential impact on Earth's atmosphere and technology. One area of particular interest is solar radio bursts, which are intense bursts of electromagnetic radiation originating from the Sun. These bursts can be classified into different types based on their characteristics and associated phenomena. Solar radio bursts, including Type III bursts, serve as remote diagnostics for the study of energetic electrons within the solar corona. These bursts result from transient energetic electron beams injected into the corona, which then propagate along interplanetary magnetic field (IMF) lines (Ergun et al. 1998; ?; Reid 2020). As these electron beams traverse the corona, they induce plasma waves, also known as Langmuir waves, which subsequently transform into radio emission at the local plasma frequency or its harmonic components (Melrose 2017). The frequency of the radio emission is directly linked to the plasma density, making Type III bursts a valuable tool for investigating the inner heliosphere and understanding the underlying processes that drive solar active phenomena, such as solar flares and coronal mass ejections (Reid & Ratcliffe 2014; Kontar et al. 2017). These bursts offer insights into the acceleration of energetic electrons in the corona and their transport along magnetic field lines (Reid & Ratcliffe 2014). The generation of electromagnetic emission at radio frequencies through plasma emission mechanisms is a key aspect of solar radio bursts, shedding light on the dynamic interplay between non-thermal electron distributions and the ambient plasma (Melrose 1980).

In radio spectrograms, type III bursts manifest as intense enhancements of radio flux over background levels, exhibiting rapid frequency drifts over timescales ranging from seconds to minutes, signifying plasma dynamics (Reid & Vilmer 2017). These bursts are observable across a wide range of frequencies, spanning from GHz to kHz, and wavelengths extending from metric to decametric (Wild & McCready 1950; Lecacheux et al. 1989; Bonnin et al. 2008). This phenomenon is detectable by ground-based instruments on Earth as well as various spacecraft within the heliosphere, underscoring the significance of plasma dynamics in their manifestation.

Pioneering observations of solar radio bursts were made in the 1940s leading to their classifications (Wild et al. 1963). Subsequent spectrographic studies uncovered emission mechanisms, source regions and particle diagnostics (Suzuki & Dulk 1985). Magnetic reconnection models of flares provided theoretical explanations for particle acceleration generating radio bursts (Holman et al. 2011). Radio imaging spectroscopy using interferometric imaging arrays coupled with high time/frequency resolution spectrometers enables tracking radio sources as a function of frequency and position on the Sun, yielding particle acceleration locations and trajectories through the corona into interplanetary space (Krucker et al. 2011; Klassen et al. 2003a,b). This provides a unique diagnostic of energetic particle transport from the Sun to the Earth which is crucial for improving SEP forecasting models.

Different types of bursts are observed, classified based on their spectral characteristics as documented in radio burst catalogs (Wild et al. 1963). The present thesis focuses on detailed analysis of solar type III radio bursts and their associated phenomena (Reid & Ratcliffe 2014). Type III bursts appear as intense rapidly drifting emissions from high to low frequencies over seconds, corresponding to the propagation

of energetic electron beams from the low corona to beyond 1 AU along open field lines. They signify the initial escape of flare-accelerated electrons into interplanetary space, making them an important precursor signature of SEP activity (Cane et al. 2002; MacDowall et al. 2003). Investigating their source locations, plasma environments, and beam kinematics based on multi-wavelength observations coupled with plasma emission theory is therefore vital for improved understanding of coronal particle acceleration and transport processes relevant for SEP forecasting models.

While type III bursts have been studied for over 50 years since their initial discovery by Wild & McCready (1950); Wild (1950a,b), gaps persist in our understanding of their exciter beams and emission mechanisms. Key outstanding questions pertain to the detailed electron acceleration and injection sites, beam configurations and energy spectra, drivers of burst onset and duration, and the role of density fluctuations in propagating beams (Reid & Kontar 2018b,a; Li & Cairns 2012). Recent work combines imaging and spectral data with modeling to constrain radio burst excitors in unprecedented detail (?Kontar et al. 2017). Key challenges remain in reconciling emission models with observations and predicting radio diagnostics. Advancing our knowledge of these aspects through coordinated observations and modeling can help constrain the predictions of energetic electron properties based on radio diagnostics. The present work undertakes detailed investigation of a solar type III burst combining imaging and radio spectral data to derive electron beam trajectories and coronal densities, and models the emission sources. The results provide insights into the corona plasma environment and energetic electron transport relevant for SEP forecasting applications.

### 1.1.3 Solar Energetic Particle (SEP) Forecasting

Solar Energetic Protons (SEP) are high-energy particles that are believed to be originated from the acceleration of particles in the solar corona during coronal mass ejections (CMEs) and solar flares (Aschwanden 2002; Klein & Dalla 2017; Lin 2005, 2011; Kahler et al. 2017). They are typically characterized by their high energy levels - with some particles having energies in the relativistic GeV/nucleon range - and their ability to penetrate through spacecraft shielding, causing radiation damage (Reames 2013; Desai & Giacalone 2016). The fluence and energy spectrum of SEP are influenced by several factors, including the strength of the solar flare or CME that produced them, and the conditions of the interplanetary environment (Kahler et al. 1984, 1987; Debrunner et al. 1988; Miteva et al. 2013; Trottet et al. 2015; Dierckxsens et al. 2015; Le & Zhang 2017; Gopalswamy et al. 2017).

SEP exhibit a strong association with the solar cycle, with the frequency and flux of SEP events peaking during the maximum phase of the solar cycle (Reames 2013). This is thought to be due to the increased activity of the Sun during this phase, which leads to more frequent and powerful flares and CMEs. Previous studies have shown a relationship between the occurrence frequency of SEP and the sunspot number (SN; Nymmik, 2007; Richardson et al., 2016). However, the exact relationship between the solar cycle and SEP is complex and not fully understood. Hence, more work is needed to better understand this connection, as previous studies have reported intense SEP events during relatively weak solar activity (Cohen & Mewaldt 2018; Ramstad et al. 2018).

SEP have been a subject of interest and research in heliophysics for decades. It is hypothesized that shock waves generated in the corona can lead to an early acceleration of particles. However, SEP have sufficient energy to propagate themselves by *surfing* the interplanetary magnetic fields (IMF), and therefore, the expanding CME is not necessary for their transport (Reames 2000; Kóta et al. 2005; Kozarev et al. 2019, 2022). While this theory has gained acceptance, there is an ongoing debate among scientists over the specific mechanisms and conditions responsible for SEP production and acceleration.

The creation, acceleration, and transport mechanisms of SEP are complex and involve a combination of magnetic reconnection, shock acceleration, and wave-particle interactions (Li et al. 2003, 2012; Ng et al. 2012). The specific mechanisms responsible for SEP production and acceleration can vary depending on the type and strength of the solar event that triggered them. Further research is imperative to better understand the processes involved in the production and transport of SEP in the heliosphere. This will facilitate the development of more precise models that assist in minimizing the impact of SEP on astronauts and space-based assets.

The arrival of solar energetic particles (SEPs) in the near-Earth space environment constitutes one of the major components of adverse space weather (Reames 1999; Vainio et al. 2009). SEPs consist primarily of protons (and some heavy ions), accelerated to very high energies by CME-driven shock waves during large solar eruptive events. The gradual SEP events, so called due to their long durations from several hours to a few days, involve protons accelerated to energies above  $\sim 10$  MeV which can penetrate Earth's magnetic field and atmosphere posing radiation hazards to humans and equipment in

space and at polar regions (Reames 2013).

Initial SEP forecasting models were based on empirical correlations between proton intensity profiles and CME or flare properties (Kahler et al. 2007). The complex physics of CME shock acceleration combined with modeling the transport of SEPs through turbulent interplanetary magnetic fields presents major challenges for first-principles based SEP forecasting models (Aran et al. 2006; Laitinen & Dalla 2017). As an alternative approach, empirical and data-driven models based on statistical/machine learning techniques applied to historical SEP event data have shown considerable promise for operational forecasting over the past decade (Laurenza et al. 2009; Camporeale 2019; Kozarev et al. 2022). This motivates detailed investigation of data-driven SEP forecasting models using state-of-the-art machine learning algorithms which can outperform conventional empirical methods.

The emergence of deep learning techniques has enabled application of sophisticated machine learning models to SEP forecasting, yielding improved predictions since they can capture complex nonlinear relationships between parameters which has been leveraged for diverse space weather applications recently (Florios et al. 2018; Camporeale 2019). Opportunities exist for novel forecasting approaches utilizing deep learning algorithms and expanded input parameters. However, applications to SEP forecasting problems are still limited, presenting an important research gap which this thesis aims to address. In the present work, we develop a deep neural network model for predicting the intensity profile of  $>10$  MeV gradual SEP proton events utilizing near real-time solar wind plasma measurements as model inputs. The developed model is trained and tested on a database of historical SEP events spanning solar cycles 23 and 24, with the goal of producing SEP flux forecasts over an hour in advance of particle arrivals near Earth. Such capability can provide actionable information for mitigating radiation effects from extreme SEP events. The study demonstrates the potential of state-of-the-art machine learning algorithms to achieve significant enhancement of SEP forecasting capabilities building upon conventional empirical methods.

## 1.2 Objectives and Scope

The primary objectives and research questions addressed through the investigations carried out in this thesis include:

1. Characterize the large-scale propagation kinematics of coronal EUV waves over distances of hundreds of Mm from the eruption source location. Compare observed spatial and temporal variations in speeds with analytical CME-driven wave/shock models.
2. Conduct a comprehensive statistical analysis correlating properties of EUV waves with associated CME and flare parameters utilizing a large event sample. Discriminate between wave and pseudo-wave models based on observational evidence.
3. Analyze coordinated observations of a solar type III radio burst across imaging and radio spectral domains to derive coronal density profiles, electron beam kinematics and emission source models.
4. Develop a deep neural network model for forecasting the intensity profile of  $>10$  MeV gradual SEP proton events using real-time solar wind data as inputs. Evaluate model performance and forecast accuracy over different lead times.

The scope of the thesis encompasses key phenomena related to solar eruptions and their space weather impacts that align with the outstanding questions and challenges highlighted in the background discussion. While expansive in scope, some limitations exist that bound the present work:

- The studies rely primarily on remote sensing observations of the Sun and heliosphere, limited by measurement capabilities and resolution.
- Analytical modeling utilizes simplified theory and assumptions which cannot account for all complexities.
- Machine learning models have dependencies on data coverage and uncertainties in input parameters.
- Findings are constrained by the event samples studied and applicability to the broader population.

These factors imply appropriate care and diligence in interpretation of results and their generalizability. Nevertheless, the present work establishes an important foundation for future advances that can build upon these limitations.

## 1.3 Methodology Overview

The research presented in this thesis employs a synergistic methodology combining analytical theory, numerical modeling, and data science techniques. Both observational case studies and statistical analysis approaches are utilized for gaining new insights from application of these tools. The data sources, models, and algorithms employed in each of the investigations are concisely summarized below.

**Coronal waves:** The study utilizes an event database of  $\sim 60$  coronal EUV waves observed by SDO/AIA since 2010, tracking kinematics to  $30 R_{\odot}$  distances. Evolution trends are compared with analytical CME-driven wave propagation models. Statistical associations with CME and flare parameters provide corroboration for physical interpretation.

**Solar radio bursts:** Multi-wavelength observations of type III bursts from the LOFAR stations and Parker Solar Probe (PSP) are analyzed. Beam trajectories, densities, and emission sources are characterized by combining imaging data, plasma emission theory and coronal density models.

**SEP forecasting:** A database of  $>10$ ,  $>30$ , and  $>60$  MeV SEP integral fluxes during the last four solar cycles is generated using the GOES database. Deep neural network models are developed using solar wind data time-series as inputs. Model training, testing and validation is performed to evaluate forecast accuracy over different lead times.

This triangulation between data analysis, physics-based modeling and data-driven modeling provides confidence in the results obtained. Details of the methodological approaches are elaborated in their respective chapters.

## 1.4 Main Contributions

The primary contributions arising from the research presented in this thesis include:

- New large-scale kinematical characterization of coronal EUV waves propagating to distances over 100 Mm. Derived velocity and acceleration trends challenge steady-wave behavior assumed in models.
- Statistical analysis correlating EUV wave and CME/flare properties using a significantly larger event sample compared to prior studies. This enables stronger discrimination between competing initiation models.
- Novel methodology combining radio and EUV observations with analytical modeling to reconstruct plasma environments and electron beam trajectories for a solar type III radio burst.
- Deep learning forecasting model for intense SEP events using an expanded input parameter space based on solar wind data. This demonstrates cutting-edge artificial intelligence capabilities for space weather applications.
- Synergistic approach leveraging analytical theory, numerical modeling and data science techniques to gain new insights on long-standing problems in heliophysics research related to solar eruptions and their space weather impacts.

These contributions provide advances over prior state-of-the-art in the respective areas. They have implications for improving models used in operational space weather monitoring and forecasting systems, besides progressing fundamental physics understanding of solar and heliospheric phenomena. The results validate the merit of cross-disciplinary studies combining traditional analytical techniques with modern statistical and machine learning methods to enable discoveries from application of these synergies.

## 1.5 Outline

This thesis is divided into the following five chapters:

**Chapter 1 - Introduction:** Provides a background to the research topics, motivation and context of the work, summary of literature, overview of methodology, and the structure of the thesis.

**Chapter 2 – Propagation and Drivers of Coronal EUV Waves:** Presents a statistical analysis of the kinematics and physical interpretation of coronal waves using EUV imaging observations and analytical models.

**Chapter 3 – Plasma Environment and Energetics of a Solar Type III Radio Burst:** Details a multi-wavelength observational case study of a type III burst combining data analysis and modeling to probe the radio emission physics.

**Chapter 4 – Deep Learning Approach for Forecasting Intense SEP Events:** Describes the development and evaluation of a neural network model for predicting SEP properties using solar wind data.

**Chapter 5 – Conclusions and Future Outlook:** Summarizes the key findings, implications, and limitations of the research studies. Discusses future extensions building on the present work.

The core chapters 2 through 4 present the major research investigations carried out. The multi-faceted phenomena are studied by tailoring the methodology to leverage their key observational signatures. Together they provide new insights on different aspects of solar eruptions and space weather. Each chapter is structured to be reasonably self-contained, with relevant background and literature specific to the phenomenon under study. The findings are synergistic and united by the common thread of employing heliophysics principles to address outstanding questions using cutting-edge analytics.

## Chapter 2

# Characterization of Coronal Bright Fronts

### 2.1 Introduction

### 2.2 Observations

### 2.3 Data Analysis and Methods

### 2.4 Results and Discussion

### 2.5 Conclusions

### 2.6 Wavetrack: A Flexible Framework for Automated Recognition and Tracking of Wave-Like Events in Solar Imagery

#### 2.6.1 Overview

Solar eruptive events involve complex phenomena like flares, filament eruptions, coronal mass ejections (CMEs), and CME-driven shock waves. CME-driven shocks in the corona and interplanetary space are considered the primary accelerators of solar energetic particles (SEPs), mainly through diffusive shock acceleration (DSA) and shock drift acceleration (SDA) processes (Reames 2021). Substantial efforts have characterized and modeled SEP acceleration under ideal conditions (Vainio & Laitinen 2008; Sokolov et al. 2009; Kozarev et al. 2013). Recent work has focused on building more realistic CME-shock and SEP acceleration models using observational data (Vourlidas et al. 2012; Kwon et al. 2014; Kozarev et al. 2015, 2019).

Knowledge of CME-shock interactions with 3D coronal fields is critical for understanding SEP acceleration efficiency and spread Rouillard et al. (2016). DSA modeling requires deducing shock front shapes from observations since the local magnetic field-shock angle strongly affects acceleration Guo & Giacalone (2013). CMEs often over-expand laterally early on, altering the overall compressive front Bein et al. (2011); Temmer (2016). Thus, idealized shock surface descriptions used in modeling should be improved (Vourlidas et al. 2012; Kwon et al. 2014; Rouillard et al. 2016).

EUV imaging enables shock characterization, using instruments like STEREO/EUVI (Wuelser et al. 2004) and SDO/AIA (Lemen et al. 2012). Their resolution and multi-wavelength coverage allow time-dependent modeling of SEP acceleration (Kozarev & Schwadron 2016; Kozarev et al. 2017, 2019). Automated solar feature detection has increased due to Big Data demand. Fundamental techniques are reviewed in Aschwanden (2010) and applied for features at different heights (Pérez-Suárez et al. 2011). Some detect sunspots and active regions (Curto et al. 2008).

EUV wave recognition and tracking are challenging due to their weak intensity near other features. Algorithms exist but can be complex (Podladchikova & Berghmans 2005; Verbeeck et al. 2014; Long et al. 2014; Ireland et al. 2019). CorPITA (Long et al. 2014) and AWARE (Ireland et al. 2019) fit shapes

to flare-centered wave sectors, but use different images or persistence filters that introduce artifacts. They currently only work on the disk.

This paper presents Wavetrack - a flexible, object-oriented Python library for general solar feature detection and tracking. At its core combines multiscale representation (Starck & Murtagh 2002),  $\Delta$  trous wavelets (Akansu 1991; Holschneider et al. 1989), and filtering. Wavetrack can generate training sets for machine learning-based recognition.

Machine learning is increasingly applied in solar physics, like for EUV irradiance mapping (Szenicer et al. 2019), solar flare prediction (Li & Zhu 2013), and magnetic flux generation (Kim et al. 2019). However, data-driven CME tracking is limited by small training sets. Wavetrack can facilitate these by converting results into annotated sets.

At the core of Wavetrack is a general feature recognition and tracking method. It is implemented as an easy-to-integrate, open-source Python library. The modular structure allows configuring applications by tuning a few threshold parameters. The calculation scheme combines multiscale data representation (Starck & Murtagh 2002) and the  $\Delta$  trous wavelet transform (Akansu 1991; Holschneider et al. 1989). This is supplemented by image filtering techniques for noise removal and edge enhancement.

Wavetrack moves beyond complex existing algorithms that target specific phenomena. It provides a flexible framework for detecting various solar features in EUV, white light, and other observations. The modular design enables training set generation for machine learning approaches. Wavetrack facilitates automated analysis to uncover new knowledge from the wealth of solar data.

The  $\Delta$  trous wavelet transform enables isolating features at different scales. This allows separating noise from the signal and enhancing edges. The wavelet coefficients encode the multiscale structure efficiently. Thresholding coefficients suppress noise by zeroing insignificant values.

The filtering techniques refine the signal further. Morphological operations like opening remove artifacts and smooth edges. Contrast enhancement sharpens edges and boundaries. The result highlights features while suppressing noise.

Wavetrack takes advantage of these techniques to recognize faint features like EUV waves. It tracks them by identifying significant coefficients across wavelet scales. This avoids pre-processing like difference images that can introduce false signals.

The modular structure makes Wavetrack adaptable. Users can build specific applications by setting parameters like thresholds and filters. The original data is not altered, only the processed copies are used for feature detection. This prevents information loss.

Wavetrack will be open-source to facilitate community involvement. Users can contribute modules, optimizations, and new techniques. This collective effort will enhance solar data analysis capabilities for the Big Data era. Together we can uncover new knowledge to better understand our dynamic Sun.

Some techniques used for image processing and analysis in the context of solar observations include:

1. Wavelet Transform: The  $\Delta$  trous wavelet transform is a multi-scale data representation concept that is commonly used in solar image analysis. It allows for the extraction of features at different decomposition and intensity levels.
2. Image Filtering: Various image filtering techniques are employed to enhance and extract specific features in solar images. These techniques can help in detecting and tracking phenomena such as CME shock waves and filaments.
3. Feature Detection Algorithms: Automated algorithms are used to detect and identify solar features in different types of observations. These algorithms utilize image processing techniques to identify features like sunspot groups, active regions, and eruptive fronts.
4. Machine Learning: Machine learning methods, such as Convolutional Neural Networks (CNNs) and Generative Adversarial Networks (GANs), are increasingly being applied in solar image analysis. These techniques can be used for tasks like predicting solar flares or generating magnetic flux distributions.
5. Solar Feature Tracking: Tracking the evolution of solar features over time is an important aspect of image analysis. Tracking algorithms can be used to follow the movement and changes in features like CMEs, filaments, and EUV waves. These techniques and algorithms contribute to the understanding of solar phenomena and can aid in the development of models for solar activity and space weather forecasting.

The study utilized observations from the Atmospheric Imaging Assembly (AIA) instrument on the Solar Dynamics Observatory (SDO). The AIA instrument is an EUV imager that provides high-resolution and high-temporal observations of the Sun. The AIA instrument is particularly useful for detecting and characterizing large-scale shocks, known as EUV waves or Coronal Bright Fronts (CBFs). The study specifically focused on the AIA channels centered on 193 $\text{\AA}$  and 211 $\text{\AA}$  wavelengths. The 193 $\text{\AA}$  data was obtained using a standard AIA pipeline with the SunPy package. Base images were created by averaging a series of images prior to the eruption. Base difference images were then constructed by subtracting the base images from the current raw image of the sequence. This allowed for the enhancement of the change in intensity caused by CBFs, while omitting static details and reducing noise. The CBFs observed in

EUV are usually dim features that exist in a narrow part of the wide dynamic range of the raw image data. To overcome the challenge of recognizing and tracking these dim objects, the study pre-selected the part of the dynamic range where the shock wave is revealed from the base difference image of the sequence. Overall, the SDO/AIA telescope observations were utilized to study and track the CBFs and their evolution over time. The observations provided the necessary data to analyze the spatial and temporal relationships of the CBFs and other solar dynamic features.

The specific image filtering techniques used in the method include thresholding, wavelet decomposition, and segmentation. First, thresholding is applied to the absolute values of the pixels in the base difference images. This helps narrow the dynamic range of the image and focus on the segment where the object of interest is located. Next, the base difference images are decomposed using the  $\Delta$  trous wavelet technique into a series of scales. Each wavelet coefficient is then subjected to relative thresholding based on the statistical distribution of the pixel intensities at each decomposition level. After the segmentation process, object masks are obtained for each time step. These masks are then multiplied by the original data to reveal the intensity of different parts of the object. Overall, the method utilizes a combination of thresholding, wavelet decomposition, and segmentation to filter and analyze the images.

The statistical distributions of pixel intensities in base and running difference images can vary. In the case of base difference images, the pixel intensities are narrowed down to a specific segment where the object of interest is located, such as a coronal bright feature (CBF). The absolute values of the threshold interval are selected to focus on this segment. On the other hand, running difference images are used to determine the moment when an eruption starts. The statistical distribution of pixel intensities in these images depends on the specific features and objects being observed.

The multi-scale data representation concept, specifically the  $\Delta$  trous wavelet transform, contributes to the recognition and tracking of solar images by providing a hierarchical decomposition of the data. This allows for the extraction of certain objects and their masks from the imaging observations, enabling their tracking and evolution over time. The  $\Delta$  trous wavelet decomposition enhances the clarity and intensity of faint features in solar images, such as EUV waves, making them easier to detect and track. This methodology provides a flexible framework for solar feature detection and can be applied to various types of solar phenomena observed in different wavelengths. It offers a valuable tool for analyzing and understanding the dynamics of solar features, such as CME shock waves and filaments.

The purpose of the Wavetrack package mentioned in the document is to provide a method for the automated detection and tracking of dynamic coronal features in solar observations. It utilizes wavelet decomposition, feature enhancement and filtering, and object recomposition to identify and track features such as coronal bright fronts (CBFs) and eruptive filaments. The package is designed to work with both on-disk and off-limb features and can track features that split into separate parts over time. It is a flexible, object-oriented framework written in Python and is freely available for download and use.

Wavetrack uses AIA 193 $\text{\AA}$  images for tracking coronal waves. Wavetrack tracks coronal waves by utilizing wavelet decomposition, feature enhancement, and filtering techniques. It applies an  $\Delta$  trous wavelet decomposition method to the observational data, which enhances the clarity and intensity of faint features such as EUV waves. The algorithm convolves the image with different iterations of the wavelet filters, allowing it to capture different scales of features. After the wavelet decomposition, Wavetrack performs automated feature recognition by applying intensity thresholding, image posterization, median filtering, image segmentation, and intensity level splitting methods. These techniques help identify and isolate the coronal wave features in the data. The output of Wavetrack is a time-dependent pixel mask that represents the tracked coronal wave. This pixel mask can be applied to the original data to generate a final feature map. Wavetrack is capable of tracking both on-disk and off-limb features, and it can successfully track features that split into separate parts over time. Overall, Wavetrack combines wavelet decomposition and automated feature recognition to effectively track coronal waves in solar observations.

To track filaments using Wavetrack, the following process is followed: 1. Wavelet Decomposition: The observational data is decomposed using wavelet decomposition. This helps in identifying different scales of features in the image. 2. Feature Recognition: The decomposed image is processed using various techniques such as intensity thresholding, image posterization, median filtering, and image segmentation. These techniques enhance the features of interest, making them easier to track. 3. Object Mask Generation: The processed image is used to generate time-dependent feature pixel masks. These masks isolate the filament features in the image. 4. Image Recomposition: The image can be recomposed from the weighted wavelet scales after applying filtering techniques. This helps in obtaining a final feature map of the filaments. The type of images utilized for filament tracking depends on the source data and the velocity of the filaments. In general, inverted AIA 193 $\text{\AA}$  images are used for tracking filaments. These images provide better visibility of the filaments due to their distinct contours and lower dynamic range.

However, depending on the specific event and the characteristics of the filaments, other types of images such as Base Difference, Running Difference, or Raw Intensity data may also be used.

The FLCT model uses the Fourier Local Correlation Tracking (FLCT) method to calculate the plane-of-sky velocity and speed of solar features. This method involves analyzing consecutive images and tracking the motion of the features over time. The FLCT algorithm applies the FLCT method to the object masks generated by the Wavetrack code, resulting in detailed maps of the instantaneous velocity of the solar feature of interest. The velocity is represented by arrows indicating the direction of motion, while the speed is represented by the length of the arrows or through color mapping. The FLCT model provides valuable insights into the expansion and evolution of solar features such as Coronal Bright Fronts (CBFs) and erupting filaments.

The document presents several examples and case studies that demonstrate the application of the Wavetrack package. Here are some of the examples mentioned: 1. May 11, 2011 event: The Wavetrack algorithm was used to track both an erupting filament and the coronal bright front (CBF) it drives. The relationship between the driver and wave was studied using the segmented features from AIA 193Å observations. 2. September 29, 2013 event: Wavetrack was applied to a large-scale filament in a slow eruption. The segmented filament feature was overlaid on the solar corona, and the on-disk feature was consistently tracked during the eruption. 3. December 12, 2013 event: Wavetrack was used to track the evolution of driven and non-driven regions of the CBF. The method revealed the relation between the CBF and eruptive features. These examples demonstrate the versatility of Wavetrack in recognizing and tracking various solar features, both on the solar disk and off the solar limb.

For the June 07, 2011 event, the variation in speed between the geometric center (GC) and center of mass (CM) is up to 300 km/s in the radial direction. The angle between the GC and CM changes quite a lot as different parts of the compressive front brighten and dim. However, the angle remains relatively stable, changing only slightly during this event.

The main results of the paper are as follows: 1. The Wavetrack framework, which utilizes an  $\text{\AA}$  trous wavelet decomposition method, is effective in enhancing solar EUV and white light images and improving the clarity and intensity of faint features. 2. The Wavetrack method allows for the segmentation and tracking of solar dynamic features, such as coronal bright fronts (CBFs), over time. It provides a simple metric with a one-dimensional time series for characterizing the evolution of these features. 3. The Wavetrack framework is widely applicable to different types of solar dynamic features and different observational data. 4. The method has some limitations, such as the need for manual input in setting object criteria and fine-tuning parameters for specific events. These limitations will be addressed in future work. Overall, the Wavetrack framework provides a valuable tool for analyzing and tracking solar dynamic features in observational data.

The conclusions drawn from the study are as follows: 1. The Wavetrack method is effective in segmenting and tracking solar dynamic features, such as coronal bright fronts (CBFs) and filaments, in observational data. 2. The Wavetrack method allows for the analysis of feature evolution over time by calculating the time-dependent vector between the pixel geometric center and the center of mass. 3. The method can successfully capture the extent of CBFs in consecutive time steps, even in regions with different pixel distributions and intensities. 4. Wavetrack is capable of tracking multiple separate parts of the same feature. 5. The method is widely applicable to different types of solar dynamic features and different observational data. 6. The limitations of the method, such as the need for manual input in setting object criteria and fine-tuning parameters for specific events, will be addressed in future work.

## 2.7 Geomagnetic Storms: CME Speed De-Projection vs. In Situ Analysis

This study, led by Miteva et al. (2023), examines the relationship between the intensity of geomagnetic storms (GS) and parameters of solar and interplanetary phenomena. We utilize the recently developed PyThea framework to reconstruct the 3D geometry of geo-effective CMEs and compare on-sky and de-projected values, focusing on the reliability of the de-projection capabilities. Spheroid, ellipsoid, and graduated cylindrical shell models are used. We collected parameters of the GS-associated phenomena. Considerable variation in 3D de-projections of CME speeds was obtained depending on the reconstruction model chosen and subjective observations. Fast CME speeds combined with frontal magnetic structure orientation when reaching Earth's magnetosphere proved the best indicator of GS strength. More accurate estimations of geometry, direction, and de-projected speeds are critical for operational GS forecasting in space weather prediction schemes.

### 2.7.1 Overview

Solar eruptive events like coronal mass ejections (CMEs) and solar flares (SFs) can generate disturbances that propagate through interplanetary space and impact Earth's magnetosphere, leading to space weather effects (Fletcher et al. 2011; Webb & Howard 2012; Klein & Dalla 2017; Temmer 2021). The electromagnetic radiation from SFs arrives at Earth first, followed by energetic particles. The plasma clouds of CMEs take longer, from tens of hours up to a few days, to impact Earth's environment (Malandraki & Crosby 2018; Gopalswamy 2022). The temporary disruption of Earth's magnetosphere and atmosphere due to these solar events are known as geomagnetic storms (GSs) (Gonzalez et al. 1994; Saiz et al. 2013; Lakhina & Tsurutani 2016).

The coupling between solar wind plasma and Earth's magnetosphere occurs through magnetic reconnection, enabled when the interplanetary (IP) magnetic field turns southward (negative  $B_z$  component) and impacts Earth at high speed, as during CMEs (Dungey 1961; Akasofu 1981; Echer & Gonzalez 2022). This leads to increased particle injection into the magnetosphere and atmosphere, causing bright auroral displays. Drifting electrons and protons also drive the westward ring current responsible for decreases in the horizontal magnetic field measured by the disturbance storm time (Dst) index (Gonzalez et al. 1994; Saiz et al. 2013; Lakhina & Tsurutani 2016).

Fast CMEs propagating through IP space (ICMEs) cause the most intense GSs, with sudden Dst decreases, compared to gradual storms from corotating interaction regions (CIRs) (Tsurutani et al. 1997; Zhang et al. 2007; Wu & Lepping 2016; Borovsky & Denton 2006). ICME shock waves and magnetic ejecta produce cascading effects in near-Earth space that can disrupt technology (Pulkkinen 2007).

Earth-directed fast ejecta with strong southward magnetic fields inside are the most geoeffective. However, single spacecraft observations are limited by projection effects, leading to uncertain CME speed estimations (Paouris et al. 2021; Kouloumvakos et al. 2022). Previous studies found no clear relationship between GS intensity and solar flare parameters or CME properties like projected speed and angular width (Samwel & Miteva 2023). Furthermore, CME magnetic structure cannot be derived from remote sensing data. Reliable solar or near-Sun measurements that provide early warnings for potential GS strength remain lacking.

Accurately predicting when an incoming disturbance will impact Earth requires determining the arrival time and speed of CMEs. Different portions of these large structures, such as the apex or flanks, can hit Earth upon arrival at 1 AU. Flank hits may only involve the CME sheath while apex hits include both sheath and ejecta, leading to different magnetospheric effects (Kay & Gopalswamy 2018). Therefore, deducing CME directionality and 3D geometry is important. To maximize forecast lead time, these parameters should be estimated as early as possible when the CME emerges in coronagraph fields of view. In images, CMEs appear as line-of-sight integrated brightness enhancements projected onto the observing plane (Vourlidas et al. 2003; Jackson et al. 2010).

Further developing reconstruction techniques to correct for projection effects can improve CME propagation understanding and impact forecasting (Thernisien et al. 2009; Mierla et al. 2010; Wood et al. 2010; Thernisien 2011). Several CME propagation models exist (Odstrcil et al. 2004; Xie et al. 2004; Vršnak et al. 2013; Pomoell & Poedts 2018). A study found 2D CME speeds underestimate 3D speeds by  $\sim 20\%$  while 2D widths overestimate 3D widths (Jang et al. 2016). Another study showed observer bias in 3D modeling using graduated cylindrical shells, even for experienced observers (Verbeke et al. 2022). CME structure interpretation differs, and line-of-sight integration leads to non-unique solutions.

This study focuses on deducing CME directionality and near-Sun speeds using new tools like PyThea (Kouloumvakos et al. 2022). We analyze geo-effective cycle 24 CMEs using multiple reconstruction techniques by two team members. Comparisons are made between derived parameters and storm intensity (Dst). CME speed correlations with ICME and IP shock speeds evaluate 3D de-projection value for arrival forecasting. Other IP parameters are also examined, including shock speed, plasma jumps, and magnetic fields near L1. We examine the correlation between the intensity of geomagnetic storms and parameters of solar and interplanetary phenomena. More specifically, we focus on the speed and geometry of CMEs, as well as interplanetary shocks, as these factors are known to play a significant role in the occurrence and intensity of geomagnetic storms. The objective of the study is to analyze the correlations between the intensity of geomagnetic storms (GS) and parameters of solar and interplanetary (IP) phenomena. The study also aims to perform 3D geometry reconstructions of geo-effective coronal mass ejections (CMEs) using the PyThea framework and compare the de-projected CME speeds with in situ data.

## 2.7.2 Data Analysis and Methods

The event selection process for this investigation commenced with the identification of significant Geomagnetic Storms (GSs) within Solar Cycle 24 (SC24). These storms were characterized by a Dst index exceeding 100 nT, as per the classification outlined in [7]. A total of 25 GSs were identified, with Dst indices ranging from 101 to 234 nT. Previous studies have explored the solar and Interplanetary (IP) origins of these GSs in SC24 [34–37]. However, the comprehensive review of all pertinent literature falls beyond the purview of this study. It is noteworthy that SC24 exhibited a reduced number of GSs in comparison to preceding solar cycles [38].

In our investigation, distinct from prior analyses, our objective was to establish a causal connection between the identified GSs and potential IP and/or solar phenomena. This approach mirrors methodologies employed by other researchers [14,39–42]. To delineate the solar and IP drivers, we employed an association procedure widely acknowledged in the field of Space Weather (SW) research. The methodology involves searching for the IP and solar origins of a GS storm within a specific timeframe preceding the reported GS occurrence at Earth. The sequential steps of our approach are delineated below:

1. **Temporal Association with IP and ICME Events:** We initiated the analysis with a temporal association between the GS and recorded IP shocks in the vicinity of Earth. This association was established within a 1-day period preceding the reported minimum Dst of the GS. A parallel procedure was employed for the association with Interplanetary Coronal Mass Ejections (ICMEs) reported in proximity to Earth. Additionally, animations from <http://helioweb.net/archive/> (accessed on 5 April 2023) were utilized to validate potential ICME and IP shock candidates.

2. **Association with Coronal Mass Ejections (CMEs):** Subsequently, we extended the association to include Coronal Mass Ejections (CMEs) within a 3-to-5 day window prior to the IP (or GS) timing. Information from available solar and IP event catalogs, as well as animations from <http://helioweb.net/archive/> (accessed on 5 April 2023), was employed for this purpose.

3. **Completion of the Association with Solar Flares (SFs):** The final step involved associating the GS with the identification of a Solar Flare (SF) linked to the previously associated CME. This association was based on timing (within one hour between the SF onset and CME timing) and location constraints (the SF location had to align with the solar quadrant reported in the measurement position angle, MPA, of the CME).

All utilized databases, catalogs, and publicly available lists pertinent to the analysis are summarized as follows:

- GS database (Kyoto): [<https://wdc.kugi.kyoto-u.ac.jp/dstdir/index.html>] (<https://wdc.kugi.kyoto-u.ac.jp/dstdir/index.html>) (accessed on 5 April 2023)
- SF database (GOES): [<http://ftp.swpc.noaa.gov/pub/warehouse/>] (<http://ftp.swpc.noaa.gov/pub/warehouse/>) (accessed on 5 April 2023)
- CME catalog (SOHO-LASCO): [<https://cdaw.gsfc.nasa.gov/CMElist/>] (<https://cdaw.gsfc.nasa.gov/CMElist/>) (accessed on 5 April 2023)
- ICME database: [<https://wind.nasa.gov/ICMEcatalog/>] (<https://wind.nasa.gov/ICMEcatalog/>)
- Wind database: [[https://wind.nasa.gov/ICMEcatalog/ICME\\_catalog\\_viewer.php](https://wind.nasa.gov/ICMEcatalog/ICME_catalog_viewer.php)] ([https://wind.nasa.gov/ICMEcatalog/ICME\\_catalog\\_viewer.php](https://wind.nasa.gov/ICMEcatalog/ICME_catalog_viewer.php)) (accessed on 5 April 2023)
- ACE database: [<http://izw1.caltech.edu/ACE/ASC/DATA/level3/icmetable2.htm>] (<http://izw1.caltech.edu/ACE/ASC/DATA/level3/icmetable2.htm>) (accessed on 5 April 2023)
- IP shock database: [<http://www.ipshocks.fi/database>] (<http://www.ipshocks.fi/database>) (accessed on 5 April 2023)
- LWEBC database: [<https://lweb.cfa.harvard.edu/shocks/widata/>] (<https://lweb.cfa.harvard.edu/shocks/widata/>) (accessed on 5 April 2023)

## GSs and IP Phenomena

The findings pertaining to Geomagnetic Storms (GSs) and their associated Interplanetary Coronal Mass Ejections (ICMEs) and Interplanetary (IP) shocks are succinctly presented in Table 1. The initial column designates the event number (), a consistent reference utilized throughout this paper. Columns (2) and (3) detail the GS date, hour (mm-dd/hr), and the corresponding Dst index (in nT). Subsequently, columns (4)–(6) expound upon the ICME parameters [43], drawing from the Wind database accessible at [https://wind.nasa.gov/ICMEcatalog/ICMEcatalog\\_viewer.php](https://wind.nasa.gov/ICMEcatalog/ICMEcatalog_viewer.php) (accessed on 5 April 2023). The sheath duration ( $D$ , in hours)

Column (8) integrates the minimum  $B_z$  component throughout the Interplanetary Coronal Mass Ejection (ICME) duration, as ascertained from the data available at <https://cdaweb.gsfc.nasa.gov/> (accessed on 5 April 2023), thereby enhancing the comprehensiveness of the dataset. In Column (9), we conduct a qualitative assessment of the ICME arrival orientation. Specifically, we visually inspect the intersection point between the ICME structure and Earth using ecliptic plane animations accessible at <http://helioweb.net/archive/> (accessed on 5 April 2023). The orientations are denoted as either 'hit' (nose) or 'f' (flank) arrivals. Instances of discrepancies among diverse data sources, such as the presence of solar wind streams or Corotating Interaction Regions (CIRs) visible in animations contradicting ICME arrivals identified through in situ data, are marked as 'u' (uncertain) in the same column. This classification signifies situations where a distinct ICME structure propagating through the Interplanetary

(IP) space could not be conclusively observed. Noteworthy is the occurrence of swift solar wind flows and/or CIRs recorded near Earth during ICME and/or shock wave events. For instance, in the cases of E11 and E18, a CIR was identified as their IP origin by [35]; however, in contrast to these findings, our methodology does not differentiate between ICME and sheath origins.

The final columns, (10)–(13), enumerate the properties of the IP shock, incorporating timing, speed, magnetic field, density, temperature jump at the shock interface, and the Mach number (Mms). These details are sourced from Wind satellite data, <http://www.ipshocks.fi/database> (accessed on 5 April 2023), with the exception of E24, where the median shock speed is derived from <https://lweb.cfa.harvard.edu/shocks/widata/> (accessed on 5 April 2023).

## GSs and Solar Phenomena

In the context of five cases denoted as E05, E11, E17, E18, and E22, our attempts to identify Solar Flares (SFs) or Coronal Mass Ejections (CMEs) were unsuccessful. Furthermore, in an additional six cases, the specification of SFs proved unattainable. The ensuing presentation provides details on the parameters of the remaining cases, specifically focusing on the solar origins associated with Geomagnetic Storms (GSs), as outlined in Table 2.

Columns (2)–(5) of Table 2 elucidate the properties of the GS-associated SFs, while columns (6) to (9) furnish the parameters of the GS-associated CMEs. The identified SFs exhibit a range of magnitudes from C1.2 to X5.4 and are predominantly positioned proximate to the solar disk center, with the exception of E02 and E03. The CMEs associated with these events possess on-sky projected speeds, denoted as 2D, spanning from 126 to 2684 km/s, extracted from the SOHO-LASCO CDAW catalog. Notably, the majority of the GS-associated CMEs (15 out of 20) exhibit a halo configuration, while three others are in close proximity to halo.

It is imperative to note that events with uncertain CME origins have been excluded from the subsequent 3D analyses. Specifically, in the case of E07, the unique orientation of the double CME rendered the de-projection procedure unfeasible for the same CME structure, leading to its exclusion from the 3D analyses. Additionally, for seven other cases (E12, E14–E16, E19, E23, E25), the online tool utilized for analyses failed to retrieve data simultaneously from both spacecraft. Consequently, these cases have also been omitted from the 3D analyses.

For the remaining 12 cases, successful 3D CME speed reconstructions were achieved from each model. The mean values, based on 2 or 4 available fits (as detailed in the subsequent subsection), are presented in the concluding columns (10)–(12) of Table 2. This comprehensive overview provides a foundation for the subsequent analytical discussions, offering a detailed characterization of the solar events associated with the studied GSs.

## PyThea 3D De-Projection Tool

The de-projection methodology employed in this investigation relies on the innovative PyThea online tool designed for the 3D reconstruction of Coronal Mass Ejections (CMEs) and shock waves [19]. All three available models within PyThea, namely spheroid, ellipsoid, and GCS, are applied in this study. The fitting procedure is conducted independently by two observers within our team. Figure 1 presents an illustrative example of the fits for event E03.

Upon scrutinizing the fitting outcomes for this particular example, it becomes evident that the reconstructions exhibit a discernible bias. The observer's subjective 'choice' of structures to align with the model introduces a level of variability. In the top row of Figure 1, distinct shock-related structures (manifested as the bending of streamers) are observed, upon which the idealized Geocentric Solar Coordinates (GCS) flux rope geometry is fitted. Consequently, there is a likelihood of overestimating the CME width. Despite this bias, it is noteworthy that the overall results, including directivity and speed for event E03, are minimally impacted. However, it is acknowledged that the complexity of structure choices can lead to larger discrepancies among different observers.

This study places emphasis on deriving de-projected CME speeds based on fits conducted at two distinct time steps. For each of the three models, the initial CME longitude and latitude are manually specified, utilizing the provided locations of the CME-accompanied Solar Flares (SFs). It is important to note that these values exhibit minimal to no substantial changes post-finalization of the fitting procedure. Consequently, the final CME directivity provided by PyThea is considered to be a relatively crude estimate. The ultimate orientations of the CME in Interplanetary (IP) space and at Earth are derived solely from qualitative information extracted from animations available at <http://helioweb.net/archive/> (accessed on 5 April 2023). This approach ensures a rigorous and consistent basis for evaluating the de-projected CME speeds in our analyses.

### 2.7.3 Results and Discussions

The main results of the study include correlations between the intensity of geomagnetic storms and parameters of solar and interplanetary phenomena. The study also involves the 3D reconstruction of geo-effective coronal mass ejections (CMEs) using the PyThea framework. The researchers analyzed the de-projection of CME speeds and compared them with in situ data. The study provides insights into the relationship between CME properties and geomagnetic storm intensity.

The main findings of the study on the correlations between solar and interplanetary phenomena and the intensity of geomagnetic storms are as follows:

1. The study found moderate positive correlations between the plasma compression parameters at the shock interface and the intensity of geomagnetic storms, as measured by the Dst index. These correlations were similar to or slightly larger than those obtained when interplanetary magnetic cloud speeds were used instead.

2. Interestingly, the study found that the correlation between the intensity of geomagnetic storms and the  $-B_z-$  component (minimum value during the ICME duration) was weaker compared to previous studies.

3. The study also reported strong correlations between the intensity of geomagnetic storms and different components of the electric and magnetic fields. However, these correlations were not analyzed in detail in the study.

4. It is important to note that the study did not calculate uncertainty estimates for the correlation coefficients, so the results should be interpreted with caution.

In conclusion, the study found moderate positive correlations between the intensity of geomagnetic storms and the plasma compression parameters at the shock interface. These findings contribute to our understanding of the relationship between solar and interplanetary phenomena and the occurrence of geomagnetic storms.

In the study, the comparison between the observed projected CME speeds and the CME speeds derived from PyThea showed that the correlation coefficient could be improved from 0.04 (using LASCO data) to 0.34-0.55 (using different geometrical models provided by PyThea). However, it was found that fast CMEs tend to have larger speed errors when applying different CME geometry reconstruction techniques.

There are correlations between space weather parameters during intense geomagnetic storms. Intense geomagnetic storms have been found to exhibit correlations with certain space weather parameters. According to the study mentioned in the context, correlations have been observed between the intensity of geomagnetic storms (measured by the Dst index) and parameters of solar and interplanetary phenomena. These correlations include:

1. Correlations with plasma compression parameters at the shock interface: The study found a moderately positive correlation between the downstream to upstream ratio of plasma compression parameters at the shock interface and the Dst index. This indicates that the intensity of geomagnetic storms is moderately correlated with the plasma compression at the shock interface.

2. Correlations with ICME speeds: Intense geomagnetic storms have also shown correlations with interplanetary coronal mass ejection (ICME) speeds. The study found that the ICME speeds, measured by spacecraft like Wind and ACE, exhibit correlations with the Dst index.

It is important to note that these correlations were observed in a small sample of geomagnetic storms and caution should be exercised when interpreting the results. Additionally, the study did not provide uncertainty estimates for the correlation coefficients.

### 2.7.4 Conclusions

The study found that certain parameters of solar and interplanetary phenomena show a positive correlation with the intensity of geomagnetic storms (GS). Specifically, the combination of the speed and orientation of the magnetic obstacle (nose-like) of coronal mass ejections (CMEs) seemed to have a positive feedback on the strength of the geomagnetic storm. However, other parameters such as CME speed, magnetic field, temperature, and density jump at the shock profile showed only moderate correlations with the geomagnetic storm intensity. The study also highlighted the importance of reliable estimation of the CME speed distribution over the entire CME structure for better modeling of CME propagation and forecasting of geomagnetic storms.

The significance of 3D de-projection efforts for CME arrival and GS forecasting is that it allows for a more accurate estimation of the direction and speed of coronal mass ejections (CMEs) as they approach Earth. By de-projecting the 3D geometry of CMEs, researchers can determine the true speed

and trajectory of these large-scale structures, which is crucial for forecasting their potential impacts on Earth's geomagnetic storm (GS) intensity. This information helps in predicting the arrival time and intensity of the CMEs, providing valuable insights for space weather forecasting and mitigation efforts.

Additionally, 3D de-projection efforts help in distinguishing different parts of CMEs that might hit Earth, such as the apex or flanks. These different parts can lead to different processes in Earth's atmospheric layers, and accurately determining the CME directivity and geometry aids in understanding the specific effects and potential hazards associated with each type of CME impact.

Overall, reliable estimation of the 3D speed and directivity of CMEs through de-projection efforts is essential for improving the accuracy of CME arrival and GS forecasting, enabling better preparedness and mitigation strategies for potential space weather impacts.

3D de-projection is important for forecasting the arrival of coronal mass ejections (CMEs) and predicting the intensity of geomagnetic storms (GS) because it allows for a more accurate estimation of the CME's direction, geometry, and speed. When a CME reaches Earth, different parts of it can hit different regions, leading to varying effects on the Earth's atmospheric layers. By accurately determining the CME's directivity and geometry, scientists can better understand its propagation in interplanetary space and predict its potential impacts on Earth.

Projection effects occur when observing CMEs from Earth, as they appear as line-of-sight integrated intensity enhancements projected onto the plane-of-sky of the observing instrument. This projection can distort the true shape and speed of the CME. By de-projecting the observed data and reconstructing the CME's 3D geometry, scientists can correct for these projection effects and obtain a more reliable estimate of the CME's speed and arrival time.

Accurate estimation of the CME's speed and arrival time is crucial for space weather forecasting. It allows for early prediction of potential impacts on Earth, providing valuable lead time for preparations and mitigating the effects of geomagnetic storms. Additionally, understanding the geometry and directivity of CMEs helps in determining the specific processes that occur in the Earth's atmospheric layers during different types of CME hits.

In summary, 3D de-projection is important for forecasting the arrival of CMEs and predicting the intensity of geomagnetic storms because it improves the accuracy of estimating the CME's direction, geometry, and speed, which are essential parameters for assessing their potential impacts on Earth.

Different CME geometry reconstruction techniques can have an impact on the accuracy of CME speed measurements. In particular, fast CMEs tend to be more prone to large speed errors when using these techniques. This is likely due to the complexity in choosing the coronal structures that become visible as a result of the rapidly expanding magnetic structure of the CME. Additionally, for fast halo CMEs, there may be significant deviations in the reconstruction quality due to the overlap of shock and magnetic structure components. Therefore, the accuracy of CME speed measurements can be affected by the choice of reconstruction technique, especially for fast events.

Using remote sensing image data for early warnings about potential geomagnetic storm onsets and strength has certain limitations. Here are some of the limitations:

1. Projection Effects: Remote sensing measurements from a single spacecraft are subject to projection effects. This means that the observed parameters, such as CME speed, can be influenced by the viewing angle and may not accurately represent the true values. This can lead to uncertainties in the estimation of CME properties and their impact on Earth.

2. Speed Estimations: Estimating the speed of a CME from remote sensing image data can be challenging. Different techniques and models are used to reconstruct the 3D geometry of CMEs, but they can introduce errors and uncertainties in the speed estimation. Especially for fast CMEs, the speed errors can be significant.

3. Lack of Magnetic Field Information: Remote sensing image data alone cannot provide information about the magnetic field structure of CMEs. The strength and orientation of the magnetic field within a CME play a crucial role in determining its impact on Earth's magnetosphere. Without this information, it is difficult to accurately predict the strength of the associated geomagnetic storm.

4. Limited Coverage: Remote sensing instruments are typically located on specific spacecraft, which may have limited coverage of the Sun-Earth space. This can result in gaps in the observations and make it challenging to track and predict the propagation of CMEs and their interaction with the interplanetary medium.

5. Uncertainties in Arrival Time Prediction: Predicting the arrival time of a CME at Earth based solely on remote sensing image data can be challenging. Factors such as the interaction with the solar wind and the presence of other solar or interplanetary disturbances can affect the propagation speed and trajectory of CMEs, leading to uncertainties in arrival time predictions.

It is important to consider these limitations when using remote sensing image data for early warnings about potential geomagnetic storm onsets and strength. Integrating multiple data sources and models can help improve the accuracy of predictions and provide a more comprehensive understanding of the space weather conditions.

The study's findings have potential implications for space weather forecasting by improving the accuracy of predicting geomagnetic storms (GS) and their intensity. By analyzing the correlations between the intensity of GS and parameters of solar and interplanetary phenomena, the study aims to derive reliable solar or near-Sun parameters that can be used for early warnings about potential GS onsets and strength. The use of newly developed tools for CME de-projection, such as the PyThea software package, allows for the reconstruction of the 3D structure of coronal mass ejections (CMEs) and shock waves, which can provide more accurate information for space weather forecasting. Additionally, the study highlights the importance of considering different CME geometry reconstruction techniques to improve the accuracy of predicting fast CMEs, which are particularly prone to large speed errors. Overall, the findings of this study contribute to the advancement of space weather forecasting and the ability to predict and mitigate the potential impacts of geomagnetic storms on Earth.

The study provides valuable insights into the relationship between geomagnetic storms and solar/interplanetary factors. It examines correlations between the intensity of geomagnetic storms and parameters of solar and interplanetary phenomena. The study also includes 3D geometry reconstructions of geo-effective coronal mass ejections (CMEs) and compares on-sky and de-projected parameter values. The researchers found that a combination of fast speed and frontal orientation of the magnetic structure upon its arrival at the terrestrial magnetosphere is the best indicator for the strength of a geomagnetic storm. The study emphasizes the importance of more reliable estimations of geometry, directivity, and de-projected speeds for geomagnetic storm forecasting in operational space weather schemes.

# Chapter 3

## Solar Radio Observations: Integrating Space-based and Ground-based Data for Coronal Diagnostics

In this chapter, I focus on multi-wavelength observations of solar type III radio bursts, as well as modeling studies of plasma parameters and coronal magnetic fields, to gain insights into the mechanism of solar radio emission during quiet times and the coronal conditions influencing the propagation and detection of these bursts. First, I briefly introduce the characteristics of solar type III radio bursts. I then present the data I have worked with, detailing the multiple processing stages I undertook. Finally, I present my outputs and interpret their meaning.

### 3.1 Introduction

Type III radio bursts are manifestations of transient energetic electron beams injected into the solar corona, propagating along the interplanetary magnetic field (IMF) lines Ergun et al. (1998); Pick (2006); Reid (2020). As these beams traverse the corona, they trigger plasma waves (also known as Langmuir waves) that are then transformed into radio emission at the local plasma frequency or its harmonic components Melrose (2017). In the radio spectrograms, type III bursts are usually observed as intense emissions that drift in frequency over timescales of several seconds to minutes and over a wide range of frequencies, from metric to decametric wavelengths Wild & McCready (1950); Lecacheux et al. (1989); Bonnin et al. (2008), making them detectable by ground-based instruments on Earth and various spacecraft within the heliosphere. The frequency of the radio emission is directly related to the plasma density, making type III bursts a valuable diagnostic tool for examining the inner heliosphere and the processes that drive solar active phenomena, such as solar flares and coronal mass ejections Reid & Ratcliffe (2014); Kontar et al. (2017).

The electron beams follow open magnetic field lines and can persist well beyond 1 astronomical unit (AU) (e.g., Dulk et al. (1985); Boudjada et al. (2020)), offering in situ insights into the burst and ambient conditions of the heliosphere, including electron density, radio frequency drift, speed of the electron beams and even potential direct detection of Langmuir waves (see Gurnett & Anderson (1976, 1977) and Reid & Ratcliffe (2014) and references within). In addition, tracing the path of type III bursts provides a map of the density structure of the heliosphere, serving as a foundation for developing and testing density models. Since radio observations below  $\sim 10$  MHz cannot be accomplished from the ground, it is important to combine high- and low-frequency observations from ground-based and space-borne instruments. In this work, I perform a study of several type III radio bursts that occurred in close succession on April 3, 2019. I use remote observations of type III radio bursts detected by the Low-Frequency Array (van Haarlem et al. 2013, LOFAR) ground-based radio telescope and the Parker Solar Probe (Fox et al. 2016, PSP) spacecraft during Encounter 2 to study the sources of these radio emissions and to investigate the physical conditions responsible for their generation. Additionally, I incorporate results of two steady-state models of the solar corona: the potential field source surface (PFSS) model Altschuler & Newkirk

(1969); Schatten et al. (1969) and the magnetohydrodynamic algorithm outside a sphere (MAS) model Mikić et al. (1999), to gain a better understanding of the coronal magnetic environment and its role in the acceleration of electrons. The ground-based LOFAR imaging observations provide valuable insight into the actual location of the burst sources. This research aims to expand upon current knowledge of the electron beams responsible for triggering type III radio bursts and the coronal conditions they experience. Gaining a deeper insight into this aspect is vital in comprehending other solar phenomena, such as solar energetic particles and solar wind, and how they influence the near-Earth space environment.

A number of recent studies investigate the physical mechanisms responsible for the generation of solar type III radio bursts. For example, Chen et al. (2013) investigated the association of type III bursts with flaring activities in February 2011, via combined multi-wavelength observation from the Solar Dynamic Observatory (SDO) instruments, as well as Wind/WAVE and ground-based instruments. They found that the SDO measurements indicated that type III emission was correlated with a hot plasma (7 MK) at the extreme ultraviolet (EUV) jet's footpoint. By using a triangulation method with the Wind and the twin STEREO spacecraft, Bonnin et al. (2008) reported the first measurements of the beaming characteristics for two type III bursts between 2007-2008, assuming the source was located near the ecliptic plane (see also Reiner et al. (2009)). They concluded that the individual type III bursts have a broad beaming pattern that is roughly parallel to the Parker spiral magnetic field line at the source. Saint-Hilaire et al. (2012) conducted a study on almost 10,000 type III bursts observed by the Nançay Radioheliograph between 1998 and 2008. Their analysis revealed discrepancies in the location of type III sources that may have been caused by a tilted magnetic field. Additionally, they found that the average energy released during type III bursts throughout a solar cycle could be comparable to the energy produced by non-thermal bremsstrahlung mechanisms in nano-flares. Morosan & Gallagher (2017) utilized LOFAR data to investigate the statistical characteristics of over 800 type III radio bursts within an eight-hour period on July 9, 2013. They discovered that the drift rates of type III bursts were twice that of type S bursts and plasma emission was the primary emission mechanism for both types.

Pulupa et al. (2020) introduced a statistical overview of type III radio bursts during the first two PSP solar encounters. While the first encounter in November 2018 revealed a small number of bursts, the second encounter in April 2019 exhibited frequent type III bursts, including continuous occurrences during noise storms. They reported the characteristics of type III bursts with spectral and polarization analysis.

Krupar et al. (2020) performed a statistical survey of 30 type III radio bursts detected by PSP during the second encounter in April 2019 and estimated their decay times, which were used to estimate the relative electron density fluctuations in the solar wind. They localized radio sources using a polarization-based-radio triangulation technique, which placed the sources near the modeled Parker spiral rooted in the active region AR12738 behind the plane of the sky as seen from Earth.

Cattell et al. (2021) explored correlations between type III radio bursts and EUV emission in the solar corona. Using coordinated observations from PSP, SDO, and Nuclear Spectroscopic Telescope Array (NuSTAR) on April 12, 2019, they identified periodicities in EUV emission correlated with type III burst rates. The findings suggested impulsive events causing heating and cooling in the corona, possibly nano-flares, despite the absence of observable flares in X-ray and EUV data, which implies periodic non-thermal electron acceleration processes associated with small-scale impulsive events.

Harra et al. (2021) explored the origin of the type III radio bursts I am tackling in this paper and found that electron beams that triggered radio bursts may have emanated from the periphery of an active region that showed significant blue-shifted plasma. More recently, Badman et al. (2022) observed a distinct type III radio burst using the PSP and LOFAR between 0.1 and 80 MHz on April 9, 2019, around 12:40 UT, six days after the occurrence of the event analyzed in our study. While no detectable flare activity was linked with the event, a type III noise storm was ongoing during the PSP encounter 2. The authors determined the type III trajectory and reconstructed its source using observations from Wind and STEREO spacecraft, as well as measuring related electron enhancement *in situ*.

In the last few years, I have witnessed the emergence of modern instruments, such as LOFAR and PSP, that have allowed for the observation of solar radio emissions with higher sensitivity from a better vantage point. Although type III bursts have been extensively studied Dabrowski et al. (2021), there are still some unresolved issues regarding the exact mechanism of type III emissions. For example, it is not yet clear how the electrons are accelerated to the high energies required to generate type III radio bursts or what role the coronal magnetic field plays in this process. Furthermore, there are inconsistencies between the observations and the models, which need to be resolved in order to gain a more complete understanding of the dynamics of the solar corona. Examples of these inconsistencies are the origin of the type III radio bursts and the discrepancy between the estimated plasma densities from the models

and the observations. This paper aims to address these unresolved challenges by using new observations from LOFAR and PSP and models of the solar corona to study the physical mechanisms responsible for the generation of type III bursts. The data analysis includes a combination of radio spectroscopy and imaging techniques to study the frequency, temporal and spatial variations of the radio bursts.

This chapter is organized as follows. In Section 3.2, I describe the observations of type III radio bursts made with LOFAR and PSP. In Section 3.3 I explain the data analysis and modeling techniques used to study these events. In Section 3.4, I present the results of our analysis, including an investigation of the potential physical mechanisms responsible for the generation of type III radio bursts and a comparison of the observations with models of the solar corona. Finally, in Section 3.5, I summarize our findings and discuss their implications.

## 3.2 Observations

A number of studies focused on observing the solar radio emissions during the second encounter of the PSP in late 2019 Krupar et al. (2020); Pulupa et al. (2020); Cattell et al. (2021); Harra et al. (2021); Badman et al. (2022). In this study, our primary emphasis is directed towards investigating a set of type III radio bursts that took place on April 3, 2019, during the time interval spanning from  $\sim$ 12:10 to 12:50 UT. This period coincided with the presence of two distinct active regions (ARs) on the Sun, denoted as AR12737 and AR12738. AR12737 was situated on the Sun’s near side at coordinates E12°N06°. Notably, this region had eight sunspots and exhibited a  $\beta$  magnetic configuration according to the Hale magnetic classification Hale et al. (1919). On the other hand, AR12738 was positioned on the solar far side at coordinates E140°N02°. Due to its remote location, detailed observations of the magnetic configuration and activity within AR12738 were unattainable in this time frame.

I observed a group of intense type III radio bursts by four instruments (Wind/WAVES, PSP/FIELDS, STEREO-A/SWAVES, and LOFAR/LBA) via a regular survey. In Figure 3.1, I show the first type III burst within the time of this study as observed by the four instruments. By taking the second derivative of the light curve at a specific frequency channels, I determined the start time of the burst, which is denoted by the vertical red dashed line. The frequency bands used for obtaining the start time at each instrument are as follows: 6.97 MHz (Wind), 7.03 MHz (STEREO), 5.03 MHz (PSP), and 40.16 MHz (LOFAR).

I checked the relative orientations of the instruments with respect to Earth (Fig. 3.2). Since the PSP and STEREO spacecraft were almost aligned (close in an angular sense) with the Sun, the STEREO/EUVI image could be taken as what PSP would see (Fig. 3.3). Figure 3.3 shows how the solar disk looks like from the Earth perspective (using the SDO/AIA instrument) and from the eastern side where the PSP and STEREO were located at that time (using the STEREO/EUVI instrument). The right panel shows a closer view of AR12737 with the contours of the photospheric magnetic field obtained from the Helioseismic and Magnetic Imager (HMI) on board SDO. From the GOES-15/XRS and SDO/EVE instruments in the panels below, they also confirm that there is no flaring activity at that time.

The solar disk was quiet, including only one AR that is visible with no X-rays and no EUV transient emissions over this period. Nevertheless, the very sensitive LOFAR telescope detected a number of bursts close to noon. I checked PSP data, and I found bursts there as well. Meanwhile, from the EUVI and AIA images, I see that there are numerous small localized regions of relatively higher intensity (i.e., likely small-scale coronal brightenings spots or campfires; see Young et al. (2018); Madjarska (2019); Berghmans et al. (2021)). In the next subsections, I introduce the PSP and LOFAR instruments and their observations of the radio bursts.

### 3.2.1 PSP Observations

Parker Solar Probe (PSP) is a pioneering spacecraft with cutting-edge technologies, launched on August 12, 2018, aimed at helping to resolve key questions about solar corona and solar wind (Fox et al. 2016). To study the radio bursts, I used the level-2 data of the radio dynamic spectrum obtained from the FIELDS instrument suite (Bale et al. 2016; Pulupa et al. 2017), which can be downloaded from this website<sup>1</sup>. The data file is in CDF format and the unit of the data values is converted from  $V^2/Hz$  to  $dB$  units using the formula

$$I_{dB} = 10 \times \log_{10}(I/10^{-16}) \quad (3.1)$$

---

<sup>1</sup>PSP FIELDS data products: <http://research.ssl.berkeley.edu/data/psp/data/sci/fields/>

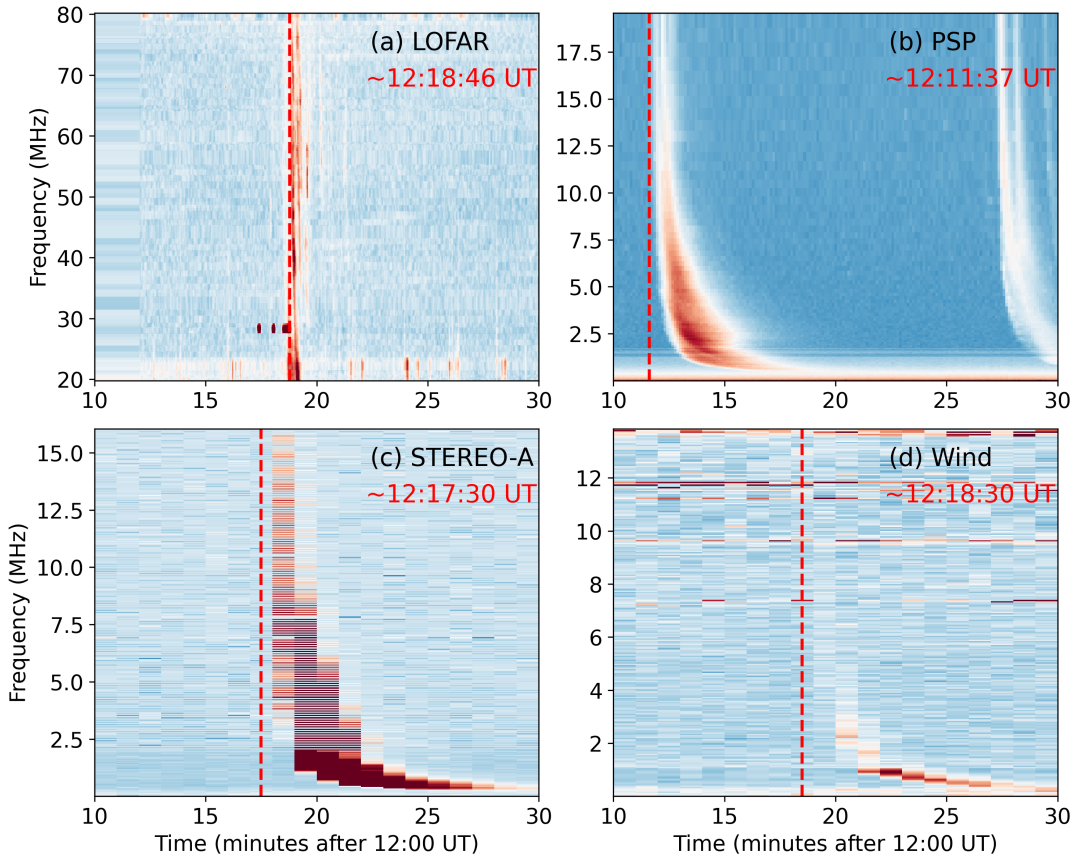


Figure 3.1: Radio dynamic spectra for a single burst obtained from multiple instruments. The top-left panel is from the LOFAR/LBA instrument, the top-right is from the PSP/FIELDS instrument, the bottom-left is from the STEREO/SWAVES instrument, and the bottom-right is from the Wind/WAVES. The vertical red dashed line denotes the start time of the burst.

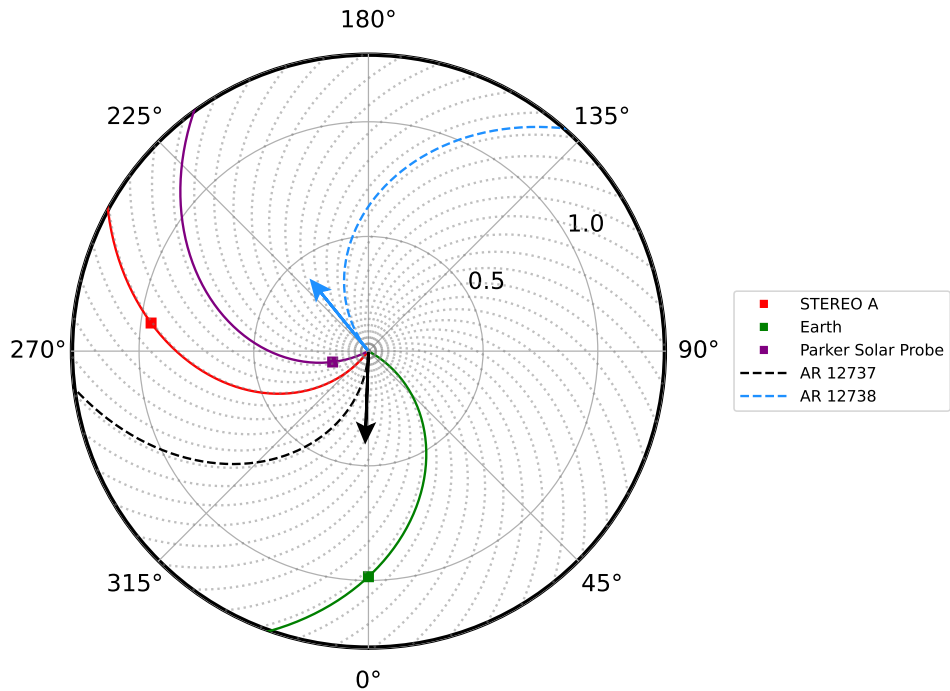


Figure 3.2: Top view of the spacecraft positions in the ecliptic plane at 12:15 UT on April 3, 2019, with the Sun-Earth line as the reference point for longitude. The Earth's location is representative of the positions of LOFAR, Wind/WAVES, and GOES-15/XRS instruments. The spacecraft were connected back to the Sun by a 400 km/s reference Parker Spiral. The black arrow represents the longitude of AR12737 and the blue arrow represents the longitude of the AR12738. The gray dotted lines are the background Parker spiral field lines. The black dashed spiral shows the field line connected to the AR12737, and the blue dashed spiral is connected to the AR12738. The figure is generated using the Solar MAgnetic Connection Haus (Solar-MACH) tool (Gieseler et al. 2023).

The minimum power spectral density (PSD) of  $10^{-16} V^2/Hz$  is used as a threshold for radio bursts according to Pulupa et al. (2020) for converting to decibels. Then, both the High-Frequency Receiver (HFR: 1.3 – 19.2 MHz) and the Low-Frequency Receive (LFR: 10.5 kHz – 1.7 MHz) data are combined into a single dynamic spectrum as shown in Figure 3.4 with a full frequency range between 10.5 kHz – 19.2 MHz. The mean intensity value at each timestep over the full frequency range is subtracted from each frequency channel to clean the spectrum and minimize the noise level.

### 3.2.2 LOFAR Observations

The Low Frequency ARray (LOFAR) radio telescope (van Haarlem et al. 2013) is a powerful tool for studying the Sun at low radio frequencies ranging between 10 and 240 MHz. Its high sensitivity and high time resolution have enabled the detection of various solar phenomena, including radio bursts and CMEs, and the study of dynamic processes in the solar atmosphere on timescales of milliseconds. The LOFAR dynamic spectrum from the beamformed radio observations is obtained by the Low-Band Antenna (LBA: 10 – 90 MHz) and can be downloaded from the LOFAR long-term archive (LTA)<sup>2</sup>. The High-Band Antenna (HBA: 110 – 190 MHz) data are not available for that timeframe. For this day under study, the LOFAR data are available between 11:42 – 13:27 UT. To clean the spectrum, background subtraction is performed, which flattens the sensitivity (response) with the frequency of the LBA antennas. Basically, the mean spectrum along each frequency band is calculated and subtracted from the whole frequency band, the same applied to the PSP spectrum. This operation effectively removes the constant background from the spectrum. Then a Gaussian smoothing filter is applied to the spectrum using the `scipy.ndimage.gaussian_filter` function with a sigma value of 1.5, which helps to reduce noise and variations in the data. After that, the PSP and LOFAR spectra are combined together in a single plot within the same time interval. The bursts' signals observed by the PSP occur earlier than those at LOFAR. This is due to the fact that the PSP spacecraft is much closer to the Sun and hence it detects the radio emissions earlier than LOFAR because of the shorter travel time of radio signals from the Sun. Therefore, the PSP dynamic spectrum must be shifted with respect to the LOFAR observations based on a calculation of the relative time travel of the radio emission from the Sun to PSP and to LOFAR. In addition, the time cadence of the PSP observations changes according to its distance from the Sun. On that day, the PSP data cadence was 7 seconds, while LOFAR's is 1 second. Therefore, the LOFAR dynamic spectrum was down-sampled to 7 seconds to match the time resolution of the PSP. Figure 3.4 shows the resulting combined LOFAR-PSP spectrum on a logarithmic y-axis. The LOFAR LBA frequency ranges between 19.82 – 80.16 MHz and for the PSP is 10.55 kHz – 19.17 MHz.

In order to detect the type III radio bursts automatically from the combined dynamic spectrum, I applied the Zhang et al. (2018) algorithm based on the probabilistic Hough transformation that detects vertical bright edges in images, within a certain degree of deviation from the vertical direction.

## 3.3 Methods

### 3.3.1 Imaging of radio sources

As part of our task, I developed an automated pipeline consisting of several modules that not only preprocessed and calibrated the LOFAR interferometric data to produce cleaned images of the Sun in the radio band (Zhang et al. 2022a), but also utilized the resulting data to find the trajectory of the radio sources and sample the magnetic field and plasma parameters at their respective locations through modeling and simulations in subsequent modules.

First, I ran the burst detection algorithm (Zhang et al. 2018)<sup>3</sup> on the combined dynamic radio spectrum of LOFAR and PSP (Fig. 3.4) to find the characteristics of each type III burst. I converted the spectrum into a binary map to isolate the bursts from the background. Then I applied the Hough transformation to get line segments of the features. For each type III burst, the line segments are grouped together into one group. To account for the interplanetary component within radio dynamic spectra, I employed the Parker electron-density model (Parker 1960) assuming a fundamental emission. This model enabled mapping between the time and frequency indices for each type III burst and subsequently converted electron densities into radial distances. Finally, a least-squares fitting method was applied to derive both the frequency drifts and the speed of the electron beams.

---

<sup>2</sup>LOFAR LTA: <https://lta.lofar.eu/>

<sup>3</sup>Detection algorithm repository: <https://github.com/peijin94/type3detect>

After this step, I did the same for the LOFAR dynamic spectrum only (Fig. 3.5) to find the  $(f, t)$  pairs for every type III burst. Then I took snapshot frequencies for each burst defined by a list of 60 central frequencies between  $\sim 20 - 80$  MHz from LOFAR LTA for the interferometric imaging. I obtained the interferometric data from LOFAR core and remote stations at the snapshot frequencies for all type III bursts. I used the concurrent observations of the radio source Tau-A to calibrate the interferometric observations. For that, I used the default preprocessing pipeline (van Diepen et al. 2018, DP3) for preliminary processing and calibrating the measurement sets (MS). Finally I obtained the cleaned images of the radio sources by using *w*-stacking clean (WSClean) algorithm (Offringa et al. 2014) only at the time indices in the MS files that are equivalent to the snapshot frequencies.

Table 3.1: Characteristics of the type III bursts detected via the automatic algorithm from the combined spectrum.

| Burst ID | Start Time (UT) | End Time (UT) | Start Frequency (MHz) | End Frequency (MHz) | Frequency Drift (MHz s <sup>-1</sup> ) | Beam Speed (c) |
|----------|-----------------|---------------|-----------------------|---------------------|--|----------------|
| 1        | 12:18:45        | 12:22:42      | 76.44                 | 1.57                | 0.892                                  | 0.044          |
| 2        | 12:34:05        | 12:36:31      | 41.24                 | 0.86                | 0.241                                  | 0.119          |
| 3        | 12:34:40        | 12:34:56      | 54.44                 | 26.54               | 3.992                                  | 0.046          |
| 4        | 12:37:14        | 12:38:09      | 66.03                 | 10.02               | 4.006                                  | 0.046          |
| 5        | 12:38:17        | 12:40:54      | 76.92                 | 1.57                | 0.77                                   | 0.066          |
| 6        | 12:39:34        | 12:40:11      | 78.86                 | 11.93               | 3.192                                  | 0.062          |
| 7        | 12:40:28        | 12:40:40      | 45.34                 | 22.9                | 3.21                                   | 0.067          |
| 8        | 12:41:39        | 12:43:06      | 78.21                 | 2.13                | 1.555                                  | 0.093          |
| 9        | 12:43:53        | 12:44:15      | 59.07                 | 42.13               | 2.424                                  | 0.013          |

After processing and cleaning the interferometric measurements of LOFAR, I explored the observations of each burst individually. Out of the 60 frequency bands in the LOFAR LTA, I chose 54 frequency bands that have unique integer numeric, between 19.92 - 80.08 MHz. For each burst, at each timestamp, the nearest frequency of the fit model to the list of chosen frequencies is picked as the snapshot frequency at that particular timestamp. This process was repeated for all the 16 type III bursts detected in the LOFAR dynamic spectrum in order to obtain snapshot images for each type III burst (Fig. 3.6). For each type III burst, I applied persistence imaging in order to create a continuous display of the radio emissions (Thompson & Young 2016).

Persistence imaging enables the creation of a clearer and more informative image. In the context of a time-ordered series of images, a method of persisting pixel values can be employed as follows: for each image, compare the value of each pixel to its corresponding value in the previous persistence image in the series. If the pixel value in the current image is brighter than its corresponding pixel in the previous image, replace the previous value with the current one; otherwise, retain the previous value. This process generates a new image, referred to as the current persistence image, which serves as the basis for the subsequent evaluation of the next image in the series. This evaluation involves a pixel-by-pixel comparison between the current image and its associated persistence image, allowing for the identification of any changes or patterns that may have occurred over time. The mathematical background is explained in Appendix A.1.1.

In order to estimate the locations of the type III sources in 3D space, I combined observations with modeling. I used magnetogram data from the Global Oscillation Network Group project (GONG) (Harvey et al. 1996). I constructed a grid of footpoints on the GONG map over two longitudinal belts around the two active regions AR12737 and AR12738, which are the two potential candidates source regions for the group of type III bursts under study. These points are used as the seed points for tracing the coronal magnetic field lines using pfsspy python package<sup>4</sup>, which is a robust implementation in python of the PFSS model developed by Stansby et al. (2020). Using the major and minor axes of the beam size, I estimated the radius of the radio source using Equation 3.2, which was used to approximate the source size. Since I already obtained the  $(x, y)$  positions of the type III sources in the plane of the sky (POS) through LOFAR observations, now it is necessary to determine their corresponding  $z$  position to have an overall understanding of their spatial distribution. Therefore, I employed Badman et al. (2022)'s approach here, assuming that the type III bursts were from harmonic emission. Firstly, I found the radial distance of the radio source from the Sun in the POS (Eq. 3.3). Secondly, I calculated the sources' radial distance ( $r_{model}$ ) using the  $2.5 \times$  Newkirk electron-density model (Newkirk 1961, 1967). The 2.5 fold factor is taken to incorporate the effects of scattering and overdensity (streamers) beyond

<sup>4</sup>Pfsspy tool: <https://pfsspy.readthedocs.io/>

the nominal Newkirk quiet Sun model. The MAS model results (Fig. 3.8) show streamers above the eastern limb, supporting the inclusion of such a factor. Lastly, I estimated the  $z$  location of the type III sources (Eq. 3.4). I proceeded with the  $+z$  solution because the theory precludes emission behind POS in this region of high-density gradients (i.e., the emission would be absorbed by passing through the high-density regions of the corona). More details are explained in Appendix A.1.2.

$$r_{source} = \sqrt{(b_{major}^2 + b_{minor}^2)}, \quad (3.2)$$

$$r_{pos} = \sqrt{(x^2 + y^2)}, \quad (3.3)$$

$$z = \sqrt{(r_{model}^2 - r_{pos}^2)}. \quad (3.4)$$

The result of the deprojection of the type III sources for the sixth burst are shown in Figure 3.7 with 70% contours made for ten frequencies on the extrapolated magnetic field lines. The red dashed line is a spline fitting curve that represents the trajectory of the centroids of the radio sources. The black arrow points toward the Earth's line of sight (LOS). It is worth to mention that the axes direction in the POS of LOFAR images are different in the 3D space. The  $(x, y)$  coordinates in the POS are translated into  $(y, z)$  in the 3D space, and  $z$  in the POS is translated into  $x$  in the 3D space.

### 3.3.2 Modeling

To explore the characteristics of the coronal plasma environment during the studied events, I used the Predictive Science Inc. (PSI) standard coronal solutions from magnetohydrodynamic (MHD) simulations originating from the MAS code (Mikić et al. 1999). The data are available on the PSI's data archive<sup>5</sup>. I obtained the PSI MAS coronal solution (a thermodynamic-with-heating MHD model) on April 3, 2019, at 12:00 UT, with the following simulation result ID<sup>6</sup>. Initially, I calculated the angle between the burst's source radial vector and the LOS. Moreover, I calculated the complement angle, which is the separation angle between the burst's radial vector and POS from the Earth's perspective. Subsequently, I utilized the complement angle to derive the Carrington longitude (Thompson, W. T. 2006), facilitating the extraction of a longitudinal segment from the MAS datacube, as if it were in the POS. Following this, the selected data slice was fed into the FORWARD model, a toolset responsible for generating synthetic coronal maps of observable quantities describing the plasma state. For extracting the longitudinal slices from the MAS data, I utilized the psipy python package<sup>7</sup>. The MAS datacube is specifically defined on a spherical grid and represents a steady-state MHD model. Owing to the inherent attributes of this datacube, the utilization of the FORWARD toolset proves more practical and advantageous for our objective. In Figure 3.8 I show the first radio contour of the sixth type III burst on top of the equivalent 2D maps for six plasma parameters, as an example. The plasma parameters are, from left to right and from the top to bottom: plasma density, plasma temperature, magnetic field strength, plasma beta parameter, the total plasma pressure, and the Alfvén speed. By taking the value of these physical plasma quantities at the centroids' coordinates of the type III sources at each frequency band, I obtained estimates of local plasma conditions shown in Figure 3.9 for the sixth type III burst, as an example.

## 3.4 Results and discussion

### 3.4.1 Detection and characterization of type III radio bursts

I found that the radio waves arrived at STEREO one minute before they arrived at Wind (Fig. 3.1). However, the difference between the  $+z$  and  $-z$  positions of the burst this close to the Sun in terms of light travel time is  $\sim 10$  seconds ( $\sim 4 R_\odot$ ), which is within the time resolution of the observations (1 min time resolution). Thus, I cannot confidently conclude whether the emission arrived at one spacecraft first and the other second.

Figure 3.4 shows the combined dynamic spectrum from both LOFAR and PSP. The free parameters of the auto-detection algorithm do not have the same values as for detection the type III bursts in the LOFAR spectrum alone. Upon visual examination, I observed that the detection algorithm effectively identified type III bursts in the LOFAR dynamic spectrum (Fig. 3.5), but it had limitations in terms of

<sup>5</sup>Predictive Science Inc.: <https://www.predsci.com/mhdweb/home.php>

<sup>6</sup>Simulation result ID: hmi\_med-cor-thermo2-std01\_med-hel-poly-std01

<sup>7</sup>PsiPy repository: <https://github.com/predsci/PsiPy>

detecting type III bursts in the combined spectrum of the LOFAR and PSP, as well as missing segments of the detected bursts and a few bursts entirely. This could be due to the increased frequency drift and dispersion of the radio bursts at lower frequencies, which made it a challenging task for the detection algorithm. I captured nine type III bursts from the combined dynamic spectrum and their characteristics are reported in Table 3.1. However, the detection algorithm performed better on the LOFAR dynamic spectrum only and I traced 16 type III bursts.

### 3.4.2 Imaging of radio emission sources

Figure 3.6 shows the persistence imaging for the 16 type III bursts in the LOFAR dynamic spectrum (Fig. 3.5). The observation frequencies and timestamps of the snapshot images used to produce the persistence image are shown at the top-right corner of each image. From a visual inspection of Figure 3.6, it seems that all the type III emissions originated from the same quadrant in the images (south-east direction on the solar disk), although there was no active region presented at that location except for a single active region nearby the central meridian (Fig. 3.3). Based on the imaging data presented in Figure 3.6, I chose one representative type III burst (No. 6) for a single-burst analysis in this paper, as it shares similarities in extent and location with other bursts.

To determine the spatial connection between the sources of radio emissions and the coronal magnetic field, a three-dimensional (3D) projection of the radio source contours onto the extrapolated coronal magnetic field via the PFSS model was employed (Fig. 3.7). The result indicates a discernible south-eastward propagation of the radio sources relative to the Earth's perspective, with no open field line crossing the radio sources. In Figure 3.7, I performed an extrapolation only over the two active regions presented on the solar surface at that time. However, when I extrapolated the magnetic field over the entire solar surface, I noticed that the radio sources are aligned with the lower part of large-scale closed field lines and are placed onto the open field lines emanating from the southern coronal hole. No open field lines crossing the radio sources are observed. I note that the PFSS modeling is limited by the fact that AR12738 is behind the limb on April 3 as observed from Earth. Consequently, the magnetic data available to us could be around two weeks old or more. This might limit the reliability of PFSS extrapolation for that region during that specific timeframe.

From Figure 3.7, the results suggest several potential origins of these type III radio emissions: 1) they could be triggered in a closed-field lines structure such as large-scale coronal loops, given that the radio sources are aligned to closed-field lines geometry in the southern hemisphere; 2) they could be triggered by electron beams that are accelerated from an open-field active region (Kong et al. 2018). However, from the PFSS model, I found no evidence for magnetic connectivity from both ARs on the Sun at that time; 3) they may result from electron beams that are accelerated in the corona due to expanding magnetic fields from plasma upflows in the active region (Del Zanna et al. 2011; Harra et al. 2021). Our findings indicate a notable inverse relationship between imaging quality and the level of solar radio emission brightness (e.g., for type III bursts 10 and 13, for instance). This observation is due to the leakage of solar radio emission into the side lobes of the calibrator beam, which disrupts the accuracy of calibration solutions.

### 3.4.3 Plasma diagnostics and magnetic field analysis

Considering the observed alignment of radio sources in Figure 3.7 and the case depicted in Figure 3.8, it becomes evident that radio sources at higher frequencies (indicating proximity to the Sun) align with a streamer-like structure near the equator within the coronal model. This structure is characterized by elevated plasma beta, reduced coronal temperature, and diminished Alfvén speed. The coronal plasma density was relatively homogeneous with no prominent structures, probably due to the model resolution.

The location of radio sources of all the bursts were in the same quadrant as seen from Earth. Therefore, I assumed that the former description applies for all bursts. I also found that the radio sources were confined between the equatorial sheet and the southern coronal hole and moving along that boundary. Figure 3.9 shows the variability of the coronal plasma quantities at the radio sources' centroids, taken from FORWARD maps in Figures 3.8, at different frequencies for the sixth burst. To estimate the error bars, I initialized random centroids, within the limits of the 70%-contours of the radio emissions, to sample the plasma quantities at those locations. Then the standard error (SE) is calculated using Equation 3.5, where  $\sigma$  is the standard deviation, and  $n$  is the number of points.

$$SE = \frac{\sigma}{\sqrt{n}} \quad (3.5)$$

The coronal temperature was increasing with radial distance, which implies there may have been some heating locally. The behavior of the coronal magnetic field, the plasma total dynamic pressure, and the Alfvén speed were decreasing over distance as expected. Finally the value of plasma beta parameter started increasing sharply around 40 MHz, which implies that the plasma pressure became more dominant than the magnetic pressure around that distance from the Sun (for a  $2.5 \times$  Newkirk model, it is  $1.89 R_\odot$  assuming a fundamental emission, or  $2.57 R_\odot$  assuming a harmonic emission).

The top-left panel of Figure 3.9 shows a comparison between the density profiles of the MAS model, the  $2.5 \times$  Newkirk model and the theoretical expected density profiles under the fundamental and harmonic assumptions. Although the Newkirk density model provided a useful approximation for determining the height of radio sources in the corona, it is not entirely accurate due to a number of its underlying assumptions; for instance, the assumption of a steady state and the spherical symmetry of the corona, which do not always apply. Therefore, I tried to use the MAS density values to estimate the depth along the LOS of the radio source, since it is supposed to give a more realistic result. I found that the plasma density obtained from the MAS and FORWARD modeling results were significantly lower compared with the  $2.5 \times$  Newkirk density model and the theoretical expected density obtained from the classical relation in Equation 3.6, where  $f_p$  is the plasma frequency (in MHz) and  $n_e$  is the electron density (in  $\text{cm}^{-3}$ ):

$$n_e = \left( \frac{f_p}{8.98 \times 10^{-3}} \right)^2 \quad (3.6)$$

The required density from the fitted Newkirk model is much higher (about ten times) than what is obtained from the MAS model, even after accounting for the  $2.5 \times$  enhancement already applied to the standard Newkirk model. This implies the discrepancy cannot be fully explained by the density enhancement factor alone. Furthermore, the imaging places the radio sources near a streamer which is an overdense region in the MAS model, so it seems unlikely the source's apparent location in the model is wrongly attached to a less dense feature, as there are not denser options available. The apparent source positions from the imaging are likely too high, possibly due to scattering effects (Kontar et al. 2019, 2023; Chen et al. 2023), which could lead to fitting an overly dense Newkirk model. Another potential explanation is that there could be a stealth CME that pushed the coronal magnetic field outward, allowing the plasma to follow it to be perceived as having a higher density than expected, and there was not enough time for the magnetic field relaxation to occur (private communication with J. Magdalenić). However, scattering alone does not seem to fully explain the large density discrepancy. While further investigation is certainly needed regarding scattering and propagation effects on the radio waves, it is interesting to report this significant discrepancy between the model and observations, as it highlights limitations in the current modeling and suggests the need for additional physics to properly characterize the density distribution. Resolving this discrepancy could lead to important insights into the true nature of the corona.

### 3.5 Summary and conclusions

In this work I analyse the characteristics of a series of type III bursts that occurred on April 3, 2019, during the second near-Sun encounter period of PSP. The bursts were observed in dynamic spectra taken with the PSP/FIELDS (2.6 kHz – 19 MHz) instrument, as well as in interferometric imaging with the LOFAR (20 – 80 MHz) ground-based telescope, as part of a coordinated observing campaign. The series of 16 separate weak bursts were observed over the span of  $\sim 20$  minutes, during an otherwise relatively quiet period. The solar disk as observed from Earth was dominated by a single active region near its center. I combined the dynamic spectra for the LOFAR frequency range and the PSP frequency range to study the solar radio emissions within the frequency range of 2.6 kHz – 80 MHz.

For the study, I developed a semi-automated pipeline, which allowed us to obtain the exact times and frequencies of the bursts. These I used to align the PSP to the LOFAR observations and to generate interferometric images between 20 and 80 MHz. I performed data pre-processing of the PSP and LOFAR dynamic spectra to resample and shift the data based on the relative location of the spacecraft with respect to the Sun and Earth, and found an excellent temporal match between the two sets of observations. Thus I automatically traced the type III bursts in the dynamic spectra algorithmically and estimated frequency drift and the electron beam speeds. I found that frequency drifts remained relatively uniform between the high-frequency (LOFAR) and low-frequency (PSP) observations, as well as among the bursts, suggesting that they are related.

In addition, I imaged the type III emission at multiple frequency bands using the interferometric observations from LOFAR to determine the locations of the sources in the solar corona. The type III emissions observed were all found to occur in the same general region off the southeast limb of the Sun, leading us to conclude that they shared a single source of electron beams low in the corona. The potential origins of these emissions are varied and include: 1) small-scale impulsive events such as nanoflares (ish 2017; Che 2018; Chhabra et al. 2021); 2) plasma upflows from the active region (Harra et al. 2021); 3) coronal closed-loop structures (Wu et al. 2002); 4) electron beams accelerated from interchange reconnection (Gopalswamy et al. 2022); 5) high-frequency Alfvén waves and/or magnetic reconnection in the outer corona (Morton et al. 2015; Alielden & Taroyan 2022).

Our magnetic extrapolation shows that there is no open potential field to either AR12737 or AR12738, which is consistent with Cattell et al. (2021). Our findings are in line with the conclusions of Harra et al. (2021), who proposed that the likely origin of these type III bursts is the AR12737 region. The type III radio bursts in Harra et al. (2021) occurred between April 1 and 4, are temporally aligned with the emergence of AR12737 near the eastern limb of the solar disk.

While potential field source surface models provide valuable insight into the large-scale magnetic topology, their reliability decreases near active regions where the field can deviate significantly from a potential configuration. Therefore, the lack of open field connectivity directly to AR12737 suggested by the PFSS model should be viewed with some caution.

This work (Nedal et al. 2023) complements those results by precisely locating the burst sources in the middle of the corona. I used the Newkirk density model to estimate the height of the radio sources from the Sun of one of the type III bursts as representative of all. Combining this with PFSS magnetic modeling, I found good agreement between the centroids of the radio sources and the location of the southern open field lines in the corona, which would be required to produce radio emissions at interplanetary wavelengths in general. On the other hand, this location does not seem to be well connected to the AR itself, according to the PFSS model.

I attempted to correct the radial distance of the radio sources from the Sun by replacing the Newkirk model with more realistic MHD results from the MAS model, but I found that there is a significant discrepancy between the Newkirk model profile fitted to the observations and the MAS density. This could result from scattering lensing the apparent burst location to a higher altitude, thus, overestimating the height of radio sources in the corona. The presence of type III radio sources at relatively high distances in the corona, with plasma density higher than expected from the MAS model, suggests that there may be missing information in the modeling. One possibility is the existence of a stealth CME that pushed the coronal magnetic field outward, causing the plasma to appear denser than expected (see Dumbović et al. (2021)) — or other non-obvious changes in large-scale coronal magnetic topology. These findings demonstrate that scattering and propagation effects play a significant role in determining the location and directionality of solar radio bursts (Kontar et al. 2019, 2023; Chen et al. 2023). Therefore, the discrepancy between the observed and modeled density profiles could potentially be attributed to scattering and lensing effects that make the radio sources appear higher in the corona than their true location. Further investigation is required to disentangle these effects from limitations in the density models themselves. Overall, accounting for scattering and refraction will likely lead to improved modeling of the corona and solar radio bursts. In future work, I will also employ the time delay of arrival (TDoA) technique (Zhang et al. 2019) to estimate the radio burst source positions from multi-instrument observations and compare that with the current methodology in this paper. Solar Orbiter observations shall also be included.

High-fidelity interferometric radio imaging in metric-decametric wavelengths provides a powerful method to characterize solar eruptive events. It is also becoming increasingly important for studying relatively quiet periods, during which there may be elevated levels of in situ particle fluxes. The ability to observe and image faint radio bursts such as those presented in this work, which may be related to episodes of reconnection on the solar surface, and potentially to episodes of solar wind release, is a testament to LOFAR’s power as a space weather instrument. In a future work, I will automate and use our method for studying hundreds of faint bursts observed with LOFAR and will investigate their relation to small-scale activity on the solar surface.

Through a novel combination between the LOFAR imaging and MAS model results, I found that the type III radio bursts experienced a weakening background magnetic field, decreasing solar wind dynamic pressure and Alfvén speed, increasing plasma beta and coronal temperature, and plasma rarefaction. The radio sources appeared at larger radial distances than the models predicted, which suggests scattering and density fluctuations are important when attempting to interpret the actual burst trajectory. The discrepancies between the observed and modeled radial distances of the radio sources suggest refinements are needed in the models to fully explain the radio imaging and modeling results. Overall, comparing the

LOFAR imaging and MAS modeling for these type III bursts motivates further analysis on additional radio bursts to improve our understanding of the physical conditions that influence the propagation of radio emissions in the corona.

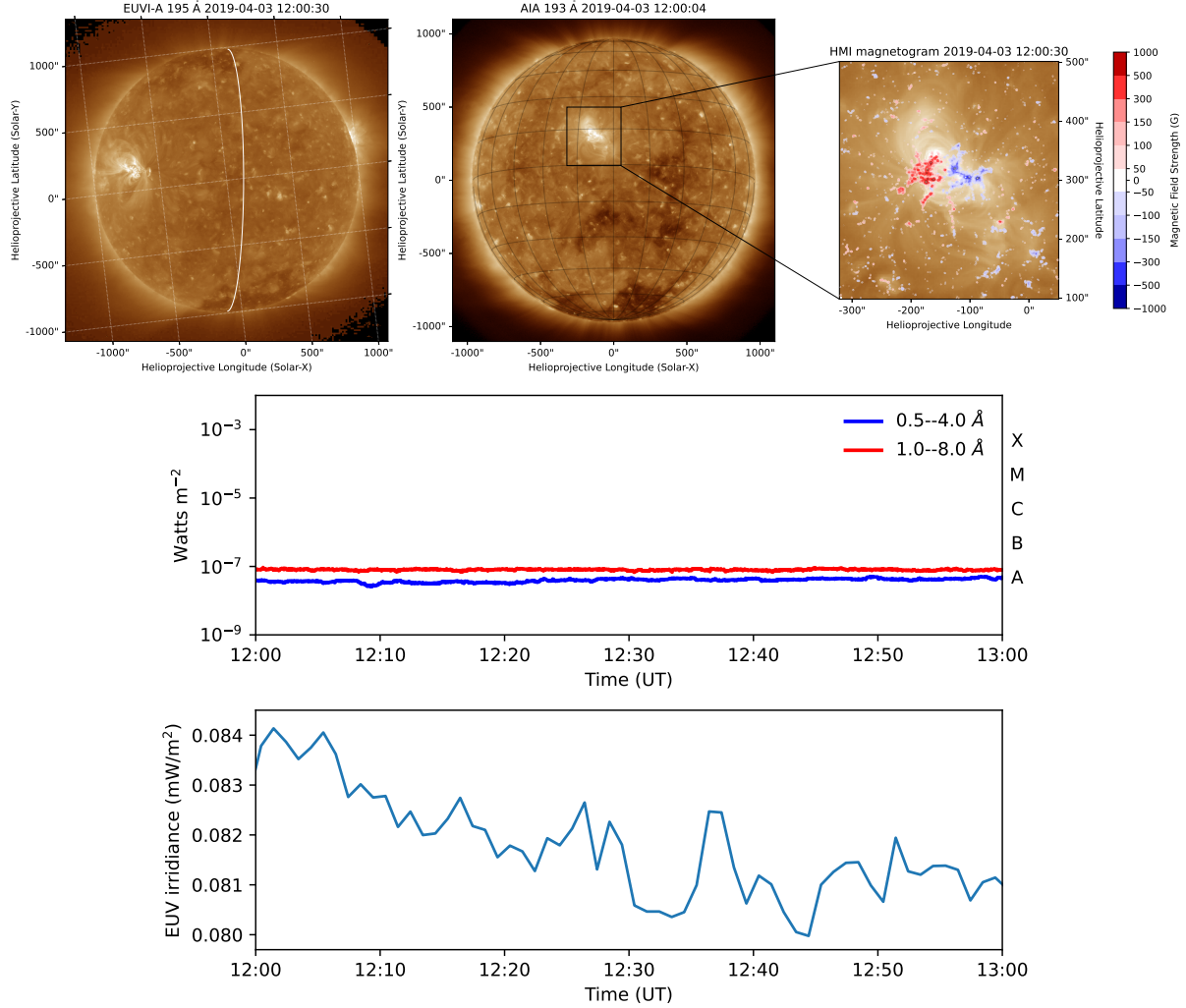


Figure 3.3: Exploring the X-ray and extreme ultraviolet (EUV) emissions from the Sun. The top panel showcases a cutout region of the SDO/AIA 193 Å image of the solar disk along with the STEREO-A EUVI 195 Å point of view. The white curve is the limb of the solar disk as seen by AIA from the right side. The red and blue colors are the contours of the line-of-sight magnetogram from the SDO/HMI instrument. The levels are (50, 100, 150, 300, 500, 1000) Gauss. The middle panel shows the X-ray flux from the GOES-14 spacecraft shows minimum activity. The bottom panel shows the time series of the ESP Quad band from the SDO/EVE instrument, which shows the solar irradiance in the extreme ultraviolet (EUV) band.

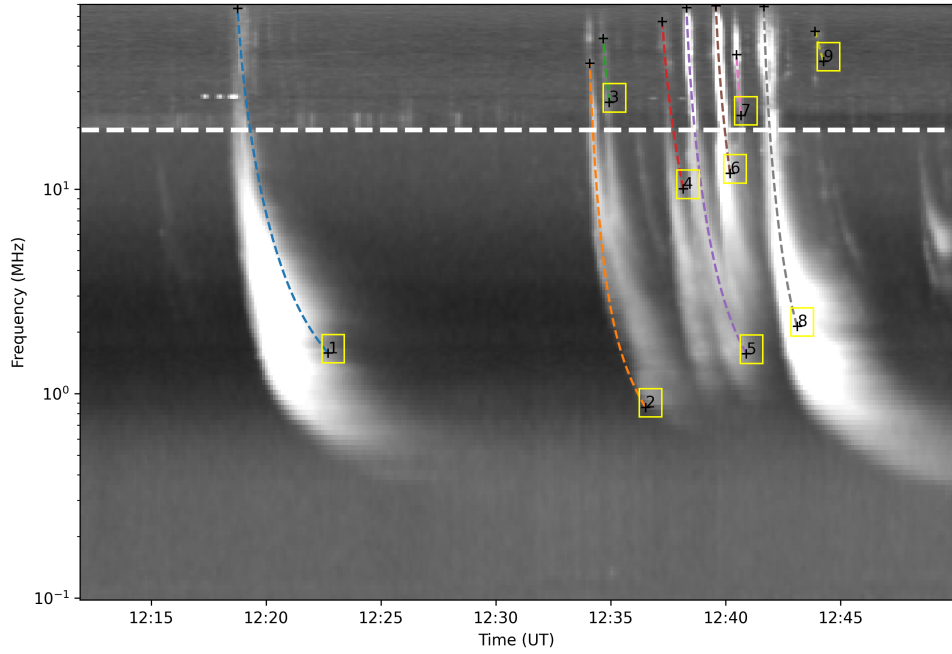


Figure 3.4: Automatic detection of type III radio bursts from the combined radio dynamic spectrum of LOFAR and PSP instruments. The dashed horizontal lines separates the LOFAR frequency range (top) and the PSP frequency range (bottom).

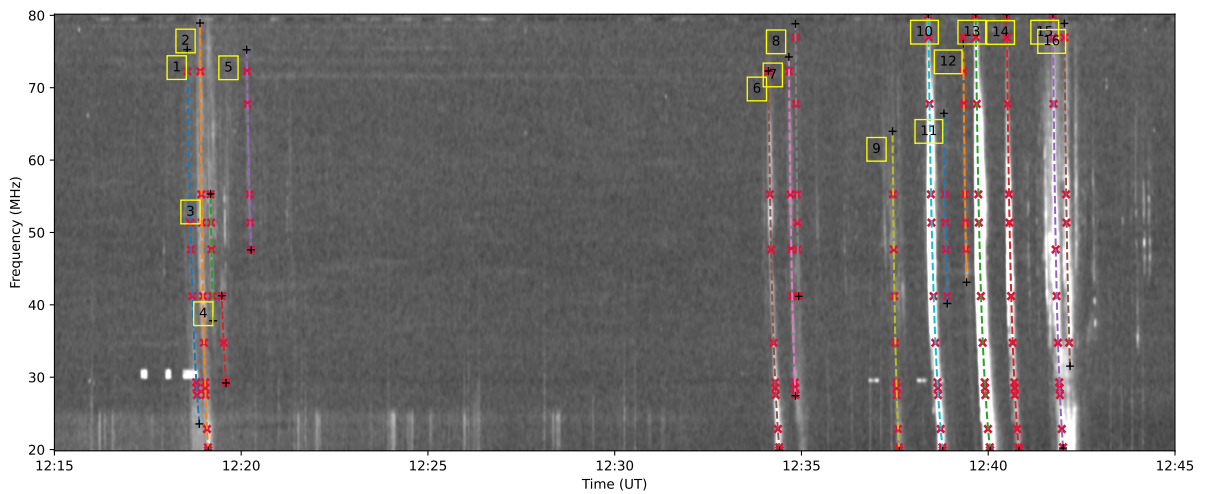


Figure 3.5: Automatic detection of type III bursts observed by LOFAR. The red symbols along the fit lines are the  $(f, t)$  coordinates of the image snapshots shown in Figure 3.6.

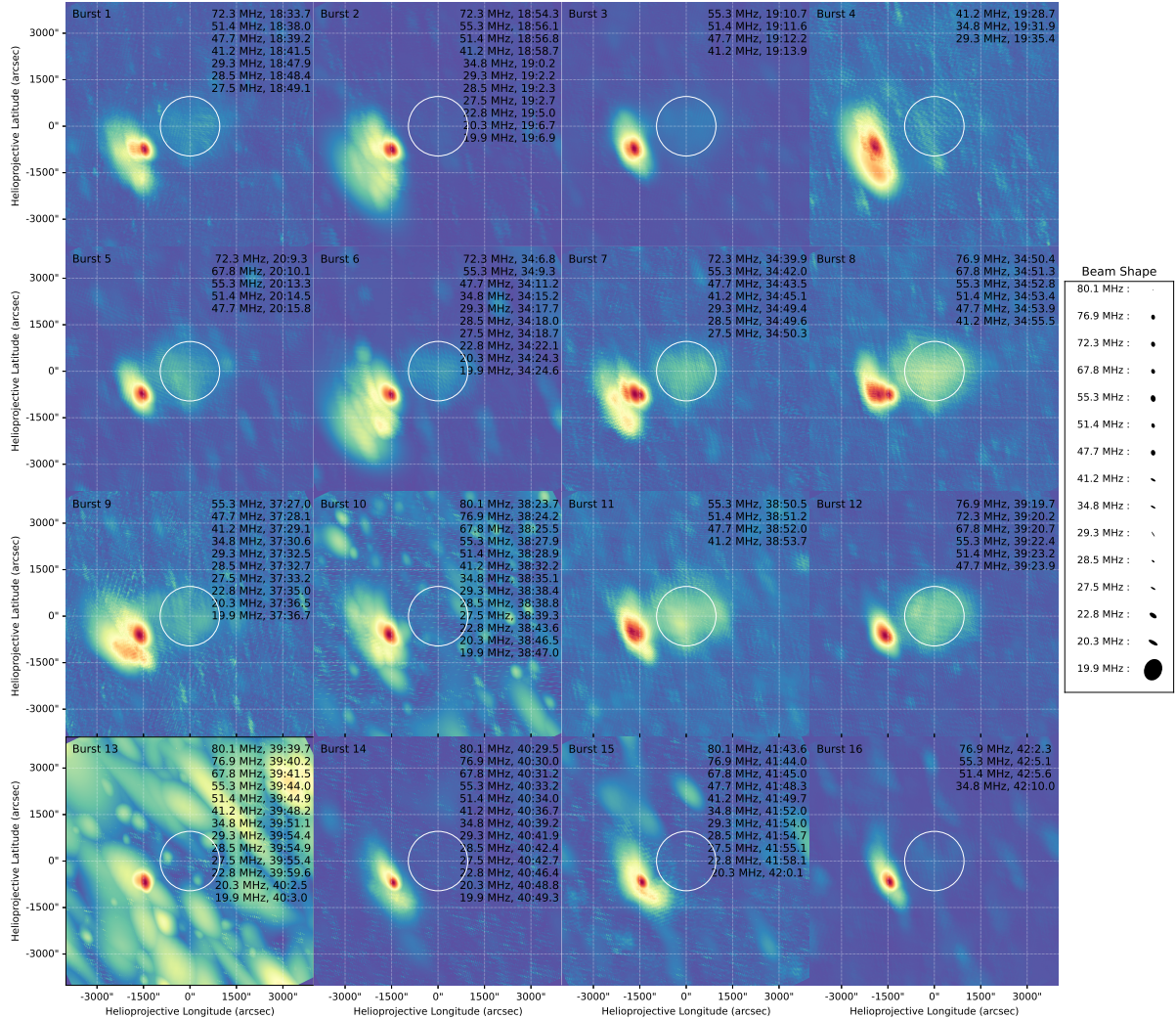


Figure 3.6: Persistence imaging for the 16 type III bursts detected in the LOFAR dynamic spectrum. The label shows the observation frequencies in MHz and times in (minutes:seconds from 12:00:00 UT). Here, the color coding is not absolute, but rather each panel has its own color code.

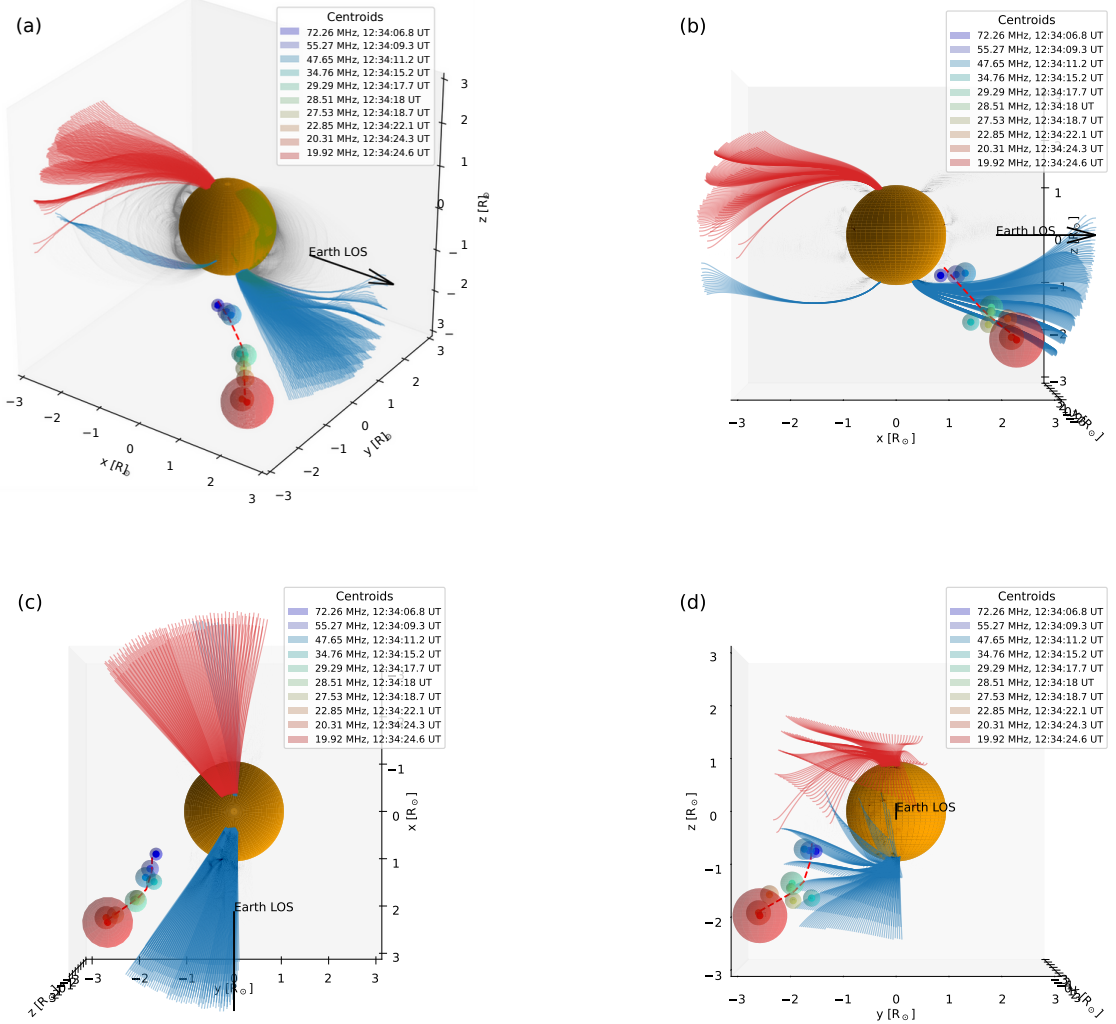


Figure 3.7: Different viewing angles for the deprojection of the radio sources of the sixth burst using the  $2.5 \times$  Newkirk electron-density model on the PFSS solution. The black arrow points toward the Earth's LOS. The  $yz$  plane is the POS as seen from the Earth. The red dashed line is a spline curve fit for the sources' centroids. The red, black, and blue curves are the open northern, closed, and open southern field lines, respectively. The opacity of the closed field lines is decreased for better visualization.

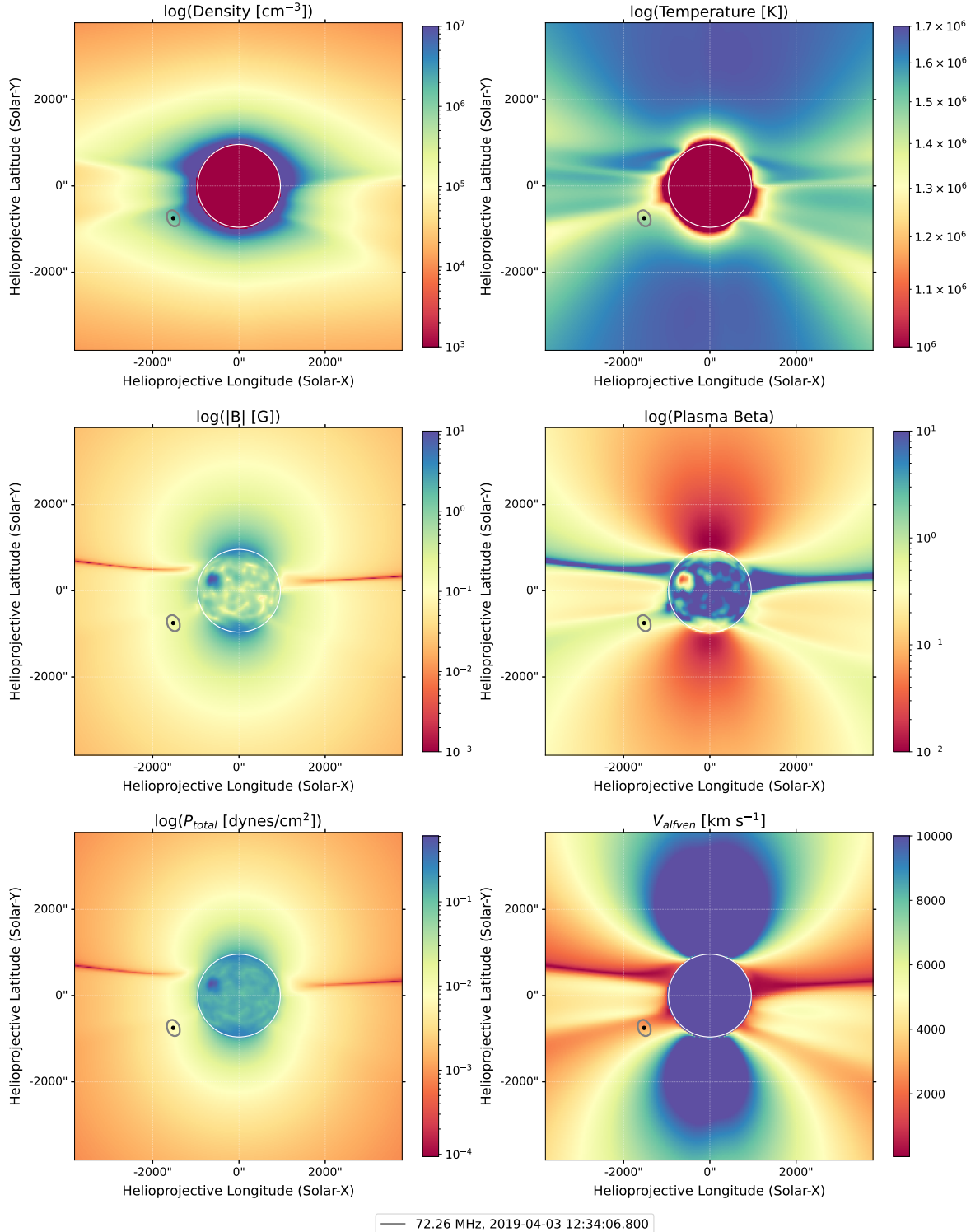


Figure 3.8: Synthesized maps of plasma parameters obtained using the FORWARD toolset, with the 70%-contour of radio emission of the sixth burst at the first timestamp (12:34:06.8 UT) at the frequency of 72.26 MHz depicted on top of the 2D POS cuts. The left column represents, from top to bottom, plasma density, magnetic field, and the total plasma dynamic pressure. The right column represents, from top to bottom, the temperature, plasma beta, and the Alfvén speed.

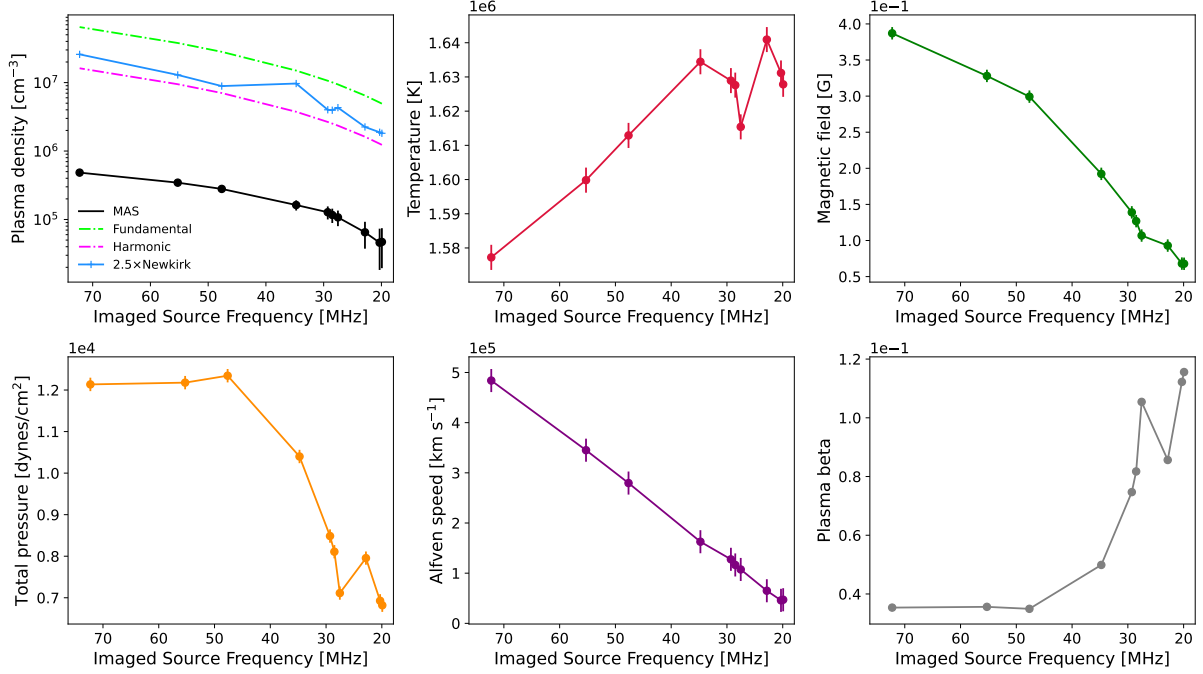


Figure 3.9: Coronal plasma parameters sampled from the 2D maps by the source centroids. The top panel shows (from left to right) the plasma density profiles from the MAS model,  $2.5 \times$  Newkirk model, and the theoretical densities under the fundamental and harmonic assumptions, plasma temperature, and magnetic field. The bottom panel shows, from left to right, the total plasma dynamic pressure, Alfvén speed, and plasma beta. The x-axis is inverted to demonstrate a progression of increasing radial distance from the Sun as the observer moves towards the right.

## Chapter 4

# Modeling and Forecasting of Solar Energetic Protons (SEP)

This chapter has two parts. In the first part, I describe a modeling study that we conducted on energetic proton acceleration and propagation from the solar corona to 1 AU. For this modeling, we employ the physics-based approach utilized in the first chapter, including the 3D coronal models and a 3D MAS-MHD model run. With these models, we use the EPREM model to find the fluxes and spectra of energetic protons at 1 AU. We then compare the modeling results with in-situ measurements. In the second part, I describe a deep learning approach that I developed to forecast the integral flux of energetic protons in three energy channels across three different forecasting horizons.

### 4.1 Introduction

Coronal Mass Ejections (CME) are a major source of accelerated solar energetic particles (SEPs), exceeding the thermal plasma in ions and electrons (Reames 1999). While flares contribute SEPs, CME-driven shocks play a key role through compression and acceleration above 100 MeV/nucleon, even in early stages below  $10 R_{\odot}$  (Ontiveros & Vourlidas 2009; Gopalswamy & Yashiro 2011). Consequently, research has focused on CME and shock dynamics in the corona using multi-wavelength observations. Recent studies of CMEs have utilized Extreme Ultra-Violet (EUV) and radio wavelength observations to uncover nuances beyond the prominence of these solar eruptions in visible light (Vourlidas et al. 2003; Zhang & Dere 2006; Bein et al. 2011). Observation of the solar corona in EUV wavelengths allows the initiation of CMEs to be imaged, through the use of instrumentation such as that on the Solar Dynamics Observatory (Lemen et al. 2012; Pesnell et al. 2012, SDO). CME propagation can generate shock waves visible as EUV waves or bright fronts in the corona (Thompson et al. 1998; Long et al. 2011).

Extending prior work, Kozarev et al. (2022) explored early SEP production using coronal bright front (CBF) events and a model of Diffusive Shock Acceleration (DSA) of Kozarev & Schwadron (2016). This revealed event-to-event variations and temporal evolution in acceleration efficiency strongly influenced by diverse coronal environments through which shock waves propagate. This approach demonstrates the use of computationally complex physics-based models to predict SEP flux at multiple energies.

Several models are available, or under development, for forecasting SEP, which use diverse approaches and serve different objectives. These models comprise computationally complex physics-based models, quick and simple empirical models, Machine Learning (ML)-based models, and hybrid models that combine different approaches and produce different types of outputs, including deterministic, probabilistic, categorical, and binary. Deterministic models always generate the same output without any randomness or stochastic components, such as predicting the SEP flux at a specific moment or the arrival time of SEP. On the other hand, probabilistic models provide a probability value that reflects the likelihood of an SEP event occurring. However, replicating SEP fluxes at a specific time is still a significant challenge for current models.

An excellent review on SEP models and predictive efforts was recently published by Whitman et al. (2023), which summarizes the majority of the existing models. For instance, Papaioannou et al. (2022) introduced the Probabilistic Solar Particle Event Forecasting (PROSPER) model, which is incorporated into the Advanced Solar Particle Event Casting System (ASPECS)<sup>1</sup>. The PROSPER model utilizes a

---

<sup>1</sup> ASPECS: <http://phobos-srv.space.noa.gr/>

Bayesian approach and data-driven methodology to probabilistically predict SEP events for 3 integral energy channels  $>10$ ,  $>30$ , and  $>100$  MeV. The model's validation results indicate that the solar flare and CME modules have hit rates of 90% and 100%, respectively, while the combined flare and CME module has a hit rate of 100%. Bruno & Richardson (2021) developed an empirical model to predict the peak intensity and spectra of SEP at 1 AU between 10 and 130 MeV, using data from multiple spacecraft. The model is tested on 20 SEP events and shows good agreement with observed values. The spatial distribution of SEP intensities was reconstructed successfully, and they found a correlation between SEP intensities and CME speed.

Hu et al. (2017) extended the Particle Acceleration and Transport in the Heliosphere (PATH) model to study particle acceleration and transport at CME-driven shocks. They showed that the model can be used to obtain simultaneous calculations of SEP characteristics such as time-intensity profiles, instantaneous particle spectra, and particle pitch angle distributions at multiple heliospheric locations. Overall, results resemble closely those observed in situ near the Earth but also yield results at other places of interest, such as Mars, making it of particular interest to Mars missions. SPREAdFAST (Kozarev et al. 2017, 2022) is a physics-based, data-driven framework that utilizes EUV observations and models to simulate SEP fluxes at 1 AU and to estimate energetic particle acceleration and transport to various locations in the inner heliosphere. It generates time-dependent histograms and movies distributing them through an online catalog. The accuracy and efficiency of the model were encouraging, but the highest energy fluxes showed disagreement with in situ observations by the SOHO/ERNE instrument. However, the framework has great potential for space weather science and forecasting.

In Aminalragia-Giamini et al. (2021), they used neural networks to provide probabilities for the occurrence of SEP based on soft X-rays data from 1988 to 2013. They obtained  $>85\%$  for correct SEP occurrence predictions and  $>92\%$  for correct no-SEP predictions. Lavasa et al. (2021) described a consistent approach to making a binary prediction of SEP events using ML and conventional statistical techniques. The study evaluated various ML models and concluded that random forests could be the best approach for an optimal sample comprising both flares and CMEs. The most important features for identifying SEP were found to be the CME speed, width, and flare soft X-ray fluence. Kasapis et al. (2022) employed ML techniques to anticipate the occurrence of a SEP event in an active region that generates flares. They utilized the Space-Weather MDI Active Region Patches (SMARP) dataset, which comprises observations of solar magnetograms between June 1996 and August 2010. The SMARP dataset had a success rate of 72% in accurately predicting whether an active region that produces a flare would result in a SEP event. Moreover, it provided a competitive lead time of 55.3 min in forecasting SEP events.

Engell et al. (2017) introduced the Space Radiation Intelligence System (SPRINTS), a technology that uses pre- and post-event data to forecast solar-driven events such as SEP. It integrates automatic detections and ML to produce forecasts. Results show that SPRINTS can predict SEP with an 56% probability of detection and 34% false alarm rate. Nevertheless, the HESPERIA REleASE tools provide real-time predictions of the proton flux at L1 by using near-relativistic electrons as a warning for the later arrival of protons and have been set to operation (Malandraki & Crosby 2018). Historical data analysis indicates high prediction accuracy, with a low false alarm rate of approximately 30% and a high probability of detection of 63% (Malandraki & Crosby 2018).

Forecasting SEP is a critical task that serves operational needs and provides insight into the broader field of space weather science and heliophysics. As emphasized in previous works, a high precision forecasting model is urgently required to predict SEP flux within a period of time, given the risks associated with these events. This highlights the critical requirement for a dependable forecasting system that can mitigate the risks associated with SEP.

Scientists have been using physics-based and empirical models for decades to forecast SEP. However, these models have certain limitations. Physics-based models require accurate input data and underlying physical assumptions. In addition, the complexity of the physics involved and incorrect parameters may introduce uncertainties that can lead to inaccurate predictions. On the other hand, empirical models rely on historical data to make predictions. While they can be accurate sometimes, they may be unable to account for changes in physical conditions related to the acceleration and propagation of SEP, which can influence prediction accuracy. ML models, however, provide a different approach to SEP forecasting. These models can analyze vast amounts of data, learning patterns from the data that are used, and connections that may not be obvious to experts. Additionally, ML models can adapt to changes in underlying physical conditions, resulting in more accurate predictions as more data is collected; they also provide relatively rapid forecasts, which allows for incorporation into a real-time forecasting workflow.

In the upcoming sections, I will explore the limitations in accuracy that arise from dealing with an

imbalanced dataset and low-resolution data. Specifically, the presence of intrinsic outliers in the time series data pertaining to SEP flux poses a significant challenge in modeling. These outliers correspond to occurrences of SEP events and, consequently, have an impact on the accuracy of predictions. Notably, they often lead to an underestimation of the SEP fluxes, primarily due to the predominance of relatively low values throughout the majority of the time interval.

In the first part, we extend the work in Chapter 2 on the kinematics of CBFs and expand on previous relevant investigations by modeling CBF-related shocks and particle acceleration up to 10 solar radii. Our modeling approach incorporates coupling to a numerical model of particle transport throughout the heliosphere, with validation against in-situ spacecraft measurements. Our study implements, for the first time, an extensive physics-based model linking CME-driven shock acceleration with the propagation of SEPs from the Sun to Earth. In the second part, I present advanced deep learning models to forecast the daily integral flux of SEP over a 3-day forecasting window by using bi-directional long short-term memory (BiLSTM) neural networks, for 3 energy channels ( $>10$ ,  $>30$ , and  $>60$  MeV). Our models can forecast the time-dependent development of SEP events in different energy domains, which can be used to model the space radiation profiles using frameworks such as BRYNTRN Wilson et al. (1988) and GEANT4 (Truscott et al. 2000).

## 4.2 Early-Stage SEP Acceleration by CME-Driven Shocks

### 4.2.1 Overview

The purpose of the SPREAdFAST (Solar Particle Radiation Environment Analysis and Forecasting-Acceleration and Scattering Transport) project is to model and analyze the particle fluxes from the Sun to Earth, specifically focusing on solar energetic particle (SEP) events. The project combines detailed observations of coronal bright fronts (CBFs) with modeling of the coronal plasma and the resulting SEP production and interplanetary transport. The SPREAdFAST framework utilizes physics-based modeling to simulate the evolution of the plasma upstream of the coronal shock associated with CBFs and the subsequent acceleration and transport of protons from the Sun to 1 AU. It incorporates various components such as EUV observations, shock dynamics, particle acceleration, and interplanetary transport. The project aims to provide a better understanding of the processes involved in SEP events and improve forecasting capabilities for these events. By modeling a large number of events and comparing the model results with in situ observations, the SPREAdFAST project contributes to the advancement of Sun-to-Earth physics-based modeling of SEP acceleration and transport. Overall, the SPREAdFAST project is a comprehensive effort to study and simulate the complex phenomena associated with SEP events, with the goal of enhancing our knowledge and predictive capabilities in this field.

The SPREAdFAST framework includes the following components:

1. CBF Kinematics and Geometric Modeling: This component characterizes the kinematics of Coronal Bright Fronts (CBFs) using observations from the Atmospheric Imaging Assembly (AIA) instrument. It estimates the CBF kinematics, including the front, peak, and back edge positions over time, as well as the mean intensity and thickness of the CBFs.
2. Coronal Shock and Particle Acceleration Modeling: This component models the evolution of the plasma immediately upstream of the coronal shock associated with CBFs. It incorporates the physics of coronal shock waves and the process of particle acceleration through diffusive shock acceleration.
3. Interplanetary Particle Transport Modeling: This component simulates the transport of accelerated particles from the corona to 1 astronomical unit (1 au), which is the distance between the Sun and Earth. It takes into account the interplanetary magnetic field and other factors that influence particle propagation.
4. Comparison with Observations: The framework compares the modeled particle fluxes and fluences at 1 au with observations from instruments like the Solar and Heliospheric Observatory (SOHO) and the Energetic and Relativistic Nuclei and Electron (ERNE) instrument. It evaluates the accuracy of the model predictions by calculating metrics such as the Mean Squared Logarithmic Error (MSLE).

Overall, the SPREAdFAST framework combines detailed observations, physics-based modeling of coronal shocks and particle acceleration, and interplanetary transport modeling to analyze and forecast Solar Energetic Particle (SEP) events from the Sun to Earth.

#### 4.2.2 Data Analysis and Methodology

We used a combination of telescopic observations and dynamic physical models to simulate the acceleration of solar energetic particles (SEPs) in global coronal shock events. We first observed off-limb coronal bright fronts (CBF) and studied their interaction with the coronal plasma using synoptic magnetohydrodynamic (MHD) simulations. Based on these observations and simulations, we then employed an analytical diffusive shock acceleration (DSA) model to simulate the SEP acceleration. The simulated fluxes obtained from the DSA model were used as time-dependent inner boundary conditions for modeling the particle transport to 1 AU. This approach allowed us to study the early-stage acceleration and transport of SEPs from the Sun to 1 AU.

The criteria used to select the events for analysis in the study of the SPREAdFAST framework were as follows:

1. Proton events in the energy range of 17-22 MeV observed by the SOHO/ERNE instrument from 2010 to 2017 were initially identified.
2. Events without identified flares and coronal mass ejections (CMEs) and without EUV waves preceding the SEP event were excluded.
3. Events without EUV waves or no EUV data, even if they had identified flares/CMEs, were also excluded.
4. Uncertain EUV waves that were not relevant to the specific solar eruption were dropped.
5. Events with measurable near-limb or off-limb Coronal Bright Fronts (CBFs) that could be analyzed with the SPREAdFAST framework were selected.

In total, 62 events met the selection criteria and were included in the analysis.

The kinematics of Coronal Bright Fronts (CBFs) are characterized using the methodology of the Coronal Analysis of SHocks and Waves (CASHeW) framework. This framework estimates the CBF kinematics by following the leading edge of the front on consecutive images. It calculates the kinematics of the front, peak, and back edge of the CBFs over time, allowing for the estimation of their time-dependent mean intensity and thickness. The kinematics are determined using time-height maps (J-maps) generated with the CASHeW code for each event. The radial and lateral wave front positions are measured in these J-maps, providing information on the radial and lateral positions, speeds, accelerations, mean wave intensities, and wave thickness of the CBFs.

The methodology used to characterize the kinematics of Coronal Bright Fronts (CBFs) is based on the Coronal Analysis of SHocks and Waves (CASHeW) framework. This framework involves analyzing observations from the Atmospheric Imaging Assembly (AIA) instrument on board the Solar Dynamics Observatory (SDO). The kinematics of CBFs are determined by tracking the leading edge of the front on consecutive images. Time-height maps, also known as J-maps, are created by stacking columns of pixels in a desired direction from a solar image. The shape of the track on these J-maps depends on the direction and speed of the CBF. The CASHeW code identifies the radial and lateral wave front positions over time in the J-maps, allowing for the estimation of the CBF kinematics, including speeds, accelerations, mean wave intensities, and wave thickness. A three-dimensional geometric model, known as the Synthetic Shock Model (S2M), is then created based on the measured front positions, which describes the shock surface at regular intervals. This model is propagated through the solar corona using a synoptic coronal magnetohydrodynamic (MHD) model, providing information on the relevant parameters for coronal shock acceleration of solar energetic particles (SEPs).

In the SPREAdFAST DSA model, the shock-crossing field lines are modeled by dividing the shock surface into three regions: the "nose" of the shock model, which consists of model points on the spheroidal cap; and two flanks or zones, divided by a plane parallel to the Sun-Earth line. The plasma parameters at the points on these three surfaces are examined separately. The model calculates the proton acceleration along these shock-crossing field lines based on time-dependent estimates of shock speed, density jump ratio, magnetic field strength, and shock angle. The model solves for the coronal charged particle acceleration by large-scale CME-driven shocks and provides time-dependent distribution function spectra or fluxes as output.

The method used to compare the modeled and observed proton fluences is by analyzing scatter plots of the fitted power indices of the proton fluences from the EPREM model and the ERNE observations. The power law indices are compared between the two sets, and the onset hours for the proton events are also compared. The comparison helps evaluate the performance of the modeling framework in predicting the proton fluxes. Additionally, histograms and Mean Squared Logarithmic Error (MSLE) are used to assess the agreement between the modeled and observed fluence spectra and onset times.

#### 4.2.3 Results and Discussions

The study's findings have important implications for understanding and predicting solar particle radiation. By modeling the dynamics of shock waves and particle acceleration in the solar corona, the study provides valuable insights into the factors that influence the efficiency of particle acceleration. The results highlight the significant role of the coronal environment in shaping the acceleration and transport of solar energetic particles (SEPs) from the Sun to Earth. One key implication is that the overlying coronal structure and the particle energy play a crucial role in determining where SEPs are produced during CME-driven shock and compressive waves. The study shows that the large gradients in plasma parameters between neighboring streamers, quiet-Sun areas, and coronal holes lead to continuous changes in the acceleration process. This knowledge can help improve our understanding of the spatial distribution of SEPs and their energy dependence. Furthermore, the study's findings contribute to the development of physics-based models for forecasting SEP events. The SPREADFAST framework used in the study demonstrates the potential for accurately simulating the evolution of SEPs from the Sun to 1 AU. This framework can be further refined and utilized for early-stage forecasting of SEP events, providing valuable information for space weather prediction and mitigation efforts. Overall, the study enhances our understanding of the complex processes involved in solar particle radiation and provides a foundation for improving our ability to predict and mitigate the impacts of these events on space weather.

The main discrepancies between the modeled and observed fluxes in the study are primarily seen at higher energies. Above 15 MeV, there is a discrepancy in the time profile, with the observed proton fluxes rising approximately 1 hour before the simulation. Additionally, the fluxes at the highest energies show the most disagreement, mainly due to the slope of the increase and the onset times. These discrepancies indicate the need for further improvements and refinements in the modeling framework to better match the observations.

### 4.3 Solar Proton Flux Forecasting with Deep Learning Models

#### 4.3.1 Data preparation

In this section, I describe the physical quantities, the types of inputs and their sources, as well as the outputs I am forecasting. Some of the technical terms used in this study are explained further in the appendices.

In order to capture the variability of solar activity, which modulates the SEP flux, I selected input physical quantities that describe both the interplanetary medium and solar activity. These input features can be categorized into two groups: remote signatures and in-situ measurements. The remote signatures consist of the F10.7 index, as well as the long-wavelength ( $X_L$ ) and short-wavelength ( $X_S$ ) x-ray fluxes. The F10.7 index represents the flux of solar radio emission at a wavelength of 10.7 cm, measured in solar flux units (sfu). To obtain the x-ray fluxes, I utilized 1- and 5-minute averaged data from the Geostationary Operational Environmental Satellite (GOES) database<sup>2</sup>, specifically at long wavelengths (1 - 8 Å) and short wavelengths (0.5 - 4.0 Å).

The in-situ measurements encompass the near-Earth solar wind magnetic field and plasma parameters. These include the solar wind speed (in km s<sup>-1</sup>), average interplanetary magnetic field (IMF) strength (in nT), and the integral SEP fluxes at three energy channels: >10, >30, and >60 MeV, which correspond to the GOES channels (in 1/cm<sup>2</sup> sec ster). These SEP fluxes were obtained from multiple spacecraft stationed at the first Lagrange point (L1) throughout the study period. In particular, the IMF and plasma data in the OMNI database are obtained from the IMP, Wind, and ACE missions, while the energetic particle fluxes are obtained from the IMP and GOES spacecraft<sup>3</sup>.

---

<sup>2</sup>GOES SXR Database: <https://satdat.ngdc.noaa.gov/sem/goes/data/avg/>

<sup>3</sup>OMNIWeb Data Documentation: [https://omniweb.gsfc.nasa.gov/html/ow\\_data.html](https://omniweb.gsfc.nasa.gov/html/ow_data.html)

To ensure a comprehensive dataset, I acquired hourly-averaged data covering a timeframe from December 1976 to July 2019, which spans the past four solar cycles. These data were sourced from the Space Physics Data Facility (SPDF) OMNIWeb database<sup>4</sup>, hosted by the Goddard Space Flight Center. This database provides a wealth of information, including integral proton fluxes, as well as an extensive range of solar wind plasma and magnetic field parameters. Lastly, the daily data on sunspot numbers were obtained from the Sunspot Index and Long-term Solar Observations (SILSO) archive<sup>5</sup>, maintained by the World Data Center.

Figure 4.1 shows a plot for the timeseries data of all features. The top 3 panels are the logarithms of the SEP integral flux at the 3 energy channels (log\_PF10, log\_PF30, and log\_PF60), then the sunspot number, the F10.7 index (F10\_idx), the logarithms of the x-ray fluxes (log\_Xs and log\_Xl), the solar wind speed (Vsw), and the average magnitude of the IMF (avg\_IMF). Throughout this paper, I adopt the convention that "log" refers to the common logarithm with a base of 10. The gray shades refer to the timespan of solar cycles. The blue, orange, and gold colors refer to the training, validation, and test sets, respectively. The data split method will be explained shortly.

Since the input SEP data have been compiled from various spacecraft, it may have artifacts even after processing. In particular, there are occasional jumps in the background level. There are also several day-long gaps in the OMNI solar wind parameters from the early 1980s to mid-1990s where only IMP 8 data are available and this spacecraft spent part of each orbit in the magnetosphere. I am reasonably confident that these issues do not influence the overall analysis significantly.

In deep learning applications, the dataset is split into 3 sets; namely the training set, the validation set, and the test set. The training set is usually the largest chunk of data that is used to fit the model. The validation set is a smaller chunk of data used to fine-tune the model and evaluate its accuracy to ensure it is unbiased. The test set is the out-of-sample data exclusively used to assess the final model when performing on unseen data (Ripley 1996).

After inspecting the correlation between the solar wind indices and the SEP integral fluxes in the OMNIWeb database, I chose the top-correlated features with the SEP flux. The correlations were made between the SEP fluxes and the individual parameters. Hence I took only timeseries of logarithms of the protons' integral flux at 3 energy channels ( $>10$ ,  $>30$ , and  $>60$  MeV), the timeseries of logarithm of the X-ray fluxes, the F10.7 index, the sunspot number, the solar wind speed, and the average strength of the IMF as input parameters to our model. The log of the SEP flux was used across the whole study. The correlation matrices for the training, validation, and test sets are shown in Figure 4.2. The X-ray and proton fluxes were converted into the logarithmic form because it was more convenient than the original form of data since the time series data were mostly quiet and had numerous sharp spikes, which correspond to solar events. Based on a previous experience with NNs (Nedal et al. 2019), I found that training separate models for each target (output) feature can lead to better results. This is because a dedicated model for each output feature can more easily learn the interrelationships between input features and make more accurate predictions. Therefore, in our current study, I trained 3 separate models, each one targeting the logarithm of the protons integral flux at a specific energy channel.

In order to ensure consistency across all features, all durations of the time series data of the physical quantities were matched to be within the same time range. Subsequently, the dataset was resampled to obtain daily averaged data, resulting in a significant reduction of the dataset size by a factor of 24. This reduction facilitated expeditious training and yielded prompt results.

There were missing data values in the original dataset; for the  $B_{avg}$  ( $\sim 10.7\%$ ),  $V_{sw}$  ( $\sim 10.5\%$ ), F10.7-index ( $\sim 0.08\%$ ), short-band x-ray flux ( $\sim 8\%$ ), long-band x-ray flux ( $\sim 9.8\%$ ), and proton fluxes ( $\sim 4.3\%$ ). The data gaps were linearly interpolated.

In timeseries forecasting, it is a common practice to take a continuous set of data points from the main dataset to be the validation set and another smaller chunk of data to be the test set, for instance in Pala & Atici (2019); Benson et al. (2020); ?; Zhu et al. (2022). From our experiments, I got descent results when I applied the same data split method, but the results were a bit biased toward the end of the solar cycle 24 and the testing set was biased towards a quiet period. So, I adopted the 9-2-1 strategy, that is taking from each year 9 months to be added in the training set, 2 months to be added in the validation set, and 1 month to be added in the test set. This is applied over the  $\sim 43$  years of data (Fig. 4.1), which yields 74.29% of the data for the training set, 16.2% for the validation set, and 9.51% for the testing set. By doing so, I eliminated the need to do cross-validation and hence, made the training more efficient. It is worth to mention that the timeseries data must not be shuffled as that will break temporal and logical order of measurements, which must be maintained.

---

<sup>4</sup>OMNI Database: <https://omniweb.gsfc.nasa.gov>

<sup>5</sup>Sunspot Number Dataset: <https://www.sidc.be/silso/home>

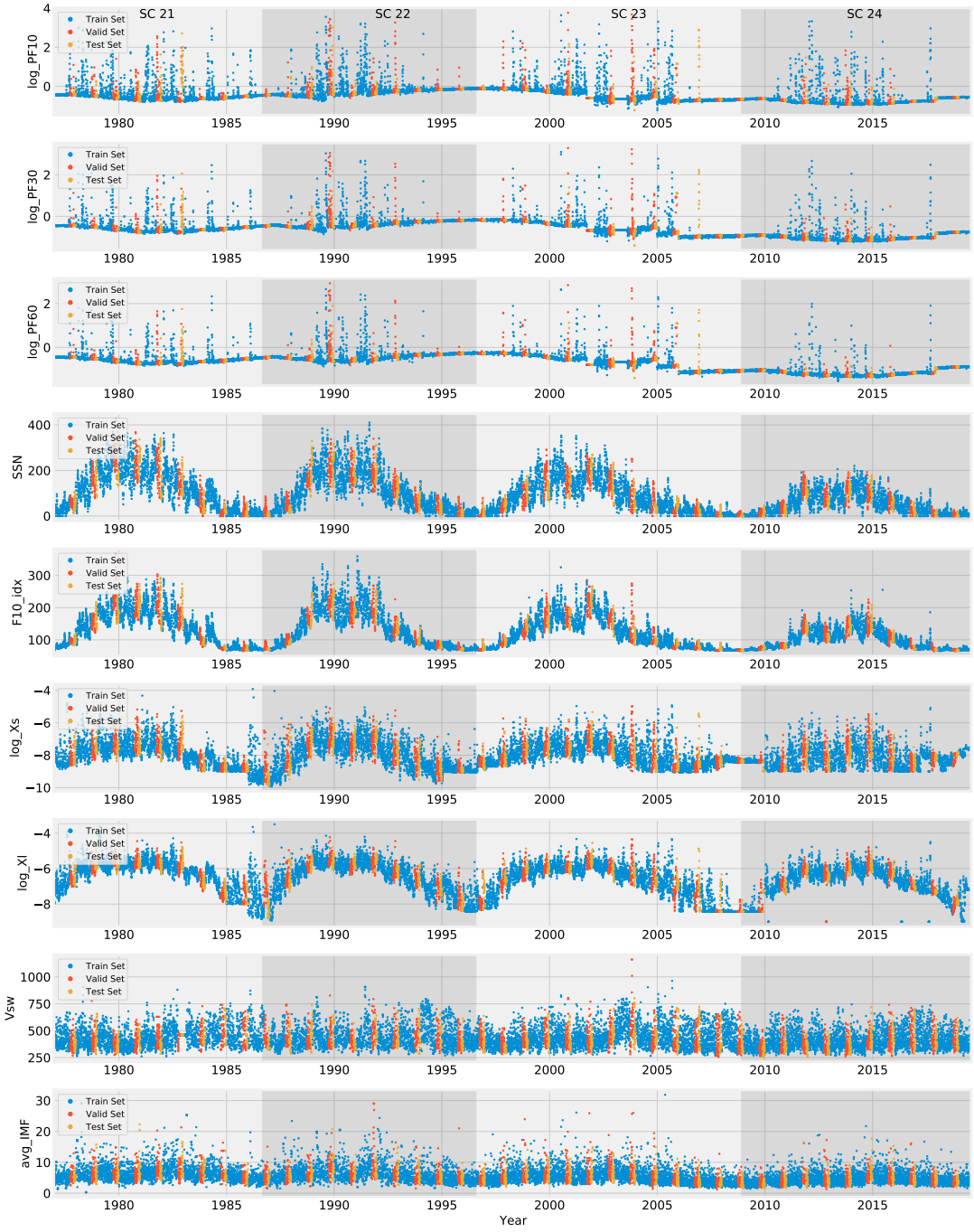


Figure 4.1: Data splitting for all input features, showing the training, validation, and testing sets. Daily data from 1976-12-25 00:00 to 2019-07-30 00:00. The gray shading labels the solar cycles from SC21 to SC24.

### 4.3.2 Method

In this section, I introduce the data analysis methods used in this work. I start with explaining the model selection phase, followed by a discussion of the bidirectional long-short-term memory (BiLSTM) neural network architecture. The technical terminologies are described in the appendices.

#### The Bi-LSTM Model

Recurrent neural networks (RNNs) that support processing input sequences both forward and backward are known as Bidirectional Long Short-Term Memory (BiLSTM) neural networks (Schuster & Paliwal

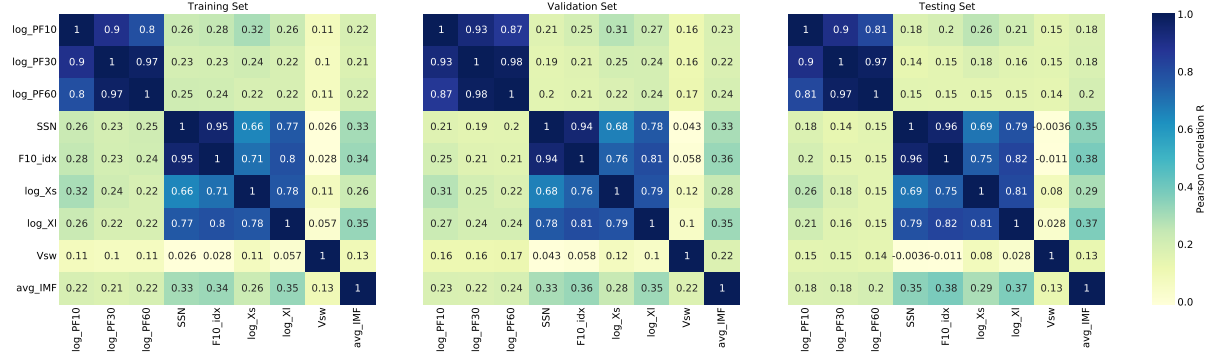


Figure 4.2: Correlation matrices show the correlation between the features in the training, validation, and test sets.

1997). Regular RNNs (Hochreiter & Schmidhuber 1997; Kolen & Kremer 2001) depend on the prior hidden state and the current input to determine the output at a given time. The output of a BiLSTM network, on the other hand, is dependent on the input at a given moment as well as the previous and future hidden states. As a result, the network is able to make predictions using contexts from the past as well as the future. Hence, accuracy is improving. Each BiLSTM layer consists of two LSTM layers; a forward layer that processes the input sequences from the past to future, and a backward layer that processes the input sequences from the future to the past, as illustrated in Figure 4.3, to capture information from both past and future contexts. The output from each layer is concatenated and fed to the next layer, which can be another BiLSTM layer or a fully connected layer for final prediction.

BiLSTM networks are advantageous than traditional LSTM networks in a variety of aspects (Graves & Schmidhuber 2005; Ihianle et al. 2020; Alharbi & Csala 2021). First, as I demonstrate in this study, they are excellent for tasks like timeseries forecasting, as well as speech recognition and language translation (Wöllmer et al. 2013; Graves & Jaitly 2014; Sundermeyer et al. 2014; Huang et al. 2018; Nammou et al. 2022) because they can capture long-term dependencies in the input sequence in both forward and backward directions. Second, unlike feedforward networks, BiLSTM networks do not demand fixed-length input sequences, thus being able to handle variable-length sequences better. Furthermore, by taking into account both past and future contexts, BiLSTM networks can handle noisy data. However, BiLSTM networks are computationally more expensive than regular LSTM networks due to the need for processing the input sequence in both directions. They also have a higher number of parameters and require more training data to achieve good performance.

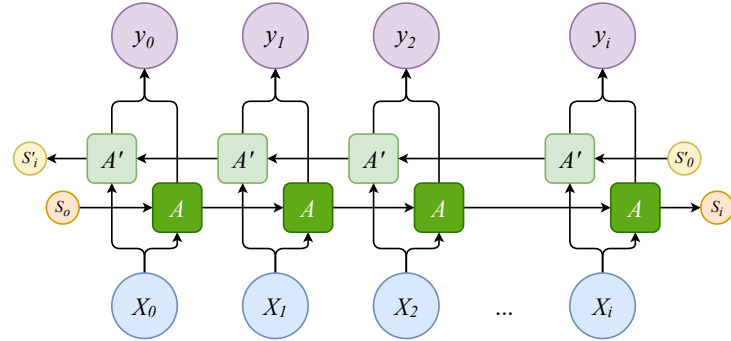


Figure 4.3: Architecture of a single BiLSTM layer. The blue circles at the bottom labeled by  $(x_0, x_1, x_2, \dots, x_i)$  are the input data values at multiple time steps. The purple circles, on the other hand, are the output data values at multiple time steps labeled by  $(y_0, y_1, y_2, \dots, y_i)$ . The dark green and light green boxes are the activation units of the forward layer and the backward layer, respectively. The orange and yellow circles are the hidden states at the forward layer and the backward layer, respectively. Both the forward and backward layers compose a single hidden BiLSTM layer. The figure is adopted from Olah (2015)

The final dataset has 7 features, including the target feature, from December 25<sup>th</sup> 1976 to July 30<sup>th</sup> 2019, with a total of 15,558 samples (number of days). The training set has 11,558 samples, the validation

set has 2,520 samples, and the test set has 1,480 samples.

The input horizon of 270 steps (30 days  $\times$  9 months) was used. A data batch size of 30 was used, which is the number of samples processed that result in one update to the model’s weights (Appendix A.2.2). The model consists of 4 BiLSTM layers with 64 neurons each, and an output dense layer with 3 neurons, representing the output forecasting horizon. The total number of trainable parameters is 333,699. The number of training epochs was set to 50 because from experiments, the model stopped improving remarkably after almost 50 epochs. Thus, there was no need to waste time and computational resources to train the model for more than 50 epochs.

The *ModelCheckpoint* callback function was used to register the model version with the minimal validation loss. The *EarlyStopping* callback function was used to halt the model run when detecting overfitting, with a *patience* parameter of 7. *ReduceLROnPlateau* callback function was used to reduce the learning rate when the validation loss stops improving, with a *patience* parameter of 5, a reduction factor of 0.1 and minimal learning rate of  $1e^{-6}$ .

## Model Selection

To determine the most suitable model for our objective and provide justifiable reasons, I conducted the following analysis. First I examined the naive (persistence) model, which is very simplistic and assumes that the timeseries values will remain constant in the future. In other words, it assumes that the future value will be the same as the most recent historical value. That was the baseline. Next I examined the moving-average model, which calculates the future values based on the average value of historical data within a specific time widow. This gives a little bit lower error.



Figure 4.4: Illustration of the sliding window technique for a sample of 10 timesteps, where each number denotes a distinct time step. As an example here, the input horizon (blue color) length is 4 timesteps and the output horizon length is 3 timesteps. The input window slides 1 time step at a time across the entire data sequence to generate 4 distinct input and forecast horizon pairs. The purple, orange, and green colors of the output horizon represent 1-day, 2-day, and 3-day ahead forecasting, respectively. The timesteps of 1-day ahead forecasting across the data sequences are then concatenated into a single timeseries list that is called 1-day ahead prediction. The same for 2-day and 3-day ahead.

After that, I went towards the machine learning (ML)-based models. For all the ML models, I chose the Adaptive moment estimation (Adam) optimizer (Kingma & Ba 2015) as the optimization algorithm due to its minimal memory requirements and high computational efficiency as it is well-suited for applications that involve large number of parameters or large datasets. As a rule of thumb, I set the optimizer’s learning rate to be 0.001 as it is usually recommended (?).

In order to prepare the data in a readable format to the ML models, I created a windowed dataset with an input horizon of 365 steps representing 1 year of data and an output horizon of 3 steps representing the forecast window of three days. I call this windowing method as Multi-Input Multiple Output (MIMO) strategy, in which the entire output sequence is predicted in one shot. The MIMO strategy adopts the sliding window method that was mentioned in Benson et al. (2020) in which each sequence is shifted by one step with respect to the previous sequence until reaching the end of the available data (Fig. 4.4). This approach minimized the imbalance of active days, with high SEP fluxes, and quiet days.

After experiments with different loss functions and evaluate their performance on our dataset, I chose the Huber function A.9a as the loss function and the Mean Absolute Error (MAE) is used as the metric function to monitor the model performance. I used the Huber function because it is robust and combines the advantages of both Mean Squared Error (MSE) and MAE loss functions. It is less sensitive to outliers than MSE, while still being differentiable and providing gradients, unlike MAE. Since our data is noisy

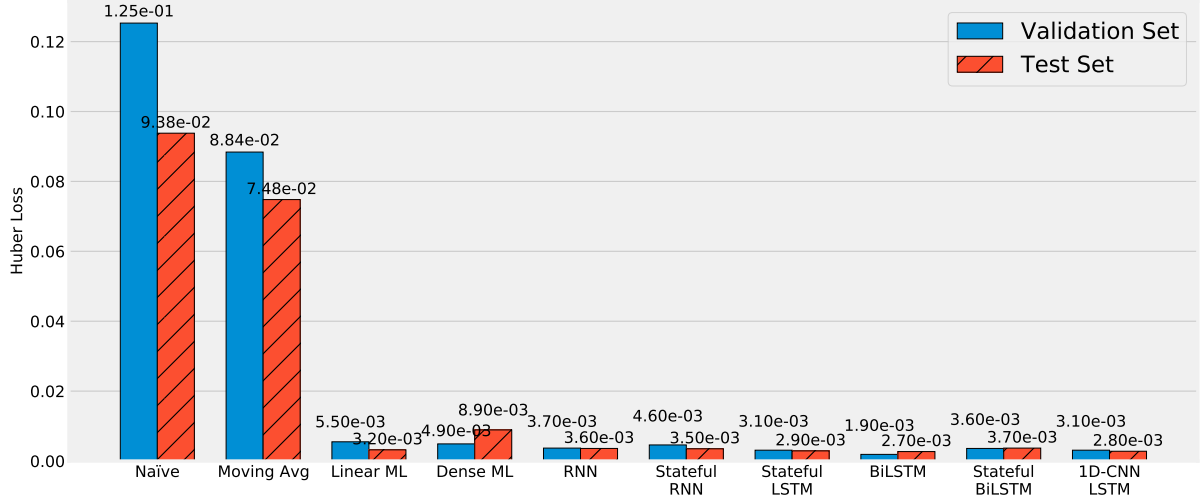


Figure 4.5: Benchmarking of 10 models, shows the Huber loss for the validation and test sets.

and contains outliers that may negatively impact the model’s performance, the Huber loss function is a good choice.

I examined various neural network models to determine the optimal architecture for our task. Initially, I started with a simple linear model comprising of a single layer with a single neuron. However, this model did not yield satisfactory results. I then explored a dense ML model consisting of two hidden layers, each with 32 neurons and a *ReLU* activation function. Next, I experimented with a simple RNN model with the same number of hidden layers and neurons. To find the optimal learning rate, I utilized the *LearningRateScheduler* callback function and discovered that a rate of  $1.58e^{-4}$  under the basic settings minimized the loss. I proceeded to examine stateful versions of RNN, LSTM, and BiLSTM models with three hidden layers, each with 32 neurons and a learning rate of  $1.58e^{-4}$ . In addition, I explored a hybrid model that consisted of a 1-dimensional convolutional layer with 32 filters, a kernel size of 5, and a *ReLU* activation function. I combined this with a two-hidden layer LSTM network with 32 neurons each and a learning rate of  $1.58e^{-4}$ . I experimented with *Dropout* layers but did not observe any significant improvement in the results. Finally, I evaluated a BiLSTM model with five hidden layers, 64 neurons each, and a learning rate of 0.001. Based on the evaluation of all the models on both the validation and test sets (Fig. 4.5 and Table A.2), I selected the BiLSTM model for further refinement. More details on the final model architecture and hyperparameters are explained in the Appendix A.2.4. Figure 4.5 presents a comparative analysis of the Huber loss within the validation and testing sets across the ten aforementioned models. I used several evaluation measures to assess our models since each metric provides valuable insights into the accuracy and performance of the forecasts (Appendix A.2.3), helping to identify areas for improvement and adjust the forecasting models accordingly.

### 4.3.3 Results and discussion

The benchmarking in Figure 4.5 showed that, in general, the ML-based methods were not much different. On the other hand, the persistence model and moving average model resulted in the highest errors compared with the ML-based models, and their results were close to some extent. As I see, the BiLSTM model performed the best over both the validation and test sets compared with the other models.

I developed and trained 3 BiLSTM models to forecast the integral flux of SEP, one model per energy channels. After the training was completed, I evaluated the performance of the models from the loss curve (Fig. 4.6) using the Huber loss (the left panel) and the metric MAE (the middle panel). During the training, the learning rate was reduced multiple times via the *LearningRateScheduler* callback function (the right panel). The left panel quantifies the discrepancy between the model’s predictions and the true values over time. It shows how the Huber loss function changes during the training iterations (Epochs) for the training and validation sets for the three energy channels so that each channel has one color. The middle panel shows how the model’s metric MAE changes with training epochs. It is used to evaluate the performance of the trained model by measuring the average absolute difference between the model’s predictions and the true values, providing a single numerical value that indicates the model’s error at a given epoch. The right panel shows how the learning rate of the model’s optimizer changes with epochs

via the *LearningRateScheduler* callback function, which changes the learning rate based on a predefined schedule to improve training efficiency and convergence. The learning rate refers to the rate at which the model's parameters are updated during the training process. I noticed that at the epochs where the learning rate has changed, there were bumps in the loss curves across all the energy channels, which is expected. This highlights the boundaries within which the learning rate yields better performance.

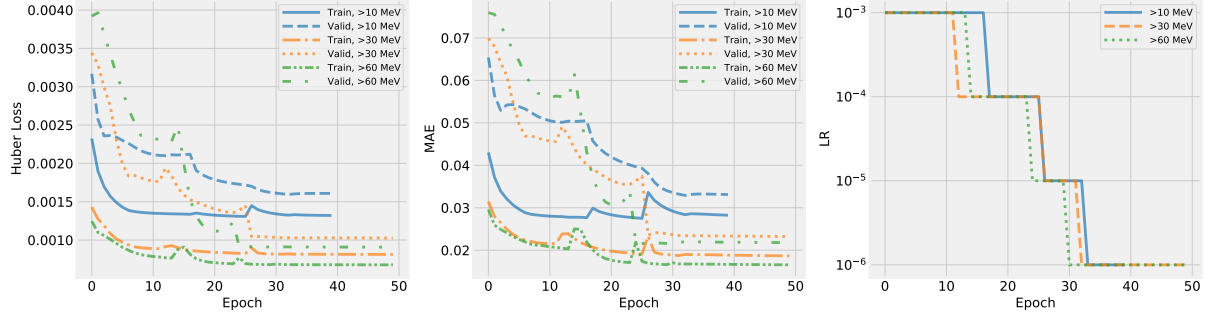


Figure 4.6: *Left Panel* - The Huber loss vs. the number of training epochs for the BiLSTM model for the validation and test sets, for the 3 energy channels. *Middle Panel* - The mean absolute error (MAE); the model's metric vs. the number of training epochs. *Right Panel* - Shows how the learning rate of the Adam optimizer changes over the number of epochs.

From experimentation, I found that the batch size and the optimizer learning rate are the most important hyperparameters that have a strong influence on the overall model's performance (Greff et al. 2016). In addition, adding *dropout* layers as well as varying the number of hidden layers and hidden neurons resulted in only marginal improvements to the final model performance, while substantially increasing training time and requiring greater computational resources.

The term *batch size* refers to the number of data sequences processed in one iteration during the training of a ML model (Goodfellow et al. 2016). Initially, a batch size of 64 was selected, however, I observed that the model produced better results when a batch size of 30 was used instead. This could be related to the Carrington rotation, which lasts for  $\sim 27$  days. There were  $\sim 570$  Carrington rotations between December 25<sup>th</sup> 1976 and July 30<sup>th</sup> 2019. Therefore, updating the model's weights after every Carrington rotation could be a reasonable choice for improving its performance. Figure 4.7 shows how good the model predictions are (on the y-axis) compared with the observations of the validation set (on the x-axis). The blue, orange, and gold colors refer to 1-day, 2-day, and 3-day ahead predictions, respectively. The top panel is for the >10 MeV channel, the middle panel is for the >30 MeV channel, and the bottom panel is for the >60 MeV channel. The left column is for the entire validation set, while the right column is for the observations points  $\geq 10$  proton flux units (pfu). That is the threshold value of proton flux as measured by the National Oceanic and Atmospheric Administration (NOAA) GOES spacecraft to indicate severity of space weather events caused by SEP.

I found that, overall, the models performed very well. The *R* correlation was  $>0.9$  for all points of the validation set across the forecasting windows for the 3 energy channels. The *R* correlation was  $>0.7$  for the observations points  $\geq 10$  pfu as well. However, the correlation between the modeled data and the observations exhibited a decline as the forecast horizon increased, in accordance with the anticipated result. To confirm the validity of the models, I performed the same correlation analysis between the modeled data and the observations of the out-of-sample test set (Fig. 4.8), which was not given to the model. Again, I found a high correlation across the forecasting windows for the 3 energy channels. The points were more dispersed between 1 and 1.5 on the x-axis, which reflected in a bit lower correlation. This might be a limitation in the current version of the model between that range of SEP fluxes since the models underestimated the flux values within that range across all energy channels, possibly due to the relatively smaller training samples with fluxes above 10 pfu compared with the majority of the data.

In order to see the temporal variation of the correlation between the modeled data and the observations, I applied a rolling window of 90 steps (3 months  $\times$  30 days/month = 1 season) that shows the seasonal variation of the correlation, as shown in Figure 4.9. Here, I show only the 1-day ahead predictions for the test set, for the 3 energy channels. I observe drops in the correlation factor synchronized with the transition between solar cycles (e.g., particularly between  $\sim 1995$  - 2000, which represents the declining phase of the solar cycle 22 and the rising phase of the solar cycle 23). This could be related to the fact that the low SEP fluxes during quiet times are more random and thus more difficult to forecast

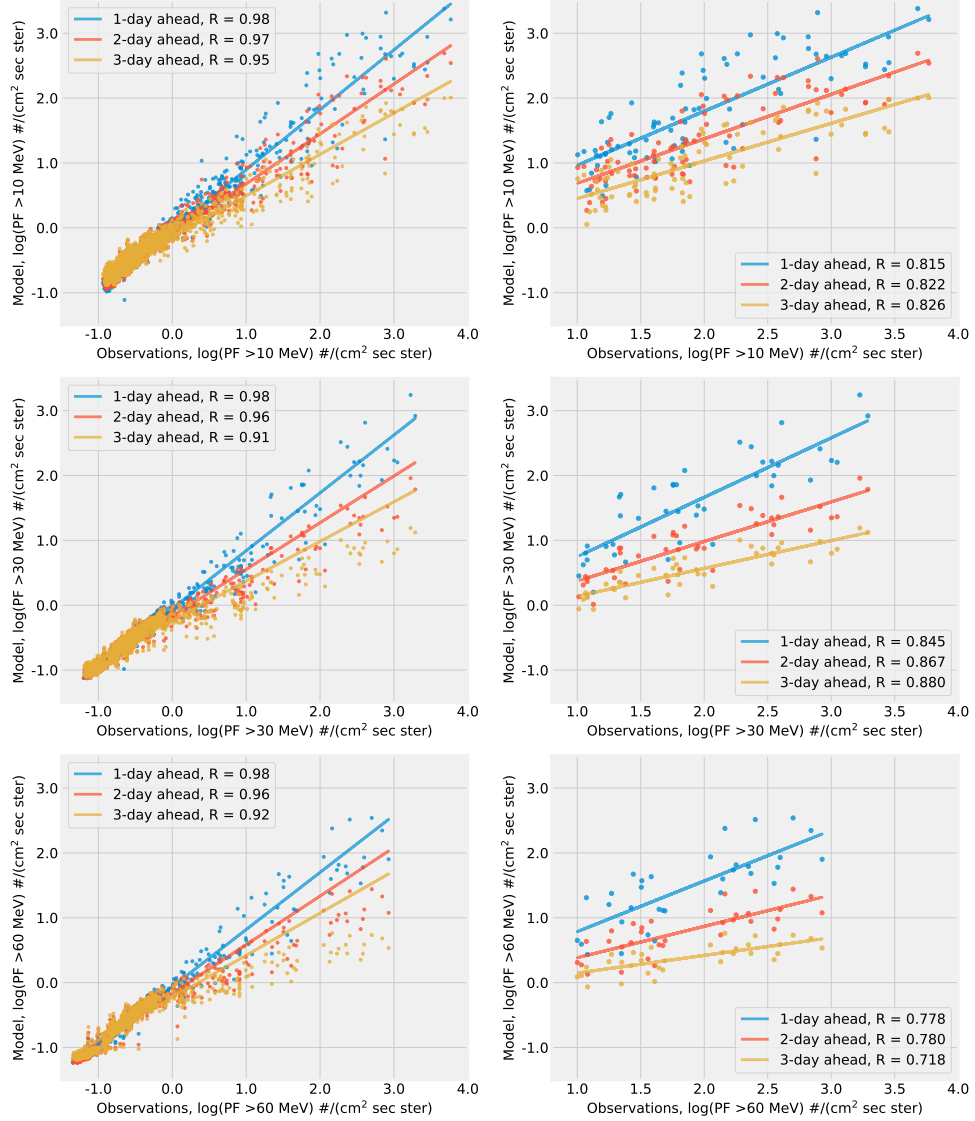


Figure 4.7: Correlation between the model predictions and observations for 1-day, 2-day, and 3-day ahead for  $>10$  MeV (top panel),  $>30$  MeV (middle panel), and  $>60$  MeV (bottom panel). The panels in the left column represent all the points of the validation set, those in the right column represent all the observations points with daily mean flux  $\geq 10$  pfu.

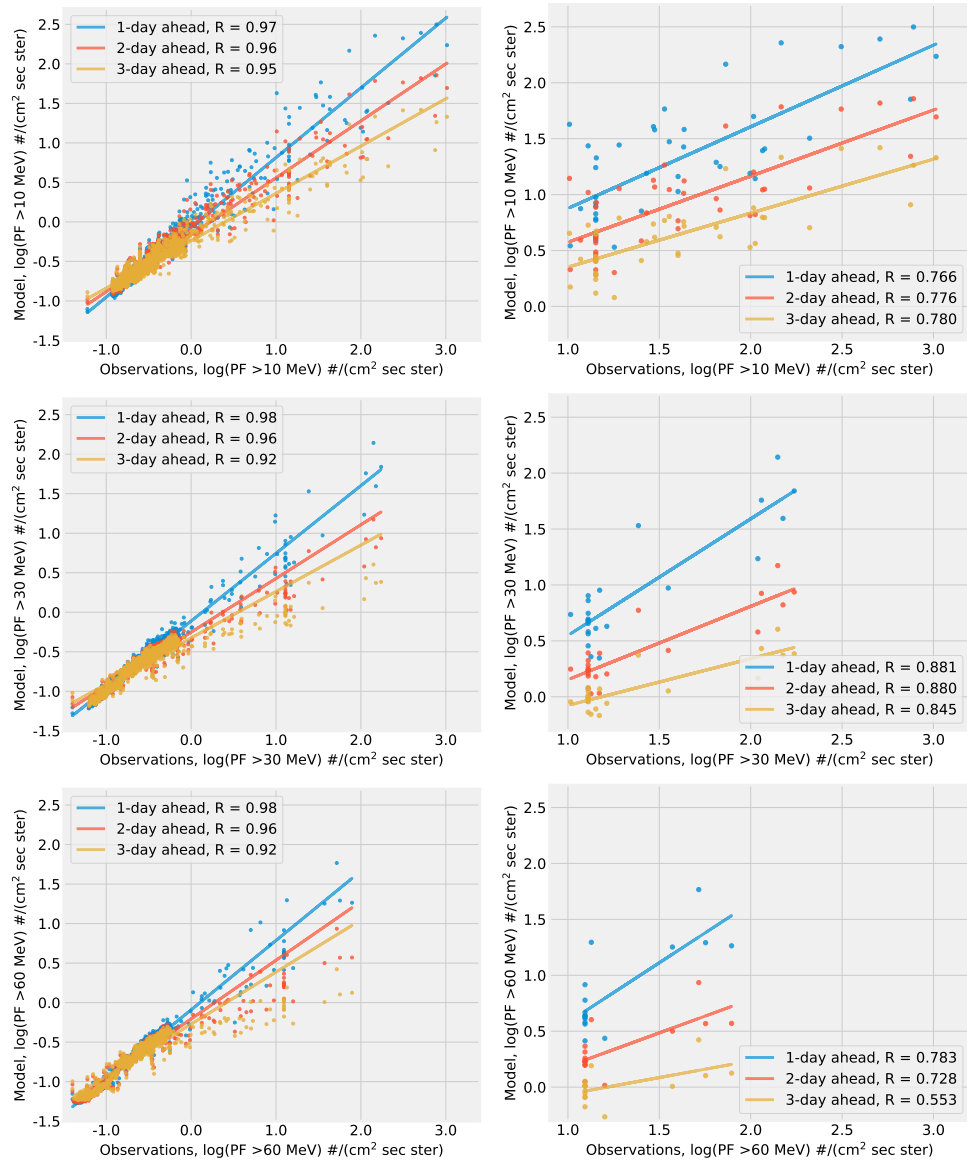


Figure 4.8: Same as Figure 4.7 but for the test set.

(Feynman et al. 1990; Gabriel et al. 1990; Rodriguez et al. 2010; Xapsos et al. 2012).

During periods of low solar activity, the forecasting of low SEP fluxes becomes more challenging due to their increased randomness. This difficulty arises from the reduced occurrence of conventional SEP drivers, such as solar flares and CMEs. Studies have suggested that the most significant solar eruptions tend to happen shortly before or after the solar cycle reaches its maximum (Svestka 1995). Additionally, sporadic increases in solar activity have been observed (Kane 2011), which might contribute to the diminished correlations observed in our research. There is clearly some factor that is influencing the correlation during certain periods where there are no or only weak SEP events. However, it is not obvious which physical phenomena are the cause rather than, for instance, some artifact of the data. Understanding the interplay between these factors and their influence on SEP fluxes during periods of reduced solar activity remains a critical area of research. It would be interesting to find what is reducing the correlations, thus more investigation is needed.

Overall, the modeled data was correlated the most with observations at  $>60$  MeV, then the second rank was for the  $>10$  MeV channel, and the third rank was for the  $>30$  MeV channel. That could be related to the relatively larger extent of drops in correlation at the  $>30$  MeV channel. The decline in correlation at the  $>30$  MeV channel is consistent with the findings of Le & Zhang (2017). A summary of the performance results of the models for both the validation set and test set is presented in Table 4.1.

From the visual inspection of the test set examples (Fig. 4.10, 4.11, and 4.12), I found that the predicted onset time, the peak time, and end times of SEP events were highly correlated with those of the observations, which implies that the model captured the temporal variations, as well as the trends in SEP flux.

Table 4.1: Summary of the performance results of the models for the validation and test sets.

| Validation Set |                  |        |        |                  |        |        |                  |        |        |
|----------------|------------------|--------|--------|------------------|--------|--------|------------------|--------|--------|
|                | log PF $>10$ MeV |        |        | log PF $>30$ MeV |        |        | log PF $>60$ MeV |        |        |
| Model Loss     | 0.0016           |        |        | 0.0010           |        |        | 0.0009           |        |        |
| Model Metric   | 0.0329           |        |        | 0.0232           |        |        | 0.0218           |        |        |
|                | 1-Day            | 2-Day  | 3-Day  | 1-Day            | 2-Day  | 3-Day  | 1-Day            | 2-Day  | 3-Day  |
| MAE            | 0.061            | 0.091  | 0.125  | 0.053            | 0.079  | 0.098  | 0.052            | 0.069  | 0.086  |
| MSE            | 0.013            | 0.028  | 0.054  | 0.010            | 0.031  | 0.055  | 0.009            | 0.027  | 0.047  |
| RMSE           | 0.114            | 0.168  | 0.233  | 0.098            | 0.176  | 0.234  | 0.097            | 0.164  | 0.217  |
| MAPE           | 22.156           | 28.104 | 34.721 | 13.039           | 18.590 | 22.735 | 10.036           | 13.994 | 16.731 |
| Test Set       |                  |        |        |                  |        |        |                  |        |        |
|                | log PF $>10$ MeV |        |        | log PF $>30$ MeV |        |        | log PF $>60$ MeV |        |        |
| Model Loss     | 0.0014           |        |        | 0.0011           |        |        | 0.0010           |        |        |
| Model Metric   | 0.0333           |        |        | 0.0283           |        |        | 0.0250           |        |        |
|                | 1-Day            | 2-Day  | 3-Day  | 1-Day            | 2-Day  | 3-Day  | 1-Day            | 2-Day  | 3-Day  |
| MAE            | 0.072            | 0.099  | 0.125  | 0.053            | 0.088  | 0.107  | 0.045            | 0.066  | 0.081  |
| MSE            | 0.015            | 0.030  | 0.050  | 0.009            | 0.029  | 0.048  | 0.007            | 0.020  | 0.034  |
| RMSE           | 0.121            | 0.172  | 0.224  | 0.094            | 0.170  | 0.218  | 0.082            | 0.141  | 0.184  |
| MAPE           | 30.135           | 37.498 | 48.139 | 20.599           | 34.300 | 40.803 | 12.358           | 20.504 | 25.305 |

To get further insight into the model’s performance, I conducted an assessment of various skill scores, including True Positive (TP), True Negative (TN), False Positive (FP), and False Negative (FN). Additionally, skill score ratios such as Probability of Detection (POD), Probability of False Detection (POFD), False Alarm Rate (FAR), Critical Success Index (CSI), True Skill Statistic (TSS), and Heidke Skill Score (HSS). Detailed descriptions of these skill scores can be found in Appendix A.2.5. To extract individual SEP events from the test dataset, I implemented a threshold-based clustering algorithm. This algorithm uses the NOAA/SWPC warning threshold value of 10 pfu for the  $E \geq 10$  MeV channel. Upon analysis, I identified the number of detected SEP events for each output forecasting window and calculated the skill scores (Table 4.2). In the true test set, I identified 12 SEP events.

The evaluation of the model revealed notable trends as the length of the output forecasting window increased. The POD and CSI exhibited a declining pattern, indicating a reduced ability of the model to accurately detect and capture positive events (SEP occurrences) as the forecasting horizon extended further into the future. This suggests that the model’s performance in identifying and capturing true positive instances diminishes with longer forecasting windows. Moreover, the POFD demonstrated an increasing trend, indicating an elevated rate of false positive predictions as the forecasting horizon length-

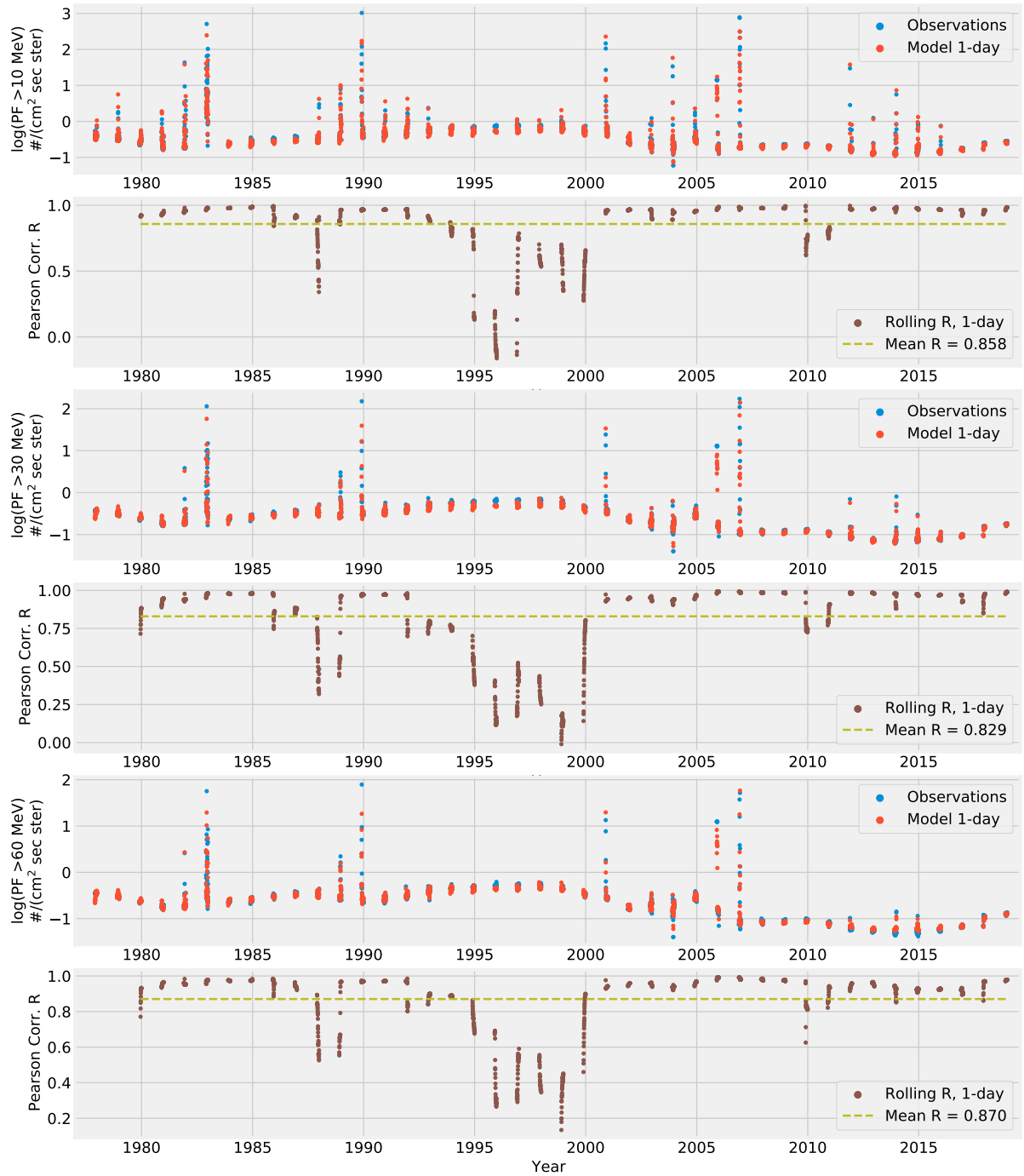


Figure 4.9: Comparison between the model outputs and observations of the test set for the 3 energy channels. In addition to the rolling-mean window correlation for 1-day ahead predictions.

ened. The model's propensity to generate false alarms rose with the lengthening forecasting window, leading to incorrect identification of non-events as positive events. Consequently, the TSS and HSS exhibited decreasing values, signifying a deterioration in the model's overall skill in accurately capturing and distinguishing between positive and negative instances. Overall, our skill scores are comparable with those reported by previous studies (Table 4.3). Although the UMASEP model does better than ours (i.e., has a higher POD), our FAR is much lower, thus, making fewer false alarms than the UMASEP model.

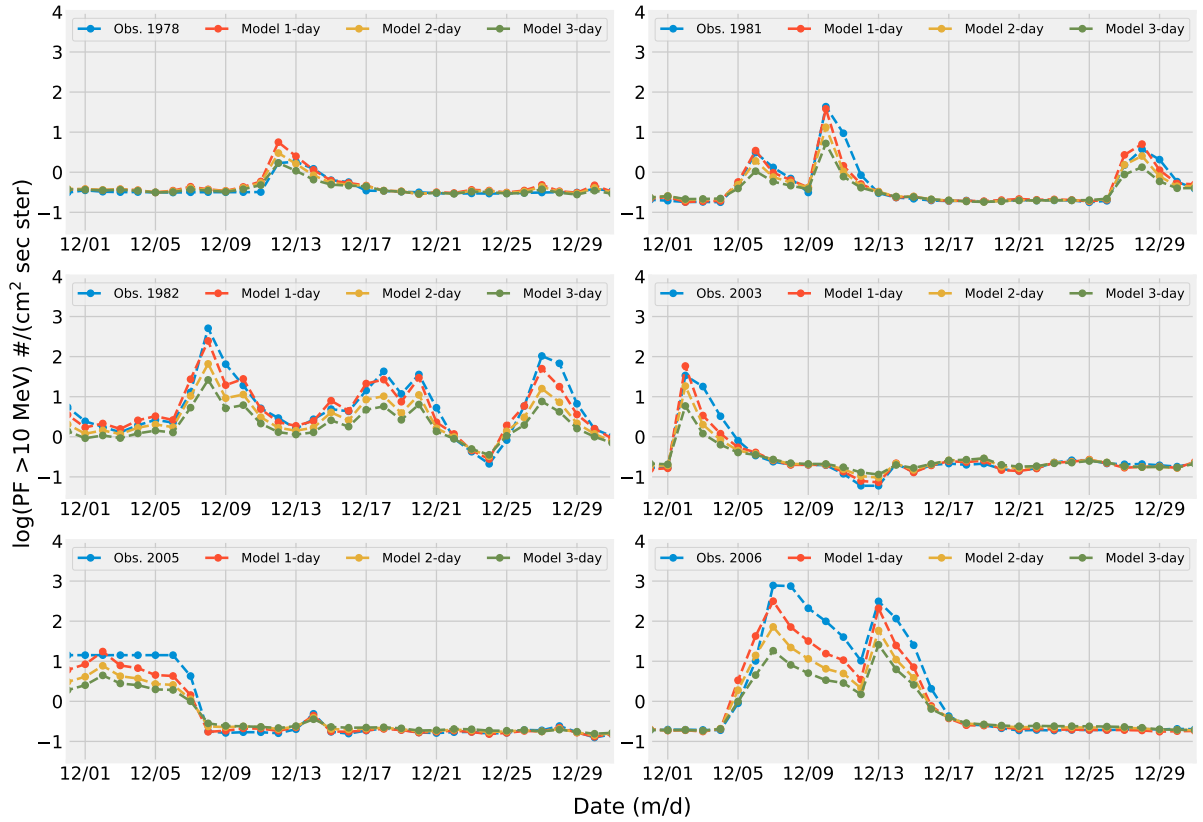


Figure 4.10: The model's forecasts for the out-of-sample testing set for the  $>10$  MeV channel are shown at forecast horizons of 1 day, 2 days, and 3 days ahead, using samples of data from December in selected years mentioned in the top-left side of the plots.

Table 4.2: Confusion matrix for the energy channel  $\geq 10$  MeV predictions in the test set.

| E >10 MeV   | No. events | TP | TN   | FP | FN |
|-------------|------------|----|------|----|----|
| 1-day ahead | 15         | 21 | 1441 | 2  | 13 |
| 2-day ahead | 13         | 14 | 1441 | 2  | 20 |
| 3-day ahead | 5          | 5  | 1443 | 0  | 29 |

Table 4.3: Comparing the skill scores with previous models. The dashed entries mean the data is unavailable (Whitman et al. (2023) for more details).

| Model                              | POD   | FAR   | TSS   | HSS   | POFD  | CSI   | Accuracy | Precision |
|------------------------------------|-------|-------|-------|-------|-------|-------|----------|-----------|
| Our BiLSTM model                   | 0.618 | 0.087 | 0.531 | 0.732 | 0.001 | 0.583 | 0.99     | 0.913     |
|                                    | 0.412 | 0.125 | 0.287 | 0.553 | 0.001 | 0.389 | 0.985    | 0.875     |
|                                    | 0.147 | 0     | 0.147 | 0.252 | 0     | 0.147 | 0.980    | 1         |
| UMASEP-10 (Núñez 2011)             | 0.822 | 0.219 | —     | —     | —     | —     | —        | —         |
| PCA (Papaioannou et al. 2018)      | 0.587 | 0.245 | —     | 0.65  | —     | —     | —        | —         |
| SPARX (Dalla et al. 2017)          | 0.5   | 0.57  | —     | —     | 0.32  | 0.3   | —        | —         |
| SPRINTS (Engell et al. 2017)       | 0.56  | 0.34  | —     | 0.58  | —     | —     | —        | —         |
| REleASE (Malandraki & Crosby 2018) | 0.63  | 0.3   | —     | —     | —     | —     | —        | —         |

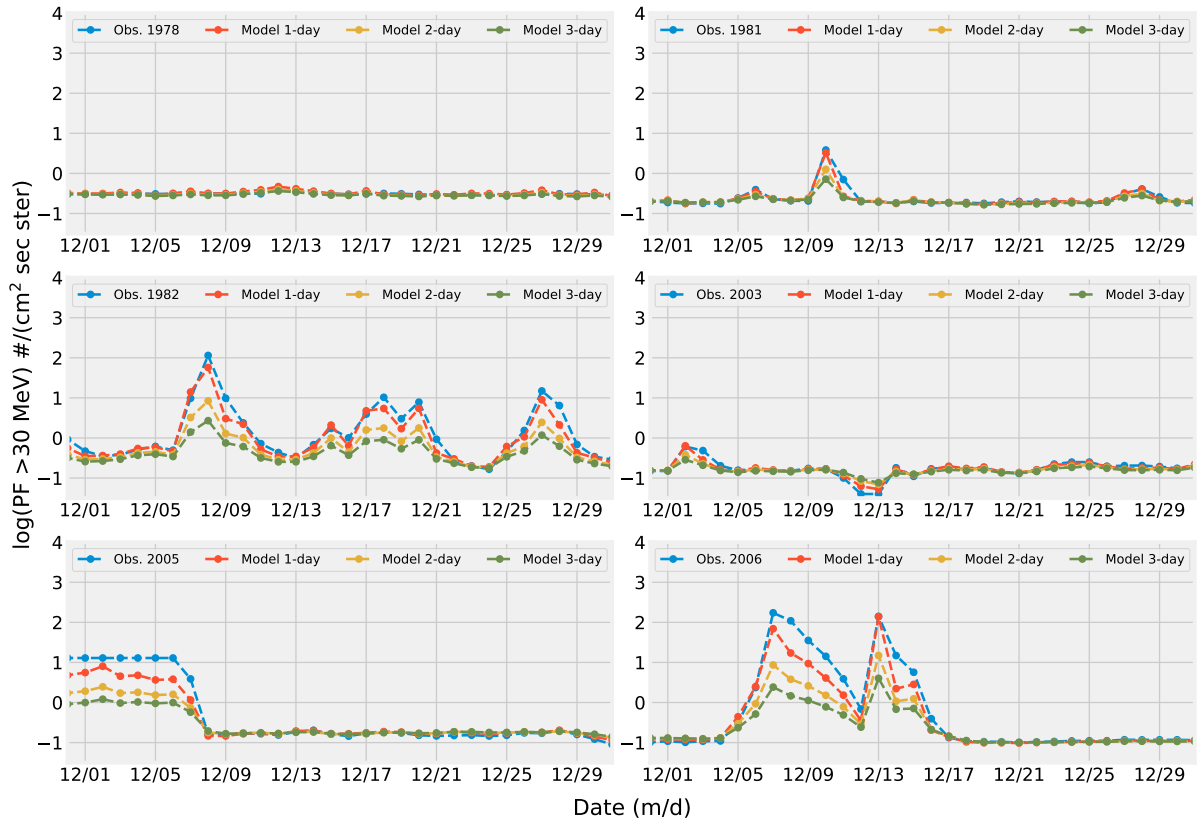


Figure 4.11: The model's forecasts for the out-of-sample testing set for the  $>30$  MeV channel are shown at forecast horizons of 1 day, 2 days, and 3 days ahead, using samples of data from December in selected years mentioned in the top-left side of the plots.

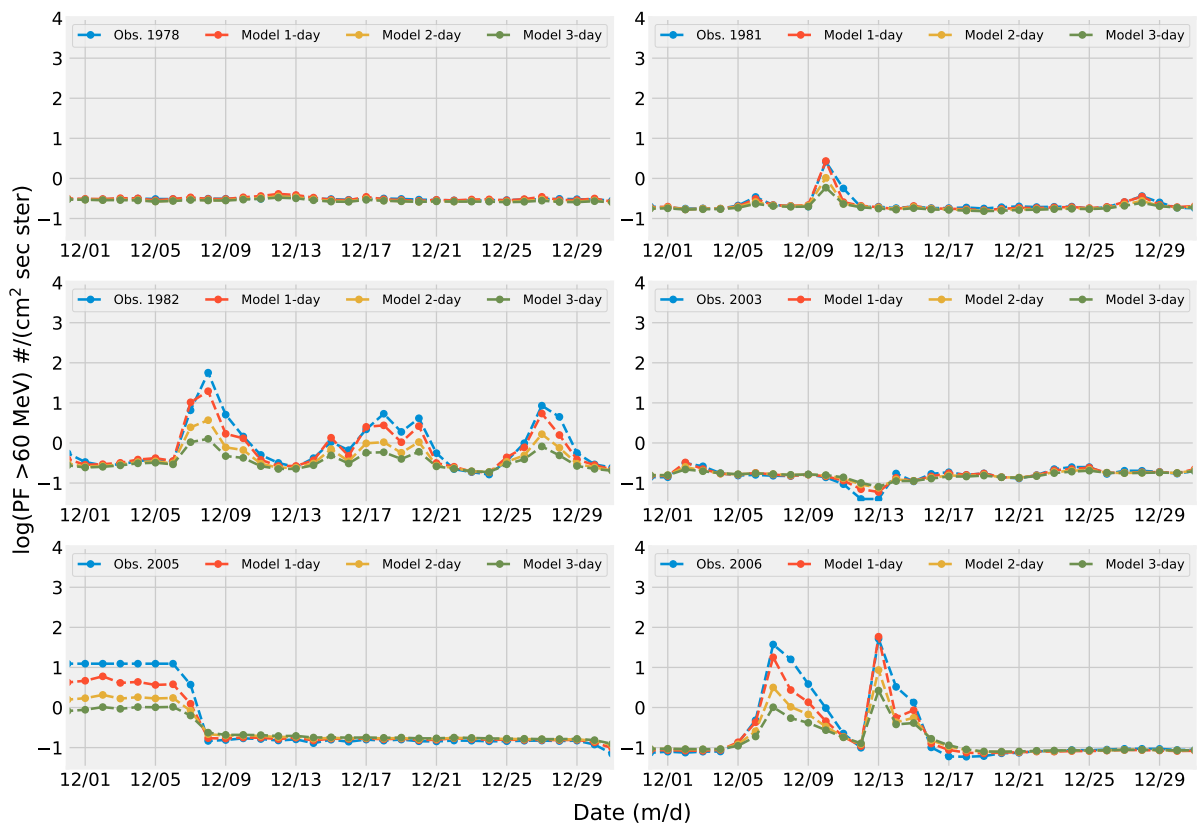


Figure 4.12: The model's forecasts for the out-of-sample testing set for the  $>60$  MeV channel are shown at forecast horizons of 1 day, 2 days, and 3 days ahead, using samples of data from December in selected years mentioned in the top-left side of the plots.

## 4.4 Conclusions

Forecasting the SEP flux is a crucial task in heliophysics since it affects satellite operations, astronaut safety, and ground-based communication systems. It is a challenging task due to its non-linear, non-stationary, and complex nature. Machine learning techniques, particularly neural networks, have shown promising results in predicting SEP flux. In this study, I developed and trained BiLSTM neural network models to predict the daily-averaged integral flux of SEP at 1-day, 2-day, and 3-day ahead, for the energy channels  $>10$  MeV,  $>30$  MeV, and  $>60$  MeV. I used a combination of solar and interplanetary magnetic field indices from the OMNIWeb database for the past 4 solar cycles as input to the model. I compared the models with baseline models and evaluated them using the Huber loss and the error metrics in Appendix A.2.

The data windowing method I used, based on the MIMO strategy, eliminates the need to feed the output forecast as input back into the model and that allows to do forecasting relatively far into the future while maintaining decent results (e.g., the MSE is ranging between 0.007 and 0.015 for 1-day forecasting in the test set, compared to an MSE of 0.236 for a persistence model. See Table 4.1). The results show that the model can make reasonably accurate predictions given the difficulty and complexity of the problem. The MSE was ranged between 0.009 and 0.055 for the validation set, and between 0.007 and 0.05 for the test set. The correlations between the observations and predictions were  $>0.9$  for the validation and test sets (Fig. 4.7 and Fig. 4.8). Nevertheless, the mean temporal correlation was  $\sim 0.8$  for the test set (Fig. 4.9). Although our models performed well, I observed a relatively large discrepancy between the predictions and the observations in the  $>30$  MeV energy band.

The findings of this study underscore the challenges encountered by the forecasting model in accurately predicting SEP data over longer time periods. As the length of the output forecasting window increased, the model's ability to detect true positives and its overall skill in differentiating positive and negative instances diminished. Additionally, the model displayed an elevated rate of false negative predictions, indicating an increased tendency to generate misses as the forecasting horizon extended. These results highlight the importance of carefully considering the appropriate forecasting window length for SEP data to ensure the model's optimal performance. Our skill scores generally align with those from previous works (Table 4.3). There are variations in the metrics' values across different studies, highlighting the complexities and nuances associated with each study. Nevertheless, it is important to acknowledge that the statistical significance of the results in this study is limited due to data averaging. Future studies should consider incorporating hourly data, as this is likely to result in a greater number of identified events. The model can provide short-term predictions, which can be used to anticipate the behavior of the near-Earth space environment. These predictions have important implications for space weather forecasting, which is essential for protecting satellites, spacecraft, and astronauts from the adverse effects of solar storms.

Multiple techniques exist for identifying the optimal combination of hidden layers and neurons for a given task such as empirical methods, parametric methods, and the grid search cross-validation method, which I will explore in future work. The observed reduction in correlation necessitates further investigation to determine its origin, whether stemming from tangible causal factors or potential aberrations within the model or data. I plan to expand upon this work by performing short-term forecasting using hourly-averaged data. This extension will involve integrating additional relevant features such as the location and area of active regions and coronal holes on the Sun.

BiLSTM networks are particularly useful for tasks involving sequential data such as timeseries forecasting. Given their capacity to handle input sequences in both directions in time and capture long-term dependencies, they are valuable in a broad range of applications. Nonetheless, one should carefully consider their data requirements and computational complexity before adopting them. Our results emphasize that the use of deep learning models in forecasting tasks in heliophysics are promising and encouraging, as pointed out by Zhang et al. (2022b).

This work is a stepping stone towards real-time forecasting of SEP flux based on the public-available datasets. As an extension, I am currently working on developing a set of models that deliver near-real time prediction of SEP fluxes at multiple energy bands, multiple forecasting windows, with hourly-averaged data resolution, with a more sophisticated model architecture, as well as more features that address the state of solar activity more comprehensively. I plan to extend the analysis to include more recent data from solar cycle 25, in order to improve the accuracy of the models. In conclusion, our study highlights the potential of using BiLSTM neural networks for forecasting SEP integral fluxes. Our models provide a promising approach for predicting the near-Earth space environment too, which is crucial for space weather forecasting and ensuring the safety of our space assets. Our findings contribute

to the growing body of literature on the applications of deep learning techniques in heliophysics and space weather forecasting.

# Chapter 5

## Summary and Future Work

### 5.1

### 5.2

### 5.3

### 5.4

### 5.5 Future Work

The research presented in this thesis establishes an important foundation and provides a precursor for future advances that can build upon the present work. Some open questions and promising areas for future investigations include:

- Additional coronal wave statistical studies using expanded event samples and new imaging datasets from Solar Orbiter and ground observatories to improve generalizability of findings.
- Incorporating 3D analytical and numerical coronal wave propagation models for more physics-based forecasting approaches.
- Modeling mechanisms for type III radio burst onset and time profiles using particle-in-cell and MHD models.
- Ensemble forecasting models for SEP events combining multiple machine learning algorithms trained on multi-mission data.
- Validation of data-driven models for other solar wind driven geospace extremes such as radiation belt enhancements and ionospheric storms.
- Leveraging new solar observatory missions and assimilative models within operational prediction systems for real-time space weather forecasts.
- Exploring applications of deep learning and physics-informed machine learning to additional outstanding problems in heliophysics and astrophysics.

In summary, the present work opens exciting avenues for more cross-disciplinary studies synthesizing heliophysics domain knowledge with cutting-edge data science and artificial intelligence methods. The new generation of solar, heliospheric and geospace missions will yield transformative observations to continue advancing both science understanding and predictive capabilities.

### 5.6 Definitions and Acronyms

Some of the key technical terms and acronyms used in this thesis are listed below:

- SEP - Solar Energetic Particle
- CME - Coronal Mass Ejection
- EUV - Extreme Ultraviolet
- SOHO - Solar and Heliospheric Observatory
- SDO - Solar Dynamics Observatory
- AIA - Atmospheric Imaging Assembly

EIT - Extreme ultraviolet Imaging Telescope

TRACE - Transition Region and Coronal Explorer

LASCO - Large Angle and Spectrometric COronagraph

GOES - Geostationary Operational Environmental Satellite

AI - Artificial Intelligence

MHD - Magnetohydrodynamics

AU - Astronomical Unit

This provides definitions of the major domain-specific terms and measurement concepts used. Additional terminology is introduced as required in the respective chapters.

# Appendix A

# Appendix

## A.1 Appendix for Radio Observation-related Work

### A.1.1 Persistent imaging technique

Persistent imaging is a technique used in medical imaging, particularly ultrasound imaging, to create a continuous, real-time display of the anatomy being imaged (see Pysz et al. 2011, and references within). The core idea of persistent imaging is to use persistence, or the ability of the human eye to retain an image for a brief moment after it has disappeared to create a more informative and visually clear image (Fredkin et al. 1995; Thompson & Young 2016).

At every image in a time-ordered series, the technique keeps the old pixel value if it is brighter than the current pixel value, else it takes the current pixel's value. The result is saved as the current persistence image. Then, the next image in the series is evaluated by comparing it pixel by pixel with respect to the previous persistence image. The resulting image emphasizes the changes between the current image and the previous persistent image, making them more visible to the human eye.

The persistent imaging technique can be described mathematically by a set of equations. If we let  $I(t, x, y)$  be the intensity at time  $t$  and pixel coordinates  $(x, y)$ , and let  $P(t, x, y)$  be the persistence image at time  $t$  and pixel coordinates  $(x, y)$ , then the persistence image at time  $t$  is computed as:

$$P(t, x, y) = \max\{I(t, x, y), P(t - 1, x, y)\}, \quad (\text{A.1})$$

where **max** represents the maximum of its two arguments. The current image at time  $t$  is then evaluated with respect to the previous persistence image as follows:

$$I'(t, x, y) = \max\{I(t, x, y) - P(t - 1, x, y), 0\}, \quad (\text{A.2})$$

The resulting image  $I'(t, x, y)$  is a modified version of the current image that emphasizes the differences from the previous persistence image.

The persistent imaging technique has been shown to improve the visual quality of ultrasound images and other medical imaging modalities, and is commonly used in clinical practice. In this paper, we utilize the persistent imaging technique to improve the visualization of the solar radio sources of type III emissions (Fig. 3.6).

### A.1.2 Resolving the radio emission location ambiguity

In this part, we show that the  $-Z$  solution of Equation 3.4 is highly unlikely in our case. Figure A.1 shows the positive and negative solutions of Equation 3.4. We take the innermost and outermost coronal radio sources at  $R_1$  and  $R_2$ , respectively, as an example.  $r_1$  and  $r_2$  are the projections of  $R_1$  and  $R_2$  on the POS, respectively. Harmonic radio emission from  $R_1$  will theoretically be absorbed by a region along the LOS with plasma frequency (and corresponding density) equal to or higher than the harmonic emission frequency at  $R_1$ . In the case of the spherically symmetric Newkirk model, the highest density location the emission from  $R_1$  could pass through is  $r_1$  on the POS. Thus, for harmonic radio emission from behind the POS ( $-Z$ , where  $Z = 0$  is defined at the center of the Sun and positive  $Z$  is towards the observer) to be observed at the Earth, it must satisfy the following condition:

$$2f_{R_1} > f_{r_1}, \quad (\text{A.3})$$

where  $f_{R_1}$  is the plasma frequency of radio emission that occurred behind the POS, and  $f_{r_1}$  is the plasma frequency at the projected location of  $r_1$  on the POS. The relation between the local plasma frequency and the electron density is defined by the equation:

$$f[\text{MHz}] = 8.93 \times 10^{-3} \sqrt{n[\text{cm}^{-3}]} \quad (\text{A.4})$$

The Newkirk electron-density model (Newkirk 1961, 1967) describes the typical densities in the outer part of the corona according to the following equation:

$$n[\text{cm}^{-3}] = \alpha 4.2 \times 10^4 10^{4.32 \frac{R_\odot}{r}} \quad (\text{A.5})$$

where  $\alpha$  is the fold number (i.e., a multiplicative factor that accounts for the density variations based on the degree of solar activity), and  $r$  is the radial distance from the Sun in solar radii. By substituting Equations A.4 and A.5 into Equation A.3, we obtain

$$\frac{n_{r_1}}{n_{R_1}} = \frac{10^{4.32 \frac{R_\odot}{r_1}}}{10^{4.32 \frac{R_\odot}{R_1}}} < 4. \quad (\text{A.6})$$

After reduction we obtain the final formula that must be satisfied under these assumptions in order for radio emission behind the POS to pass through the corona and reach the Earth:

$$\frac{r_1}{R_\odot} < \left( \frac{\log 2}{2.16} + \frac{R_\odot}{R_1} \right)^{-1}. \quad (\text{A.7})$$

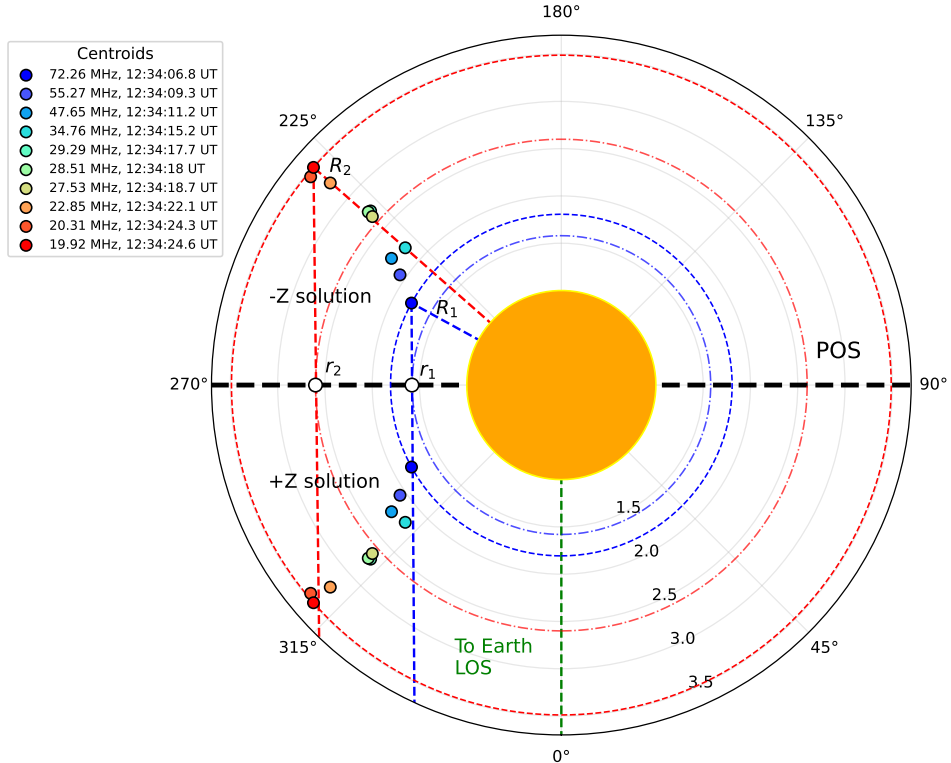


Figure A.1: Schematic shows the locations of the radio sources for the  $+Z$  and  $-Z$  solutions of Equation 3.4. The Sun is located in the middle as an orange circle, with a horizontal dashed black line representing the POS. The vertical dashed green line represents the Sun-Earth LOS. The dashed blue and red circles represent the plasma spheres of density equivalent to the observation frequencies of the innermost and outermost radio sources at  $R_1$  and  $R_2$ , respectively, under the Newkirk model assumption of spherically-symmetric density distribution. The impact parameters  $r_1$  and  $r_2$  are the projection of  $R_1$  and  $R_2$  on the POS. The dot-dashed blue and red circles are the circles passing through the impact parameters  $r_1$  and  $r_2$ , respectively.

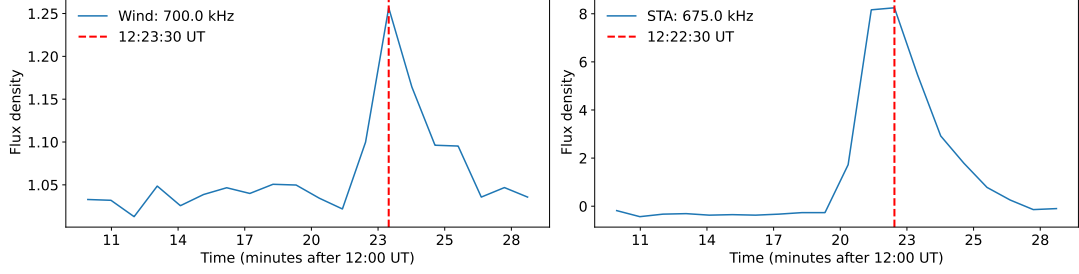


Figure A.2: Cut of the flux density at 700 kHz observed by Wind (left panel) and STEREO-A (right panel). Note: for STEREO-A, there is no exact frequency channel at 700 kHz; therefore we selected the nearest one (675 kHz).

From Figure A.1,  $r_1$  and  $r_2$  will always be smaller than  $R_1$  and  $R_2$ , respectively. The Newkirk model requires that the density at  $r_1$  and  $r_2$  be significantly higher than the density at  $R_1$  and  $R_2$ , respectively (Table A.1). Additionally, from the geometric representation in Figure A.1, we find that the electron density at  $r_1$  is higher than at  $R_1$ , hence the radio emission cannot reach the Earth from that point behind the POS (Mann, G. et al. 2018).

From Table A.1, the assumption of Equation A.6 is not satisfied. Thus, the  $-Z$  solution is invalid in our case. This implies that the harmonic emission from behind the POS will not reach the Earth. Thus, the  $+Z$  assumption is the valid solution.

Table A.1: Radial distances and densities at the first ( $R_1$ ) and last ( $R_2$ ) radio sources were obtained from the  $2.5 \times$  Newkirk model, as well as their impact parameters  $r_1$  and  $r_2$ , respectively.

| Point | Radial distance ( $R_\odot$ ) | Density ( $\text{cm}^{-3}$ ) | Ratio ( $n_r/n_R$ ) |
|-------|-------------------------------|------------------------------|---------------------|
| $r_1$ | 1.58                          | $5.69 \times 10^7$           |                     |
| $R_1$ | 1.81                          | $4.82 \times 10^6$           | 11.81               |
| $r_2$ | 2.6                           | $2.59 \times 10^7$           |                     |
| $R_2$ | 3.49                          | $1.82 \times 10^6$           | 14.23               |

Furthermore, we analyzed the time difference of arrival of the radio emission at interplanetary wavelengths in Figure A.2. Specifically, we compared the timing of peak signals at a low frequency between two spacecraft, Wind and STEREO. This analysis was conducted under the assumption of two possible scenarios:

- one in which the radio emission source follows a trajectory that is roughly equidistant between Wind and STEREO – if the  $+Z$  assumption is true.
- the trajectory implies significantly longer travel times from the source to Wind compared to STEREO – if the  $-Z$  assumption is true.

Examining the data, we selected the frequency channel 700 kHz observed by Wind and its nearest counterpart 675 kHz for STEREO. Interestingly, the difference in the arrival times of these signals was merely one minute, which is within the bounds of the time resolution of the instrument. This negligible difference in arrival times supports the  $+Z$  assumption for the beam trajectory, meaning it travels approximately at an equal distance between the two spacecraft.

## A.2 Appendix for SEP-related Work

### A.2.1 Terminologies

In this section, we introduce the main concepts related to machine learning which are presented in this paper.

- **Cross-validation:** A technique used to evaluate the performance of a machine learning model by dividing the data into subsets and assessing the model on different combinations of these subsets.

- **Input Horizon:** The number of previous time steps considered as input to a model for time series forecasting. It represents the length of the historical sequence used for predictions.
- **Batch Size:** The number of samples processed together in a single iteration of the training algorithm. It affects training speed and memory requirements.
- **Updating the Model's Weights:** The process of adjusting the parameters of a neural network based on training data to minimize the difference between predicted and true outputs. The model's weights represent the parameters that are learned during the training process.
- **Loss:** A function that quantifies the difference between predicted and actual outputs. It guides the optimization process during training.
- **Minimum Validation Loss:** The lowest value achieved by the loss function on a validation dataset during training. It indicates the most accurate predictions on unseen data.
- **Overfitting:** When a model performs well on training data but fails to generalize to unseen data due to memorizing training examples instead of learning underlying patterns.
- **Learning Rate:** A hyperparameter that determines the step size at each iteration of the optimization algorithm during training. It affects learning speed and convergence. A high learning rate can cause the training process to converge quickly, but it may also result in overshooting the optimal solution or getting stuck in a suboptimal solution. On the other hand, a very low learning rate can make the training process slow, and may struggle to find the optimal solution.
- **Reducing the learning rate when the validation loss stops improving:** This concept involves adjusting the learning rate dynamically during the training process. When the validation loss reaches a plateau or stops improving, it indicates a suboptimal point. By reducing the learning rate, the model can take smaller steps in weight space, potentially finding a better solution. This technique, known as learning rate scheduling or learning rate decay, is commonly used to fine-tune the model's performance.
- **Patience:** A parameter used in training to determine the number of epochs to wait for an improvement in validation loss before stopping the training process.
- **Patience Parameter of 7:** In the context of early stopping, training will be stopped if the validation loss does not improve for 7 consecutive epochs.
- **Adam Optimizer:** A popular optimization algorithm in deep learning that combines Adaptive Gradient Algorithm (AdaGrad) and Root Mean Square Propagation (RMSprop) to achieve efficient optimization.
- **Optimal Architecture:** The best configuration of a neural network, including the number of layers, neurons, and other choices, for optimal performance on a specific task.
- **Hyperparameters:** Parameters set before training a model that control the learning algorithm's behavior, such as learning rate, batch size, and activation functions.
- **Layer:** A building block of a neural network that performs specific operations on input data. Includes input, hidden, output, fully connected, convolutional, recurrent, activation, and dropout layers. Here is a description for each layer:
  - **Input Layer:** The first layer of a neural network that receives raw input data. It passes the input to subsequent layers for further processing. The number of nodes in the input layer is determined by the dimensionality of the input data.
  - **Hidden Layers:** Intermediate layers between the input and output layers. They perform computations on the input data and capture higher-level representations or abstractions. Hidden layers are not directly exposed to the input or output.
  - **Output Layer:** The final layer of a neural network that produces model predictions or outputs based on computations from preceding layers. The number of neurons in the output layer depends on the problem being solved, such as regression or classification.

- **Fully Connected Layer (Dense Layer):** Each neuron in this layer is connected to every neuron in the previous layer. It allows information flow between all neurons, enabling complex relationships to be learned.
- **Convolutional Layer:** Commonly used in Convolutional Neural Networks (CNNs) for analyzing grid-like data, such as images. It applies convolution operations using filters or kernels to learn spatial patterns or features.
- **Recurrent Layer:** Used in Recurrent Neural Networks (RNNs) to process sequential data. These layers have feedback connections that allow information to be passed from one step to the next, capturing temporal dependencies and maintaining memory of past inputs.
- **Activation Layer:** Applies a non-linear function to the output of a layer, introducing non-linearity into the neural network. Activation functions like Sigmoid, Hyperbolic Tangent ( $\tanh$ ), or Rectified Linear Unit (ReLU) determine neuron outputs based on weighted inputs.
- **Dropout Layer:** A regularization technique commonly used in deep learning models. It randomly sets a fraction of outputs from the previous layer to zero during training, preventing overfitting and improving generalization.

Layers play a crucial role in the information processing and learning capabilities of neural networks. The arrangement and combination of different layers determine the network's architecture and ultimately its ability to solve specific tasks.

- **Stateful:** A property of Recurrent Neural Networks (RNNs) where the hidden state is preserved between consecutive inputs, allowing the network to have memory.
- **Neuron:** A computational unit in a neural network that receives input, applies weights, and passes the result through an activation function to produce an output.
- **Hidden Neuron:** A neuron in a hidden layer of a neural network that performs intermediate computations.
- **Callback Function:** A function used during model training to perform specific actions at certain points or conditions, such as saving the best model, adjusting learning rates, or early stopping.
- **LearningRateScheduler Callback Function:** A function used in training to dynamically adjust the learning rate at specific points based on a predefined schedule or function. It improves training efficiency and convergence by allowing the model to make finer adjustments as it approaches the optimal solution.

### A.2.2 Mathematical Representation of the LSTM NN Model

The computations inside one LSTM cell can be described by the following formulas (Ihianle et al. 2020):

$$f_t = \sigma(W_f x_t + U_f h_{t-1} + b_f) \quad (\text{A.8a})$$

$$i_t = \sigma(W_i x_t + U_i h_{t-1} + b_i) \quad (\text{A.8b})$$

$$\tilde{C}_t = \tanh(W_c x_t + U_c h_{t-1} + b_c) \quad (\text{A.8c})$$

$$C_t = f_t \odot C_{t-1} + i_t \odot \tilde{C}_t \quad (\text{A.8d})$$

$$o_t = \sigma(W_o x_t + U_o h_{t-1} + b_o) \quad (\text{A.8e})$$

$$h_t = o_t \odot \tanh(C_t) \quad (\text{A.8f})$$

where  $x_t$  is input data at time  $t$ . The input gate  $i_t$  determines which values from the updated cell states (candidate values)  $\tilde{C}_t$  should be added to the cell state. It also takes into account the current input  $x_t$  and the previous output  $h_{t-1}$ , and is passed through a sigmoid activation function.  $\tilde{C}_t$  represent the candidate values that are added to the cell state at time  $t$ . The forget gate activation vector  $f_t$  at time step  $t$ , which determines how much of the previous cell state should be retained. The cell state  $C_t$  at time  $t$  is updated based on the forget gate, input gate, and candidate values. The output gate  $o_t$  at time  $t$  determines how much of the cell state should be output. The output vector  $h_t$  at time  $t$  is calculated based on the cell state and the output gate values.  $h_{t-1}$  is the output vector at the previous time step  $t - 1$ .  $W_f, W_i, W_c, W_o$  are the weight matrices for the input vector  $x_t$ .  $U_f, U_i, U_c, U_o$  are the weight

matrices for the output vector  $h_{t-1}$ .  $b_f, b_i, b_c, b_o$  are the bias vectors. The symbol  $\odot$  denotes a pointwise multiplication. The sigmoid function  $\sigma$  is used as the activation function for the gate vectors, and the hyperbolic tangent function  $\tanh$  is used for the candidate values and the output vector.

### A.2.3 Evaluation Metrics

To evaluate the model performance, we used the following equations:

$$L_\delta(y, \hat{y}) = \begin{cases} \frac{1}{2}(y - \hat{y})^2, & \text{if } |y - \hat{y}| \leq \delta, \\ \delta(|y - \hat{y}| - \frac{1}{2}\delta), & \text{otherwise} \end{cases} \quad (\text{A.9a})$$

$$MSE = \frac{1}{N} \sum_{i=1}^N (y_i - \hat{y}_i)^2 \quad (\text{A.9b})$$

$$MAE = \frac{1}{N} \sum_{i=1}^N |y_i - \hat{y}_i| \quad (\text{A.9c})$$

$$RMSE = \sqrt{\frac{\sum_{i=1}^N (y_i - \hat{y}_i)^2}{N}} \quad (\text{A.9d})$$

$$MAPE = \frac{1}{N} \sum_{i=1}^N \left| \frac{y_i - \hat{y}_i}{\hat{y}_i} \right| \quad (\text{A.9e})$$

$$R = \frac{\sum_{i=1}^n (y_i - \bar{y})(\hat{y}_i - \bar{\hat{y}})}{\sqrt{\sum_{i=1}^n (y_i - \bar{y})^2} \sqrt{\sum_{i=1}^n (\hat{y}_i - \bar{\hat{y}})^2}} \quad (\text{A.9f})$$

where  $y$  is the true value,  $\hat{y}$  is the predicted value, and  $\delta$  is a threshold in the Huber loss function that controls the trade-off between the mean squared error (MSE) and the mean absolute error (MAE). In this paper, it was set to 0.1, which was selected based on several experiments.

MSE is the mean squared error, which measures the difference between predicted and actual values by calculating the average of squared differences. It provides a measure of the average squared magnitude of the errors in your forecasts, which can be useful in penalizing larger errors more heavily than smaller errors.

MAPE is the mean absolute percentage error, which measures the difference between predicted and actual values by calculating the average of absolute differences. It provides a measure of the average magnitude of the errors, allowing to evaluate the overall accuracy of your forecasts.

RMSE is the root mean squared error, which measures the difference between predicted and actual values by taking the square root of the average of squared differences. It provides a measure of the accuracy of the forecasts in the same units as the original data, allowing to evaluate the magnitude of errors in the same scale as the data.

MAPE is the mean absolute percentage error, which measures the accuracy of a forecast by calculating the average of absolute percentage errors. It provides a measure of the accuracy of the forecasts in percentage terms, allowing to evaluate the magnitude of errors relative to the actual values. MSE, MAE, RMSE, and MAPE are often used in regression analysis to assess the accuracy of the model's predictions.

Finally,  $R$  is the Pearson correlation coefficient, which measures the strength and direction of the relationship between two continuous variables, and can provide an indication of the extent to which changes in one variable may be related to changes in the other.

### A.2.4 Model Configuration

The configurations for the ML models shown in Figure 4.5 and their performance on the validation set and the test set for the SEP integral flux  $\geq 10$  MeV are presented in Table A.2. The batch size was set to be 64 and the number of training epochs was set to be 100. The *EarlyStopping* callback function, with a *patience* of 10, is used to help prevent overfitting during the training process by stopping training when the monitored metric has stopped improving for a certain number of epochs. The *patience* parameter controls how many epochs the training will continue without improvement before it is stopped. This is useful because if the validation loss stops getting better, the model has probably overfitted the training data and is not generalizing effectively to new data. By stopping the training early, we can avoid wasting time and resources on further training that is unlikely to improve the model's performance.

We used the *ModelCheckpoint* callback function to save the best weights of the model during training so that they can be reused later. The *LearningRateScheduler* callback function allows to dynamically adjust the learning rate of the model during training using a function passed to it that will be called at the beginning of each epoch, and it should return the desired learning rate for that epoch. It can be useful when training deep neural networks, as it allows for a higher learning rate in the early stages of training when the model is still far from convergence, and a lower learning rate as the model approaches convergence, which can help it to converge more accurately. The downside might be the longer training time.

Table A.2: Configuration of the ML model. (1) refers to the error value for 1-day forecasting. Same for (2) refers to 2-day forecasting, and (3) for 3-day forecasting. \*In the 1D-CNN layer, 32 filters, a kernel size of 5, and strides of 1 were used.

| Model Architecture | No. of Hidden Layers | No. of Hidden Neurons | Activation Function | Batch Size | Learning Rate       | Epochs | Callbacks Functions                    | Validation Set                      |                                     |                                     |   | Testing Set                         |                                     |                                     |   |
|--------------------|----------------------|-----------------------|---------------------|------------|---------------------|--------|--|-------------------------------------|-------------------------------------|-------------------------------------|---|-------------------------------------|-------------------------------------|-------------------------------------|---|
|                    |                      |                       |                     |            |                     |        |  | MAE                                 | MSE                                 | RMSE                                | MAPE                                      | MAE                                 | MSE                                 | RMSE                                | MAPE                                      |
| Linear             | —                    | —                     | —                   | 64         | 0.001               | 100    | EarlyStopping                          | 0.312                               | 0.141                               | 0.376                               | 87.883                                    | 0.143                               | 0.045                               | 0.211                               | 60.689                                    |
| Dense ML           | 2                    | 32                    | ReLU                | 64         | 0.001               | 100    | EarlyStopping                          | 0.262 (1)<br>0.275 (2)<br>0.290 (3) | 0.118 (1)<br>0.138 (2)<br>0.166 (3) | 0.344 (1)<br>0.372 (2)<br>0.407 (3) | 132.580 (1)<br>132.004 (2)<br>129.288 (3) | 0.400 (1)<br>0.395 (2)<br>0.392 (3) | 0.281 (1)<br>0.286 (2)<br>0.294 (3) | 0.530 (1)<br>0.535 (2)<br>0.542 (3) | 238.898 (1)<br>234.704 (2)<br>230.896 (3) |
| Simple RNN         | 2                    | 32                    | Tanh                | 64         | 0.001               | 100    | EarlyStopping<br>ModelCheckpoint       | 0.143 (1)<br>0.171 (2)<br>0.264 (3) | 0.035 (1)<br>0.063 (2)<br>0.118 (3) | 0.187 (1)<br>0.251 (2)<br>0.343 (3) | 70.799 (1)<br>68.693 (2)<br>72.505 (3)    | 0.178 (1)<br>0.217 (2)<br>0.200 (3) | 0.052 (1)<br>0.071 (2)<br>0.084 (3) | 0.228 (1)<br>0.262 (2)<br>0.283 (3) | 69.624 (1)<br>78.075 (2)<br>67.416 (3)    |
| Stateful RNN       | 3                    | 32                    | Tanh                | 64         | 1.58e <sup>-4</sup> | 100    | LearningRateScheduler<br>EarlyStopping | 0.203 (1)<br>0.305 (2)<br>0.349 (3) | 0.060 (1)<br>0.131 (2)<br>0.173 (3) | 0.244 (1)<br>0.362 (2)<br>0.416 (3) | 56.390 (1)<br>81.028 (2)<br>82.819 (3)    | 0.155 (1)<br>0.223 (2)<br>0.223 (3) | 0.039 (1)<br>0.079 (2)<br>0.084 (3) | 0.197 (1)<br>0.281 (2)<br>0.289 (3) | 59.988 (1)<br>71.679 (2)<br>64.159 (3)    |
| Stateful LSTM      | 3                    | 32                    | Tanh                | 64         | 1.58e <sup>-4</sup> | 100    | EarlyStopping                          | 0.095 (1)<br>0.151 (2)<br>0.174 (3) | 0.021 (1)<br>0.048 (2)<br>0.076 (3) | 0.146 (1)<br>0.220 (2)<br>0.275 (3) | 40.335 (1)<br>48.937 (2)<br>55.662 (3)    | 0.098 (1)<br>0.134 (2)<br>0.166 (3) | 0.020 (1)<br>0.042 (2)<br>0.071 (3) | 0.141 (1)<br>0.205 (2)<br>0.267 (3) | 41.781 (1)<br>57.860 (2)<br>68.025 (3)    |
| Stateful Bi-LSTM   | 3                    | 32                    | Tanh                | 64         | 1.58e <sup>-4</sup> | 100    | EarlyStopping                          | 0.149 (1)<br>0.190 (2)<br>0.249 (3) | 0.043 (1)<br>0.074 (2)<br>0.120 (3) | 0.207 (1)<br>0.272 (2)<br>0.347 (3) | 58.150 (1)<br>60.154 (2)<br>67.983 (3)    | 0.170 (1)<br>0.211 (2)<br>0.229 (3) | 0.049 (1)<br>0.090 (2)<br>0.108 (3) | 0.221 (1)<br>0.300 (2)<br>0.329 (3) | 71.059 (1)<br>92.727 (2)<br>87.049 (3)    |
| 1D-CNN LSTM        | 3                    | 32 (5,1)*             | ReLU<br>Tanh        | 64         | 1.58e <sup>-4</sup> | 100    | EarlyStopping                          | 0.108 (1)<br>0.146 (2)<br>0.177 (3) | 0.027 (1)<br>0.051 (2)<br>0.078 (3) | 0.165 (1)<br>0.226 (2)<br>0.279 (3) | 41.164 (1)<br>47.512 (2)<br>53.087 (3)    | 0.098 (1)<br>0.138 (2)<br>0.156 (3) | 0.023 (1)<br>0.047 (2)<br>0.067 (3) | 0.151 (1)<br>0.217 (2)<br>0.259 (3) | 51.732 (1)<br>68.376 (2)<br>69.338 (3)    |

All the calculations and model runs were implemented under the framework of TensorFlow 2.3.0 (Singh et al. 2020) in Python 3.6.13. The models were executed on Ubuntu 20.04.1 LTS OS with 4 × GPUs (NVIDIA GeForce RTX 2080 Ti, 11019 MiB, 300 MHz). According to the Keras API guide (Ketkar & Ketkar 2017), the requirements to use the cuDNN implementation are the activation function must be set to *tanh* and the recurrent activation must be set to *sigmoid*. We also set the seed number to 7 across all the model runs to maintain reproducibility.

Stateful RNNs can be difficult to work with when using callbacks in Keras because their hidden state must be manually managed across mini-batch updates. When training a stateful RNN in Keras, the hidden state is carried over from the previous epoch and can cause problems with certain callbacks, such as *EarlyStopping* or *ModelCheckpoint*. To work around this issue, one can use stateless RNNs or manually reset the hidden state at the end of each epoch, but this can be complex and prone to errors.

### A.2.5 Skill Scores

Skill scores and ratios are commonly used in evaluating the performance of classification models, particularly in binary classification tasks. They provide insights into the model’s ability to correctly predict positive and negative instances. Here is a brief description of each skill score and ratio, along with their formulas:

- **True Positive (TP):** The number of data points or intervals correctly identified as positive by the model. It represents instances where both the model and the ground truth indicate the presence of an event.
- **True Negative (TN):** The number of intervals correctly identified as negative by the model. It represents instances where both the model and the ground truth indicate the absence of an event.
- **False Positive (FP):** The number of intervals incorrectly identified as positive by the model. It occurs when the model predicts an event, but the ground truth indicates its absence.
- **False Negative (FN):** The number of intervals incorrectly identified as negative by the model. It occurs when the model fails to detect an event that the ground truth indicates its presence.
- **Accuracy:** Represents the proportion of correct predictions out of total predictions.

$$\text{Accuracy} = \frac{TP + TN}{TP + TN + FP + FN} \quad (\text{A.10})$$

- **Precision:** Represents the proportion of positive predictions that are actually positive.

$$Precision = \frac{TP}{TP + FP} \quad (\text{A.11})$$

- **Probability of Detection (POD) or Recall:** Represents the model's ability to correctly identify positive instances.

$$POD = \frac{TP}{TP + FN} \quad (\text{A.12})$$

- **Probability of False Detection (POFD):** Measures the model's tendency to falsely predict positive instances when the ground truth indicates their absence.

$$POFD = \frac{FP}{FP + TN} \quad (\text{A.13})$$

- **False Alarm Rate (FAR):** Indicates the ratio of false positive predictions to the total number of positive instances.

$$FAR = \frac{FP}{TP + FP} \quad (\text{A.14})$$

- **Critical Success Index (CSI):** Measures the model's ability to correctly predict both positive and negative instances.

$$CSI = \frac{TP}{TP + FP + FN} \quad (\text{A.15})$$

- **True Skill Statistic (TSS):** Takes into account both the model's ability to detect positive instances and its ability to avoid false alarms.

$$TSS = POD - FAR \quad (\text{A.16})$$

- **Heidke Skill Score (HSS):** Evaluates the model's performance by comparing it with random chance. It takes into account the agreement between the model's predictions and the observed data, considering both true positive and true negative predictions.

$$HSS = \frac{TP + TN - C}{T - C} \quad (\text{A.17})$$

where

$$T = TP + TN + FP + FN$$

$$C = \frac{(TP + FP)(TP + FN) + (TN + FP)(TN + FN)}{T}$$

# Bibliography

- 2017, Nature Astronomy, 1, 771
- Akansu, A. N. 1991, Optical Engineering, 30, 912
- Akasofu, S. I. 1981, Space Science Reviews, 28, 121
- Alharbi, F. R. & Csala, D. 2021, in 2021 International Conference on Electrical, Communication, and Computer Engineering (ICECCE), IEEE, 1–6
- Alielden, K. & Taroyan, Y. 2022, The Astrophysical Journal, 935, 66
- Altschuler, M. D. & Newkirk, G. 1969, Solar Physics, 9, 131
- Amari, T., Canou, A., & Aly, J.-J. 2014, Nature, 514, 465
- Aminalragia-Giamini, S., Raptis, S., Anastasiadis, A., et al. 2021, Journal of Space Weather and Space Climate, 11, 59
- Aran, A., Sanahuja, B., & Lario, D. 2006, Advances in Space Research, 37, 1240
- Aschwanden, M. J. 2002, Space Science Reviews, 101, 1
- Aschwanden, M. J. 2010, Solar Physics, 262, 235
- Badman, S. T., Carley, E., Cañizares, L. A., et al. 2022, The Astrophysical Journal, 938, 95
- Bale, S., Goetz, K., Harvey, P., et al. 2016, Space science reviews, 204, 49
- Bein, B. M., Berkebile-Stoiser, S., Veronig, A. M., et al. 2011, apj, 738, 191
- Benson, B., Pan, W. D., Prasad, A., Gary, G. A., & Hu, Q. 2020, Solar Physics, 295, 65
- Benz, A. & Thejappa, G. 1988
- Benz, A. O. 2017, Living reviews in solar physics, 14, 1
- Berghmans, D., Auchère, F., Long, D. M., et al. 2021, Astronomy & Astrophysics, 656, L4
- Biesecker, D., Myers, D., Thompson, B., Hammer, D., & Vourlidas, A. 2002, The Astrophysical Journal, 569, 1009
- Bonnin, X., Hoang, S., & Maksimovic, M. 2008, Astron. Astrophys., 489, 419
- Borovsky, J. E. & Denton, M. H. 2006, Journal of Geophysical Research: Space Physics, 111
- Boudjada, M. Y., Abou el Fadl, A., Galopeau, P. H., Al-Haddad, E., & Lammer, H. 2020, Advances in Radio Science, 18, 83
- Brewer, D. A., Barth, J. L., Label, K. A., Kauffman, W. J., & Giffin, G. 2002, Acta Astronautica, 51, 609
- Bruno, A. & Richardson, I. G. 2021, Solar Physics, 296, 36
- Camporeale, E. 2019, Space weather, 17, 1166

- Cane, H. V., Erickson, W., & Prestage, N. 2002, Journal of Geophysical Research: Space Physics, 107, SSH
- Cattell, C., Glesener, L., Leiran, B., et al. 2021, Astron. Astrophys., 650, A6
- Che, H. 2018, Journal of Physics: Conference Series, 1100, 012005
- Chen, N., Ip, W.-H., & Innes, D. 2013, The Astrophysical Journal, 769, 96
- Chen, P. 2016, Low-Frequency Waves in Space Plasmas, 379
- Chen, P. F., Wu, S. T., Shibata, K., & Fang, C. 2002, The Astrophysical Journal, 572, L99
- Chen, X., Kontar, E. P., Chrysaphi, N., et al. 2023, arXiv e-prints, arXiv:2306.09160
- Chhabra, S., Klimchuk, J. A., & Gary, D. E. 2021, The Astrophysical Journal, 922, 128
- Cohen, C. & Mewaldt, R. 2018, Space Weather, 16, 1616
- Curto, J. J., Blanca, M., & Martínez, E. 2008, Solar Physics, 250, 411
- Dabrowski, B., Flisek, P., Mikula, K., et al. 2021, Remote Sensing, 13, 148
- Dalla, S., Swalwell, B., Battarbee, M., et al. 2017in (Cambridge University Press), 268–271
- Debrunner, H., Flückiger, E., Grädel, H., Lockwood, J., & McGuire, R. 1988, Journal of Geophysical Research: Space Physics, 93, 7206
- Del Zanna, G., Aulanier, G., Klein, K.-L., & Török, T. 2011, Astronomy & Astrophysics, 526, A137
- Delannée, C. & Aulanier, G. 1999, Solar Physics, 190, 107
- Desai, M. & Giacalone, J. 2016, Living Reviews in Solar Physics, 13, 3
- Dierckxsens, M., Tziotziou, K., Dalla, S., et al. 2015, Solar Physics, 290, 841
- Dulk, G., Steinberg, J.-L., Lecacheux, A., Hoang, S., & MacDowall, R. J. 1985, Astronomy and Astrophysics, 150, L28
- Dumbović, M., Veronig, A., Podladchikova, T., et al. 2021, Astronomy & Astrophysics, 652, A159
- Dungey, J. 1961, Journal of Geophysical Research, 66, 1043
- Eastwood, J., Nakamura, R., Turc, L., Mejnertsen, L., & Hesse, M. 2017, Space Science Reviews, 212, 1221
- Echer, E. & Gonzalez, W. 2022, Advances in Space Research, 70, 2830
- Engell, A., Falconer, D., Schuh, M., Loomis, J., & Bissett, D. 2017, Space Weather, 15, 1321
- Ergun, R., Larson, D., Lin, R., et al. 1998, The Astrophysical Journal, 503, 435
- Feynman, J., Armstrong, T., Dao-Gibner, L., & Silverman, S. 1990, Solar Physics, 126, 385
- Fletcher, L., Dennis, B. R., Hudson, H. S., et al. 2011, Space science reviews, 159, 19
- Florios, K., Kontogiannis, I., Park, S.-H., et al. 2018, Solar Physics, 293, 28
- Fox, N., Velli, M., Bale, S., et al. 2016, Space Science Reviews, 204, 7
- Fredkin, D. R., Rice, J. A., Colquhoun, D., & Gibb, A. 1995, Philosophical Transactions of the Royal Society of London. Series B: Biological Sciences, 350, 353
- Gabriel, S., Evans, R., & Feynman, J. 1990, Solar physics, 128, 415
- Gieseler, J., Dresing, N., Palmroos, C., et al. 2023, Frontiers in Astronomy and Space Sciences, 9, 384
- Gonzalez, W., Joselyn, J.-A., Kamide, Y., et al. 1994, Journal of Geophysical Research: Space Physics, 99, 5771

- Goodfellow, I., Bengio, Y., & Courville, A. 2016, Deep learning (MIT press)
- Gopalswamy, N. 2022, *Atmosphere*, 13, 1781
- Gopalswamy, N., Mäkelä, P., Yashiro, S., et al. 2017in , IOP Publishing, 012009
- Gopalswamy, N., Mäkelä, P., Yashiro, S., Akiyama, S., & Xie, H. 2022, in 2022 3rd URSI Atlantic and Asia Pacific Radio Science Meeting (AT-AP-RASC), 1–4
- Gopalswamy, N. & Yashiro, S. 2011, *apjl*, 736, L17
- Graves, A. & Jaitly, N. 2014in (Beijing, China: PMLR), 1764–1772
- Graves, A. & Schmidhuber, J. 2005, *Neural networks*, 18, 602
- Greff, K., Srivastava, R. K., Koutnřík, J., Steunebrink, B. R., & Schmidhuber, J. 2016, *IEEE transactions on neural networks and learning systems*, 28, 2222
- Guo, F. & Giacalone, J. 2013, *The Astrophysical Journal*, 773, 158
- Gurnett, D. A. & Anderson, R. R. 1976, *Science*, 194, 1159
- Gurnett, D. A. & Anderson, R. R. 1977, *Journal of Geophysical Research*, 82, 632
- Hale, G. E., Ellerman, F., Nicholson, S. B., & Joy, A. H. 1919, *Astrophys. J.*, 49, 153
- Harra, L., Brooks, D. H., Bale, S. D., et al. 2021, *Astronomy & Astrophysics*, 650, A7
- Harvey, J. W., Hill, F., Hubbard, R. P., et al. 1996, *Science*, 272, 1284
- Hochreiter, S. & Schmidhuber, J. 1997, *Neural computation*, 9, 1735
- Holman, G. D., Aschwanden, M. J., Aurass, H., et al. 2011, *Space science reviews*, 159, 107
- Holschneider, M., Kronland-Martinet, R., Morlet, J., & Tchamitchian, P. 1989, in *Wavelets. Time-Frequency Methods and Phase Space*, ed. J.-M. Combes, A. Grossmann, & P. Tchamitchian (Springer-Verlag), 286
- Hu, J., Li, G., Ao, X., Zank, G. P., & Verkhoglyadova, O. 2017, *Journal of Geophysical Research: Space Physics*, 122, 10
- Huang, X., Tan, H., Lin, G., & Tian, Y. 2018, 2018 International Conference on Artificial Intelligence and Big Data (ICAIBD), 185
- Ihianle, I. K., Nwajana, A. O., Ebenuwa, S. H., et al. 2020, *IEEE Access*, 8, 179028
- Ireland, J., Inglis, A. R., Shih, A. Y., et al. 2019, *Solar Physics*, 294, 158
- Jackson, B., Hick, P., Buffington, A., et al. 2010in , American Institute of Physics, 659–662
- Jang, S., Moon, Y.-J., Kim, R.-S., Lee, H., & Cho, K.-S. 2016, *The Astrophysical Journal*, 821, 95
- Kahler, S., Cliver, E., Cane, H., et al. 1987, in *Proceedings of the 20<sup>th</sup> International Cosmic Ray Conference Moscow*, Volume 3, p. 121
- Kahler, S., Kazachenko, M., Lynch, B., & Welsch, B. 2017in , IOP Publishing, 012011
- Kahler, S., Sheeley Jr, N., Howard, R., et al. 1984, *Journal of Geophysical Research: Space Physics*, 89, 9683
- Kahler, S. W., Cliver, E. W., & Ling, A. G. 2007, *Journal of Atmospheric and Solar-Terrestrial Physics*, 69, 43
- Kane, R. 2011, *Indian Journal of Radio & Space Physics*, 40, 7
- Kasapis, S., Zhao, L., Chen, Y., et al. 2022, *Space Weather*, 20, e2021SW002842
- Kay, C. & Gopalswamy, N. 2018, *Journal of Geophysical Research: Space Physics*, 123, 7220

- Ketkar, N. & Ketkar, N. 2017, Deep learning with python: a hands-on introduction, 97
- Kim, T., Park, E., Lee, H., et al. 2019, Nature Astronomy, 3, 397
- Kingma, D. P. & Ba, J. 2015, International Conference on Learning Representations (ICLR), San Diego
- Klassen, A., Karlický, M., & Mann, G. 2003a, *Astronomy & Astrophysics*, 410, 307
- Klassen, A., Pohjolainen, S., & Klein, K.-L. 2003b, *Solar Physics*, 218, 197
- Klein, K.-L. & Dalla, S. 2017, *Space Science Reviews*, 212, 1107
- Kolen, J. F. & Kremer, S. C. 2001, Gradient Flow in Recurrent Nets: The Difficulty of Learning LongTerm Dependencies (IEEE), 237–243
- Kong, D., Pan, G., Yan, X., Wang, J., & Li, Q. 2018, *The Astrophysical Journal Letters*, 863, L22
- Kontar, E. P., Chen, X., Chrysaphi, N., et al. 2019, *The Astrophysical Journal*, 884, 122
- Kontar, E. P., Emslie, A. G., Clarkson, D. L., et al. 2023, arXiv preprint arXiv:2308.05839
- Kontar, E. P., Yu, S., Kuznetsov, A., et al. 2017, *Nature communications*, 8, 1515
- Kóta, J., Manchester, W., Jokipii, J., De Zeeuw, D., & Gombosi, T. 2005in , American Institute of Physics, 201–206
- Kouloumvakos, A., Rodríguez-García, L., Gieseler, J., et al. 2022, *Frontiers in Astronomy and Space Sciences*, 9, 974137
- Kozarev, K., Nedal, M., Miteva, R., Dechev, M., & Zucca, P. 2022, *Frontiers in Astronomy and Space Sciences*, 9, 34
- Kozarev, K. A., Davey, A., Kendrick, A., Hammer, M., & Keith, C. 2017, *Journal of Space Weather and Space Climate*, 7, A32
- Kozarev, K. A., Dayeh, M. A., & Farahat, A. 2019, *The Astrophysical Journal*, 871, 65
- Kozarev, K. A., Evans, R. M., Schwadron, N. A., et al. 2013, *The Astrophysical Journal*, 778, 43
- Kozarev, K. A., Korreck, K. E., Lobzin, V. V., Weber, M. A., & Schwadron, N. A. 2011, *The Astrophysical Journal*, 733, L25
- Kozarev, K. A., Raymond, J. C., Lobzin, V. V., & Hammer, M. 2015, *The Astrophysical Journal*, 799, 167
- Kozarev, K. A. & Schwadron, N. A. 2016, *apj*, 831, 120
- Krucker, S., Hudson, H. S., Jeffrey, N. L. S., et al. 2011, *The Astrophysical Journal*, 739, 96
- Krupar, V., Szabo, A., Maksimovic, M., et al. 2020, *Astrophys. J. Suppl.*, 246, 57
- Kwon, R.-Y., Zhang, J., & Olmedo, O. 2014, *The Astrophysical Journal*, 794, 148
- Laitinen, T. & Dalla, S. 2017, *The Astrophysical Journal*, 834, 127
- Lakhina, G. S. & Tsurutani, B. T. 2016, *Geoscience Letters*, 3, 1
- Lanzerotti, L. J. 2001, Washington DC American Geophysical Union Geophysical Monograph Series, 125, 11
- Laurenza, M., Cliver, E., Hewitt, J., et al. 2009, *Space Weather*, 7
- Lavasa, E., Giannopoulos, G., Papaioannou, A., et al. 2021, *Solar Physics*, 296, 107
- Le, G.-M. & Zhang, X.-F. 2017, *Research in Astronomy and Astrophysics*, 17, 123
- Lecacheux, A., Steinberg, J. L., Hoang, S., & Dulk, G. A. 1989, *Astron. Astrophys.*, 217, 237
- Lemen, J. R., Title, A. M., Akin, D. J., et al. 2012, *Solar Physics*, 275, 17

- Li, B. & Cairns, I. H. 2012, *The Astrophysical Journal*, 753, 124
- Li, G., Shalchi, A., Ao, X., Zank, G., & Verkhoglyadova, O. 2012, *Advances in Space Research*, 49, 1067
- Li, G., Zank, G., & Rice, W. 2003, *Journal of Geophysical Research: Space Physics*, 108
- Li, R. & Zhu, J. 2013, *Research in Astronomy and Astrophysics*, 13, 1118
- Lilensten, J., Coates, A. J., Dehant, V., et al. 2014, *The Astronomy and Astrophysics Review*, 22, 1
- Lin, R. 2005, *Advances in Space Research*, 35, 1857
- Lin, R. 2011, *Space science reviews*, 159, 421
- Liu, W. & Ofman, L. 2014, *Solar Physics*, 289, 3233
- Long, D. M., Bloomfield, D. S., Chen, P.-F., et al. 2017, *Solar physics*, 292, 1
- Long, D. M., Bloomfield, D. S., Gallagher, P. T., & Pérez-Suárez, D. 2014, *Solar Physics*, 289, 3279
- Long, D. M., DeLuca, E. E., & Gallagher, P. T. 2011, *apjl*, 741, L21
- Ma, S., Raymond, J. C., Golub, L., et al. 2011, *The Astrophysical Journal*, 738, 160
- MacDowall, R., Lara, A., Manoharan, P., et al. 2003, *Geophysical research letters*, 30
- Madjarska, M. S. 2019, *Living Reviews in Solar Physics*, 16, 2
- Magdalenić, J., Marqué, C., Zhukov, A. N., Vršnak, B., & Žic, T. 2010, *Astrophys. J.*, 718, 266
- Malandraki, O. E. & Crosby, N. B. 2018, Solar particle radiation storms forecasting and analysis: the HESPERIA HORIZON 2020 project and beyond
- Mann, G., Breitling, F., Vocks, C., et al. 2018, *A&A*, 611, A57
- Melrose, D. 1980, *Space Science Reviews*, 26, 3
- Melrose, D. 2017, *Reviews of Modern Plasma Physics*, 1, 1
- Mierla, M., Inhester, B., Antunes, A., et al. 2010in , Copernicus GmbH, 203–215
- Mikić, Z., Linker, J. A., Schnack, D. D., Lionello, R., & Tarditi, A. 1999, *Physics of Plasmas*, 6, 2217
- Miteva, R., Klein, K.-L., Malandraki, O., & Dorrian, G. 2013, *Solar Physics*, 282, 579
- Miteva, R., Nedal, M., Samwel, S. W., & Temmer, M. 2023, *Universe*, 9, 179
- Moore, R. L., Sterling, A. C., Hudson, H. S., & Lemen, J. R. 2001, *The Astrophysical Journal*, 552, 833
- Morosan, D. E. & Gallagher, P. T. 2017, in *Planetary Radio Emissions VIII*, ed. G. Fischer, G. Mann, M. Panchenko, & P. Zarka, 357–368
- Morton, R., Tomczyk, S., & Pinto, R. 2015, *Nature Communications*, 6, 7813
- Muhr, N., Veronig, A. M., Kienreich, I. W., et al. 2014, *Solar Physics*, 289, 4563
- Nammous, M. K., Saeed, K., & Kobojeck, P. 2022, *Journal of King Saud University - Computer and Information Sciences*, 34, 764
- Nedal, M., Kozarev, K., Zhang, P., & Pietro, Z. 2023, *A&A*, 680, A106
- Nedal, M., Mahrous, A., & Youssef, M. 2019, *Astrophysics and Space Science*, 364, 161
- Newkirk, G. 1967, *Annual Review of Astronomy and Astrophysics*, 5, 213
- Newkirk, Gordon, J. 1961, *Astrophys. J.*, 133, 983
- Ng, C. K., Reames, D. V., & Tylka, A. J. 2012in , American Institute of Physics, 212–218
- Nindos, A., Aurass, H., Klein, K. L., & Trottet, G. 2008, *Sol. Phys.*, 253, 3

- Nitta, N. V., Schrijver, C. J., Liu, W., et al. 2013, *The Astrophysical Journal*, 776, 58
- Nymmk, R. 2007, *Advances in Space Research*, 40, 321
- Núñez, M. 2011, *Space Weather*, 9
- Odstrcil, D., Riley, P., & Zhao, X. 2004, *Journal of Geophysical Research: Space Physics*, 109
- Offringa, A. R., McKinley, B., Hurley-Walker, N., et al. 2014, *Mon. Not. R. Astron. Soc.*, 444, 606
- Olah, C. 2015, Neural Networks, Types, and Functional Programming, [Blog post]
- Ontiveros, V. & Vourlidas, A. 2009, *apj*, 693, 267
- Oughton, E. J., Skelton, A., Horne, R. B., Thomson, A. W., & Gaunt, C. T. 2017, *Space Weather*, 15, 65
- Pala, Z. & Atici, R. 2019, *Solar Physics*, 294, 50
- Paouris, E., Vourlidas, A., Papaioannou, A., & Anastasiadis, A. 2021, *Space Weather*, 19, e2020SW002617
- Papaioannou, A., Anastasiadis, A., Kouloumvakos, A., et al. 2018, *Solar Physics*, 293, 1
- Papaioannou, A., Vainio, R., Raukunen, O., et al. 2022, *Journal of Space Weather and Space Climate*, 12, 24
- Park, J., Innes, D. E., Bucik, R., & Moon, Y.-J. 2013, *The Astrophysical Journal*, 779, 184
- Parker, E. N. 1960, *Astrophysical Journal*, 132, 821
- Patsourakos, S. & Vourlidas, A. 2012, *Solar Physics*, 281, 187
- Patsourakos, S., Vourlidas, A., & Stenborg, G. 2010, *Astrophys. J. Lett.*, 724, L188
- Pérez-Suárez, D., Higgins, P. A., Bloomfield, D. S., et al. 2011, Automated Solar Feature Detection for Space Weather Applications, 207–225
- Pesnell, W. D., Thompson, B. J., & Chamberlin, P. C. 2012, *solphys*, 275, 3
- Pick, M. 2006, in *Solar and Heliospheric Origins of Space Weather Phenomena*, ed. J.-P. Rozelot, Vol. 699, 119
- Podladchikova, O. & Berghmans, D. 2005, *Solar Physics*, 228, 265
- Pomoell, J. & Poedts, S. 2018, *Journal of Space Weather and Space Climate*, 8, A35
- Priest, E. & Forbes, T. 2007, Magnetic Reconnection
- Pulkkinen, T. 2007, *Living Reviews in Solar Physics*, 4, 1
- Pulupa, M., Bale, S., Bonnell, J., et al. 2017, *Journal of Geophysical Research: Space Physics*, 122, 2836
- Pulupa, M., Bale, S. D., Badman, S. T., et al. 2020, *Astrophys. J. Suppl.*, 246, 49
- Pysz, M. A., Foygel, K., Panje, C. M., et al. 2011, *Investigative radiology*, 46, 187
- Ramstad, R., Holmström, M., Futaana, Y., et al. 2018, *Geophysical Research Letters*, 45, 7306
- Reames, D. V. 1999, *Space Science Reviews*, 90, 413
- Reames, D. V. 2000in , *American Institute of Physics*, 289–300
- Reames, D. V. 2013, *Space Science Reviews*, 175, 53
- Reames, D. V. 2021
- Reid, H. A. 2020, *Frontiers in Astronomy and Space Sciences*, 7, 56
- Reid, H. A. & Kontar, E. P. 2018a, *Astronomy & Astrophysics*, 614, A69

- Reid, H. A. & Kontar, E. P. 2018b, *The Astrophysical Journal*, 867, 158
- Reid, H. A. & Vilmer, N. 2017, *Astronomy & Astrophysics*, 597, A77
- Reid, H. A. S. & Ratcliffe, H. 2014, *Research in Astronomy and Astrophysics*, 14, 773
- Reiner, M. J., Goetz, K., Fainberg, J., et al. 2009, *Solar Physics*, 259, 255
- Richardson, I., von Rosenvinge, T., & Cane, H. 2016, *Solar Physics*, 291, 2117
- Ripley, B. D. 1996, *Pattern Recognition and Neural Networks* (Cambridge University Press)
- Rodriguez, J., Onsager, T., & Mazur, J. 2010, *Geophysical Research Letters*, 37
- Rouillard, A. P., Plotnikov, I., Pinto, R. F., et al. 2016, *The Astrophysical Journal*, 833, 45
- Rouillard, A. P., Sheeley, N. R., Tylka, A., et al. 2012, *The Astrophysical Journal*, 752, 44
- Saint-Hilaire, P., Vilmer, N., & Kerdraon, A. 2012, *The Astrophysical Journal*, 762, 60
- Saiz, E., Cerrato, Y., Cid, C., et al. 2013, *Journal of Space Weather and Space Climate*, 3, A26
- Samwel, S. & Miteva, R. 2023, *Advances in Space Research*, 72, 3440
- Schatten, K. H., Wilcox, J. M., & Ness, N. F. 1969, *Solar Physics*, 6, 442
- Schrijver, C. J. 2015, *Space Weather*, 13, 524
- Schrijver, C. J., Kauristie, K., Aylward, A. D., et al. 2015, *Advances in Space Research*, 55, 2745
- Schrijver, C. J. & Siscoe, G. L. 2010a, *Heliophysics: Evolving solar activity and the climates of space and Earth* (Cambridge University Press)
- Schrijver, C. J. & Siscoe, G. L. 2010b, *Heliophysics: Evolving solar activity and the climates of space and Earth* (Cambridge University Press)
- Schuster, M. & Paliwal, K. K. 1997, *IEEE transactions on Signal Processing*, 45, 2673
- Schwenn, R. 2006, *Living reviews in solar physics*, 3, 1
- Shibata, K. & Magara, T. 2011, *Living Reviews in Solar Physics*, 8, 1
- Singh, P., Manure, A., Singh, P., & Manure, A. 2020, *Learn TensorFlow 2.0: Implement Machine Learning and Deep Learning Models with Python*, 1
- Sokolov, I. V., Roussev, I. I., Skender, M., Gombosi, T. I., & Usmanov, A. V. 2009, *The Astrophysical Journal*, 696, 261
- Stansby, D., Yeates, A., & Badman, S. T. 2020, *Journal of Open Source Software*, 5, 2732
- Starck, J.-L. & Murtagh, F. 2002, *Astronomical image and data analysis* (Springer Netherlands)
- Sundermeyer, M., Alkhouri, T., Wuebker, J., & Ney, H. 2014, in *Proceedings of the 2014 conference on empirical methods in natural language processing (EMNLP)* (Association for Computational Linguistics), 14–25
- Suzuki, S. & Dulk, G. 1985, Cambridge: Cambridge University Press, 289
- Švestka, Z. 1995, *Advances in Space Research*, 16, 27
- Szenicer, A., Fouhey, D. F., Munoz-Jaramillo, A., et al. 2019, *Science Advances*, 5, eaaw6548
- Temmer, M. 2016, *Astronomische Nachrichten*, 337, 1010
- Temmer, M. 2021, *Living Reviews in Solar Physics*, 18, 4
- Thernisien, A. 2011, *The Astrophysical Journal Supplement Series*, 194, 33
- Thernisien, A., Vourlidas, A., & Howard, R. 2009, *Solar Physics*, 256, 111

- Thompson, B., Plunkett, S., Gurman, J., et al. 1998, *Geophysical Research Letters*, 25, 2465
- Thompson, B. & Young, C. 2016, *The Astrophysical Journal*, 825, 27
- Thompson, B. J. & Myers, D. C. 2009, *Astrophys. J. Suppl.*, 183, 225
- Thompson, W. T. 2006, *A&A*, 449, 791
- Trottet, G., Samwel, S., Klein, K.-L., Dudok de Wit, T., & Miteva, R. 2015, *Solar Physics*, 290, 819
- Truscott, P., Lei, F., Dyer, C., et al. 2000, in 2000 IEEE Radiation Effects Data Workshop. Workshop Record. Held in conjunction with IEEE Nuclear and Space Radiation Effects Conference (Cat. No. 00TH8527), IEEE, 147–152
- Tsurutani, B. T. 1985
- Tsurutani, B. T., Gonzalez, W. D., & Kamide, Y. 1997, *Surveys in geophysics*, 18, 363
- Vainio, R., Desorgher, L., Heynderickx, D., et al. 2009, *Space science reviews*, 147, 187
- Vainio, R. & Laitinen, T. 2008, *Journal of Atmospheric and Solar-Terrestrial Physics*, 70, 467
- van Diepen, G., Dijkema, T. J., & Offringa, A. 2018, *Astrophysics Source Code Library*, ascl
- van Haarlem, M. P., Wise, M. W., Gunst, A., et al. 2013, *Astronomy & astrophysics*, 556, A2
- Verbeeck, C., Delouille, V., Mampaey, B., & De Visscher, R. 2014, *Astronomy and Astrophysics*, 561, A29
- Verbeke, C., Mays, M. L., Kay, C., et al. 2022, *Advances in Space Research*
- Veronig, A., Muhr, N., Kienreich, I., Temmer, M., & Vršnak, B. 2010, *The Astrophysical Journal Letters*, 716, L57
- Vourlidas, A., Syntelis, P., & Tsinganos, K. 2012, *Solar Physics*, 280, 509
- Vourlidas, A., Wu, S. T., Wang, A. H., Subramanian, P., & Howard, R. A. 2003, *apj*, 598, 1392
- Vršnak, B. & Cliver, E. W. 2008, *Solar Physics*, 253, 215
- Vršnak, B., Žic, T., Vrbanec, D., et al. 2013, *Solar physics*, 285, 295
- Warmuth, A. 2015, *Living Reviews in Solar Physics*, 12, 1
- Webb, D. F. & Howard, T. A. 2012, *Living Reviews in Solar Physics*, 9, 1
- Whitman, K., Egeland, R., Richardson, I. G., et al. 2023, *Advances in Space Research*, 72, 5161, cOSPAR Space Weather Roadmap 2022: Scientific Research and Applications
- Wild, J. 1950a, *Australian Journal of Chemistry*, 3, 399
- Wild, J. 1950b, *Australian Journal of Chemistry*, 3, 541
- Wild, J. & McCready, L. 1950, *Australian Journal of Chemistry*, 3, 387
- Wild, J., Smerd, S., & Weiss, A. 1963, *Annual Review of Astronomy and Astrophysics*, 1, 291
- Wills-Davey, M., DeForest, C., & Stenflo, J. O. 2007, *The Astrophysical Journal*, 664, 556
- Wilson, J. W., Townsend, L. W., Chun, S. Y., et al. 1988, BRYNTRN: A baryon transport computer code, computation procedures and data base, Tech. rep.
- Wöllmer, M., Zhang, Z., Weninger, F., Schuller, B., & Rigoll, G. 2013, in 2013 IEEE International Conference on Acoustics, Speech and Signal Processing, IEEE, 6822–6826
- Wood, B., Howard, R., & Socker, D. 2010, *The Astrophysical Journal*, 715, 1524
- Wu, C.-C. & Lepping, R. P. 2016, *Solar Physics*, 291, 265

- Wu, C. S., Wang, C. B., Yoon, P. H., Zheng, H. N., & Wang, S. 2002, *The Astrophysical Journal*, 575, 1094
- Wuelser, J.-P., Lemen, J. R., Tarbell, T. D., et al. 2004, in Society of Photo-Optical Instrumentation Engineers (SPIE) Conference Series, Vol. 5171, Telescopes and Instrumentation for Solar Astrophysics, ed. S. Fineschi & M. A. Gummin, 111–122
- Xapsos, M. A., Stauffer, C. A., Jordan, T. M., Adams, J. H., & Dietrich, W. F. 2012, *IEEE Transactions on Nuclear Science*, 59, 1054
- Xie, H., Ofman, L., & Lawrence, G. 2004, *Journal of Geophysical Research: Space Physics*, 109
- Young, P. R., Tian, H., Peter, H., et al. 2018, *Space Science Reviews*, 214, 1
- Zhang, J., Cheng, X., & Ding, M.-d. 2012, *Nature communications*, 3, 747
- Zhang, J. & Dere, K. P. 2006, *apj*, 649, 1100
- Zhang, J., Richardson, I., Webb, D., et al. 2007, *Journal of Geophysical Research: Space Physics*, 112
- Zhang, P., Wang, C., Ye, L., & Wang, Y. 2019, *Solar Physics*, 294, 62
- Zhang, P., Wang, C. B., & Ye, L. 2018, *Astronomy & Astrophysics*, 618, A165
- Zhang, P., Zucca, P., Kozarev, K., et al. 2022a, *The Astrophysical Journal*, 932, 17
- Zhang, W., Zhao, X., Feng, X., et al. 2022b, *Universe*, 8, 30
- Zhu, H., Zhu, W., & He, M. 2022, *Solar Physics*, 297, 157